KATHOLIEKE UNIVERSITEIT LEUVEN
FACULTEIT TOEGEPASTE WETENSCHAPPEN
DEPARTEMENT BURGERLIJKE BOUWKUNDE
AFDELING HYDRAULICA
Kasteelpark Arenberg 40 – B-3001 Heverlee

OPTICAL REMOTE SENSING FOR THE ESTIMATION OF MARINE BIO-GEOPHYSICAL QUANTITIES

Promotoren:
Prof. Jaak Monbaliu
Prof. Pol Coppin

Proefschrift voorgedragen tot
het behalen van het doctoraat
in de toegepaste wetenschappen

door

Suhyb SALAMA

November 2003

KATHOLIEKE UNIVERSITEIT LEUVEN
FACULTEIT TOEGEPASTE WETENSCHAPPEN
DEPARTEMENT BURGERLIJKE BOUWKUNDE
AFDELING HYDRAULICA
Kasteelpark Arenberg 40 – B-3001 Heverlee

OPTICAL REMOTE SENSING FOR THE ESTIMATION OF MARINE BIO-GEOPHYSICAL QUANTITIES

Jury:
Prof. L. Froyen, (Voorzitter)
Prof. J. Monbaliu, (Promotor)
Prof. P. Coppin, (Co-promotor)
Dr. K. Ruddick, (BMM)
Prof. E. Toorman
Prof. L. Van Gool
Dr. V. Carrère, (Univ. Littoral)
Dr. S. Lavender, (Univ. Plymouth)
Dr. J. Van Orshoven

Proefschrift voorgedragen tot
het behalen van het doctoraat
in de toegepaste wetenschappen

door

Suhyb SALAMA

U.D.C. 556.3

November 2003

D/2003/7515/46

ISBN 90-5682-437-6

rev.2

Acknowledgment

This thesis presents the result of four years of research. I would like to thank all of those who contributed in giving this dissertation its present status.

I would like to express my gratitude to Prof. Jaak Monbaliu for supervising this research and for the fruitful discussions.

I deeply thank Prof. Pol Coppin for helping me to build up the necessary knowledge on earth observation.

I greatly appreciate the assistance and the valuable suggestions of Dr. Kevin Ruddick.

Thanks also to Prof. Erik Toorman and Prof. Luc Van Gool for their remarks. Many thanks to the jury members for reviewing the thesis. Thanks to Prof. Jean Berlamont and the hydraulics laboratory for providing the necessary facilities. Thanks to my colleagues for all those brain-storming-days, meetings and personal visits.

The hydraulics lab and ESA-PRODEX experiment (arrangement No. 90018) are acknowledged for their funds during the last three years of this research.

The support of the following institutions is acknowledged: The teaching support unit (KUL); The geomatics cell for forest engineering (KUL); The Management Unit of Mathematical Models of the North Sea; The Flanders Marine Institute; The Flemish Institute for Technological Research; Dundee University; The German Aerospace Center; The Institute for Environmental Studies-Free University of Amsterdam; The Laboratoire d'Optique Atmosphrique a la Universit des Sciences et Technologies de Lille; The Goddard Archive Center.

I would like to thank Mr. Eugène Vanderstraeten for his help.

I am deeply grateful to my parents, for their continued and unwavering moral support.

I am very thankful to Paul and Riet, my parents-in-law, for their encouragement and concern.

This manuscript would not have been accomplished without the enlightening efforts of Griet, my wife, girlfriend and soul mate.

Thanks to my daughter, Jasmien, for brightening my life.

Preface

The sun generates a wide range of frequencies (or wavelengths) of radiant energy. Only a small part of them, is visible and/or usable by plants and animals. This visible light ranges from blue-violet to deep-red and in between all the other colors of the rainbow.

About 98% of incident sun-light on a calm sea-surface is transmitted to the seawater. This penetrated light is either used for photosyntheses, absorbed by seawater constituents and/or scattered back out of the seawater body. This light, leaving the seawater surface, (i.e. color) is characterized by the absorption and scattering properties of everything in the seawater column, including the seawater itself. This relationship can mathematically be represented by a forward model. The forward model can, in turn, be inverted to retrieve the absorption and scattering properties (or generally inherent optical properties) of the seawater column. The inherent optical properties are related to the types and concentrations of dissolved and suspended constituents in the seawater. In consequence, changes in sea-colors can be assigned to changes in type and concentration of suspended and dissolved materials in the seawater.

The color of the sea can remotely be sensed by earth observation techniques. In this perspective, remote sensing offers a unique opportunity to assess and monitor seawater quality parameters. However, the visible and near infrared part of that characterized energy signal is strongly affected by the atmospheric path to the sensor, meaning that the quality of the retrieved signals is directly related to the effectiveness of the atmospheric correction algorithm.

The contributions, this Ph.D. dissertation intends to make, encompass four major parts. The first deals with the atmospheric correction of the remotely sensed signal from a seawater target. The second uses the corrected signal (i.e water leaving reflectance) to estimate the concentrations of the

suspended and dissolved materials in the seawater. The link between the atmospheric and the oceanic systems is established in the third part. In the last segment the reliability of the water leaving reflectance to estimate concentrations of seawater constituents is evaluated.

Samenvatting

De zon produceert een brede waaier frequenties (of golflengten) aan stralingsenergie. Slechts een klein deel ervan is zichtbaar en/of bruikbaar door planten en dieren. Dit zichtbare licht strekt zich uit van blauw-violet tot donkerrood met daartussen alle andere kleuren van de regenboog.

Ongeveer 98% van het zonlicht dat het zeewateroppervlak bereikt, dringt door tot in het zeewater. Dit doorgedrongen zonlicht wordt deels gebruikt voor fotosynthese, deels geabsorbeerd en/of deels terug uit het zeewater weerkaatst. Het lichtsignaal (d.w.z. kleur), weerkaatst uit het zeewater, wordt gekenmerkt door de absorberende en weerkaatsende eigenschappen van alles wat zich in het zeewater bevindt, met inbegrip van het zeewater zelf. Deze relatie kan mathematisch voorgesteld worden door een model. Dit model kan ook omgekeerd worden toegepast om er de absorberende en weerkaatsende (d.w.z. inherent optische) eigenschappen van het zeewater uit af te leiden. De inherent optische eigenschappen staan in relatie met het type en de hoeveelheid bestanddelen die opgelost en verspreid zijn in het zeewater. Bijgevolg kunnen veranderingen in kleurschakeringen van het zeewater worden toegeschreven aan veranderingen in type en concentratie van verspreide en opgeloste bestanddelen in het zeewater.

De kleur van het zeewater kan door aardobservatietechnieken worden verklaard. In dit perspectief biedt teledetectie een unieke kans om de parameters van de zeewaterkwaliteit te berekenen en te beoordelen. Het zichtbare deel van het kenmerkende energiesignaal wordt op zijn weg richting sensor echter nog sterk beïnvloed door de atmosfeer. Dit betekent dat de kwaliteit van de ontvangen signalen rechtstreeks verband houdt met de doeltreffendheid van het atmosferische correctie-algoritme.

De bijdragen, die deze doctoraatsverhandeling wil leveren, bestaan uit vier thema's. Het eerste behandelt de atmosferische correctie van het telegedetecteerde zeewatersignaal. In een tweede deel worden de verbeterde

signalen gebruikt om de concentraties van verspreide en opgeloste bestanddelen in het zeewater te berekenen. De link tussen atmosferische en oceanische systemen wordt gelegd in het derde deel. Tenslotte wordt de betrouwbaarheid geëvalueerd om met lichtsignalen uit het zeewater de concentraties van zeewaterbestanddelen te berekenen.

Table of Contents

List of Figures

List of Tables

Notations

LATIN

$a(\lambda)$	Bulk absorption coefficient	$[m^{-1}]$
$a^*(\lambda)$	Specific absorption coefficient	$[m^2.g^{-1}]$
$a_{dom}(\lambda)$	Bulk absorption coefficient of DOM	$[m^{-1}]$
$a_{phy}(\lambda)$	Bulk absorption coefficient of phytoplankton pigment (chlorophyll-a)	$[m^{-1}]$
$a_w(\lambda)$	Bulk absorption coefficient of water molecules	$[m^{-1}]$
$b(\lambda)$	Bulk scattering coefficient	$[m^{-1}]$
$b^*(\lambda)$	Specific scattering coefficient	$[m^2.g^{-1}]$
$b_b(\lambda)$	Bulk backward scattering coefficient	$[m^{-1}]$
$b_f(\lambda)$	Bulk forward scattering coefficient	$[m^{-1}]$
$b_{b(spm)}(\lambda)$	Bulk backward scattering coefficient of suspended particulate matter	$[m^{-1}]$
$c(\lambda)$	Bulk beam attenuation coefficient	$[m^{-1}]$

e_i	Residual at band i	
$g(\tan\theta_n)$	Slope-probability-distribution of the wave facets	
$\mathbf{g}$	Gradient vector	
h	Water depth	[m]
$\mathbf{iop}_0$	Solution vector of the sought inherent optical properties	[m^{-1}]
j	Number of iterations	
m	Number of unknowns	
N	Number of bands	
n	Index of refraction	
$\bar{n}$	Angstrom exponenet	
n_a	Air index of refraction	
n_w	Water index of refraction	
q	Photon's energy	[j]
r	Radius in chapter (2)	[m]
r	Correlation coefficient in chapter (3)	[%]
rv_i	The relative contribution of an error component	
s and l	Spectral bands at the NIR part of the spectrum, l being longer than s	[μm]
t	transmittance function	[s]
$t_a(\lambda)$	Aerosol diffuse transmittance	[%]
z	altitude	[m]
A	Area	[m^2]
$C_{i,j}$	An element of a covariance matrix	
C_{spm}	Concentration of SPM	[$g.m^{-3}$]

$D(z,\lambda)$	Distribution function of the average cosine	
$E(\vec{X},\lambda)$	Irradiance	$[Wm^{-2}\mu m^{-1}]$
$E_d(\vec{X},\lambda)$	Down-welling irradiance	$[Wm^{-2}\mu m^{-1}]$
$E_u(\vec{X},\lambda)$	Up-welling irradiance	$[Wm^{-2}\mu m^{-1}]$
$E_o(\vec{X},\lambda)$	Scalar irradiance	$[Wm^{-2}\mu m^{-1}]$
$E_{od}(\vec{X},\lambda)$	Down-welling scalar irradiance	$[Wm^{-2}\mu m^{-1}]$
$E_{ou}(\vec{X},\lambda)$	Up-welling scalar irradiance	$[Wm^{-2}\mu m^{-1}]$
$E_0(\vec{X},\lambda)$	Solar irradiance	$[Wm^{-2}\mu m^{-1}]$
$F(\lambda)$	The ratio of the forward scattering to the scattering coefficient	
$\mathbf{H}$	Hessian matrix	
$\mathbf{H}_0$	Hessian matrix at the solution vector	
$I(\vec{X},\xi,\lambda)$	Intensity	$[W\mu m^{-1}sr^{-1}]$
$\mathbf{J}$	Jacobian matrix	
$K(z,\lambda)$	Diffuse attenuation coefficient	$[m^{-1}]$
$L(\vec{X},\xi,\lambda)$	Radiance	$[Wm^{-2}\mu m^{-1}sr^{-1}]$
$L_d(\vec{X},\xi,\lambda)$	Down-welling radiance	$[Wm^{-2}\mu m^{-1}sr^{-1}]$
$L_u(\vec{X},\xi,\lambda)$	Up-welling radiance	$[Wm^{-2}\mu m^{-1}sr^{-1}]$
$P(\vec{X},\lambda)$	Radiant flux	$[W\mu m^{-1}]$
$P(z)$	Atmospheric pressure at altitude z	[mb]
Q	Energy	[Joule]
$Q(-0,\xi')$	Q ratio	[sr]
Q_a	The efficiency factor of absorption	
Q_b	The efficiency factor of scattering	
Q_c	Attenuation efficiency factor	
$R(z,\lambda)$	Irradiance reflectance at depth z	[%]

$R(-0,\lambda)^{dp}$	Subsurface irradiance reflectance of deep water	[%]
$R_{rs}(\xi,\lambda)$	Remote sensing reflectance	$[sr^{-1}]$
R_{rs}^{dp}	Remote sensing reflectance of deep water	$[sr^{-1}]$
$\mathbf{R}$	The upper triangle matrix of QR matrix decomposition	
S	Surface	
$T(z,\lambda)$	Transmittance	[%]
$T_g^{(\lambda)}$	Gaseous transmittance	[%]
$T_o^{(\lambda)}$	Transmittance from the sun to the target	[%]
$T_v^{(\lambda)}$	Diffuse transmittance from the target to the sensor	[%]
W	Wind speed	[m/s]
UT	Universal Time	
$\overrightarrow{X}$	Cartisian vector	
GREEKS		
$\alpha_{(\lambda_i,\lambda_j)}$	Ratio of the water leaving reflectance at two wavelengths λ_i and λ_j	
$\beta(\psi,\lambda)$	Volume scattering function	$[m^{-1}sr^{-1}]$
$\widetilde{\beta}(\psi,\lambda)$	Scattering- phase function	$[sr^{-1}]$
$\varepsilon^{s}_{(\lambda_i,\lambda_j)}$	Single scattering aerosol ratio	
$\varepsilon_{(\lambda_i,\lambda_j)}$	Multiple scattering aerosol ratio	
λ	Wavelength	$[\mu m]$
$\mu(z,\lambda)$	Average cosine	
ν	Frequency	[s]

Ω	Solid angle	$[sr^{-1}]$
ϕ	Viewing azimuth angle	[rad]
ϕ_0	Solar azimuth angle	[rad]
ϕ, ϕ_0	These symbols are used in appendix C to represent a cost function	
$\tau(z, \lambda)$	Optical thickness	
θ	Viewing zenith angle	[rad]
θ_{pc1}	The angle of the first principal component w.r.t.h.	[degrees]
θ_n	The angle between wave-facet normal and the direction of reflection	[rad]
θ_{reg}	The angle of the regression line w.r.t.h.	[degrees]
θ_0	Solar zenith angle	[rad]
$\omega(\lambda)$	Single scattering albedo	
ψ	Scattering angle	[rad]
ρ	Bottom reflectance	[%]
$\rho_a^{(\lambda)}$	Aerosol reflectance	[%]
$\rho_c^{(\lambda)}$	Corrected reflectance	[%]
$\rho_{df}^{(\lambda)}$	Diffuse surface reflectance	[%]
$\rho_{dr}^{(\lambda)}$	Direct surface reflectance	[%]
$\rho_F(\psi/2)$	Fresnel reflectance	[%]
ρ_M	Measured reflectance	[%]
$\rho_{path}^{(\lambda)}$	Reflectance from the atmospheric path	[%]
$\rho_r^{(\lambda)}$	Air molecules reflectance	[%]
$\rho_{ra}^{(\lambda)}$	Coupled-term reflectance	[%]
ρ_R	Retrieved reflectance	[%]

$\rho_{sfc}^{(\lambda)}$	Sea surface reflectance	[%]
$\rho_t^{(\lambda)}$	Total reflectance	[%]
$\rho_w^{(\lambda)}$	Water leaving reflectance	[%]
$\rho_{w,m}^{(\lambda_i)}$ (**iop**)	The modelled water leaving reflectance	[%]
$\rho_{w0}^{(\lambda)}$	The best fit to the measured spectrum	
$\rho_{w\pm0}^{(\lambda_i)}$	The upper and lower bound of the confidence interval	[%]
$\rho_{w,r}^{(\lambda_i)}$	The measured water leaving reflectance	[%]
$\rho_L^{(\lambda)}$	The lower bound of $\rho_{w0}^{(\lambda)}$	
$\rho_U^{(\lambda)}$	The upper bound of $\rho_{w0}^{(\lambda)}$	
σ	Standard deviation	
$\overrightarrow{\xi}$	Polar vector	
ξ	Pair of the zenith and azimuth angles	
ξ'	Pair of the refracted zenith and azimuth angles	
Ξ	The set of zenith and azimuth angles on the unite sphere	
Ξ_d	The down-ward set of zenith and azimuth angles	
Ξ_u	The up-ward set of zenith and azimuth angles	
χ^2	Chi-square	
ϵ	Error	

ABBREVIATIONS

AOP	Apparent Optical Property
AVHRR	Advance Very High Resolution Radiomter

CASI	Compact Airborne Spectrographic Imagery
Chl-a	Chlorophyll a pigment
CZCS	Coastal Zone Color Scanner
DAIS	Digital Airborne Imaging Spectrometer
DOM	Dissolved Organic Matter
FOV	Field Of View
GF/F	Glass Fiber/ Filter
Hydro-optics	Hydrologic Optics
IFOV	Instantaneous Field Of View
IOP	Inherent Optical Property
MERIS	Moderate-Resolution Imaging Spectrometer
NIR	Near Infra Red
NER	Noise Equivalent Radiance
OD	Optical Density
PCT	Principle Component Transform
PSD	Particle-Size Distribution
Ran	Random number generator
RTE	Radiative Transfer Equation
SeaWiFS	Sea Wide Field of view Sensor
SIOP	Specific Inherent Optical Property
SPM	Suspended Particulate Matter
SNR	Signal to Noise Ratio
TOA	Top Of Atmosphere
WLR	Water Leaving Reflectance

Chapter 1

Introduction

1.1 Marine optical remote sensing

From the top of the atmosphere to and within the water body, solar radiation is affected by the media it travels through absorption, scattering and/or (re-) emission. Radiative transfer theory allows for the phenomenology based description and quantification of this process. The applications of radiative transfer to remote sensing over water can be categorized into hydrological and meteorological optics. In turn hydrological optics can be subdivided into oceanographic and limnologic optics.

This research deals with the remote estimation of sediments suspended in sea water. This is accomplished by studying the interaction of the visible and near infrared (NIR) solar spectrum with the sea water, focusing on the numerical, empirical and experimental aspect of oceanographic optics, rather than on the fine mathematics of the radiative transfer equation. This branch of oceanography represents a combinations of:

- Optical sensors that measure the water-leaving signals over large spatial-scale. This is to provide synoptic views of the oceans over large areas and extended time periods. This task is virtually impossible to achieve via traditional in situ measurements.
- Correction algorithms that improve the quality of the recorded water signal i.e. extracted from the total recorded signal.
- Hydro optical algorithms that retrieve the concentrations of water constituents from the optical signal leaving the water body.

- In-situ measurements to calibrate and validate the correction and the optical models.

In this context marine remote sensing can be seen as a powerful tool for monitoring and prediction of primary production, sediment transport and toxic algae.

1.2 Objective

The objectives of this research are to:

- Quantify suspended particulate matters in the Belgian coastal waters from multi and hyperspectral sensors.
- Improve existing turbid water models.
- Perform all necessary in-situ and laboratory measurements for calibration and validation purposes.

In addition, the research provided the framework to start and operate a new research-unit of marine remote sensing in the Hydraulics laboratory at KULeuven. This included providing the financial and data support to this unit.

1.3 Outlines of the thesis

The conceptual background of this work is summarized in chapter (2), encompassing theoretical formulations in sections (2.1-2.5) and their applications to remote sensing in section (2.6). The theoretical segment explains the concepts of light interaction within the water medium, but is equally applicable to the atmosphere. The optical properties of the water body characterize the water leaving signal as measured by remote sensing technology. The signal recorded at sensor level (air- or space-borne) can be decomposed into a sum of sub-signals. These sub-signals are originated from different scattering processes in the atmosphere, at the sea-surface and in the water column. The remote sensing section (2.6) examines each one of these sub-signals separately, the objective being the extraction of the signal that is leaving the water body (commonly referred to as atmospheric correction). From this signal we wish to go back to the inherent optical properties (IOP) of the water that cause the sensor reading (this is called inverse modelling).

In our work we thus deals with both atmospheric correction of the recorded signal and inverse modelling of the water signal.

The Ph.D. dissertation contains four major scientifically contributing segments. The first (chapters 3 and 4) is concerned with correcting the recorded signal for atmospheric perturbations. The second (chapter 6) deals with the estimation of the inherent optical properties of surface waters. The two are linked in the third segment (chapter 5). Here we propose an approach that simultaneously corrects the recorded signals and retrieves the concentrations of suspended particulate matters. Being a link the third segment was inserted between the first and second segments of this text. The fourth component of this thesis is represented by chapter (7). Here a stochastic technique is proposed that constructs the relative-uncertainty bound around the yet to be retrieved concentrations. This is in order to assess the quality of input data (i.e. water leaving reflectance) and output results (i.e. concentration). We conclude our work in chapter (8) by an extensive summary on atmospheric correction and inverse modelling followed by recommendations for future research. Figure (1.1) illustrates the structure and the scientific contributions of the thesis.

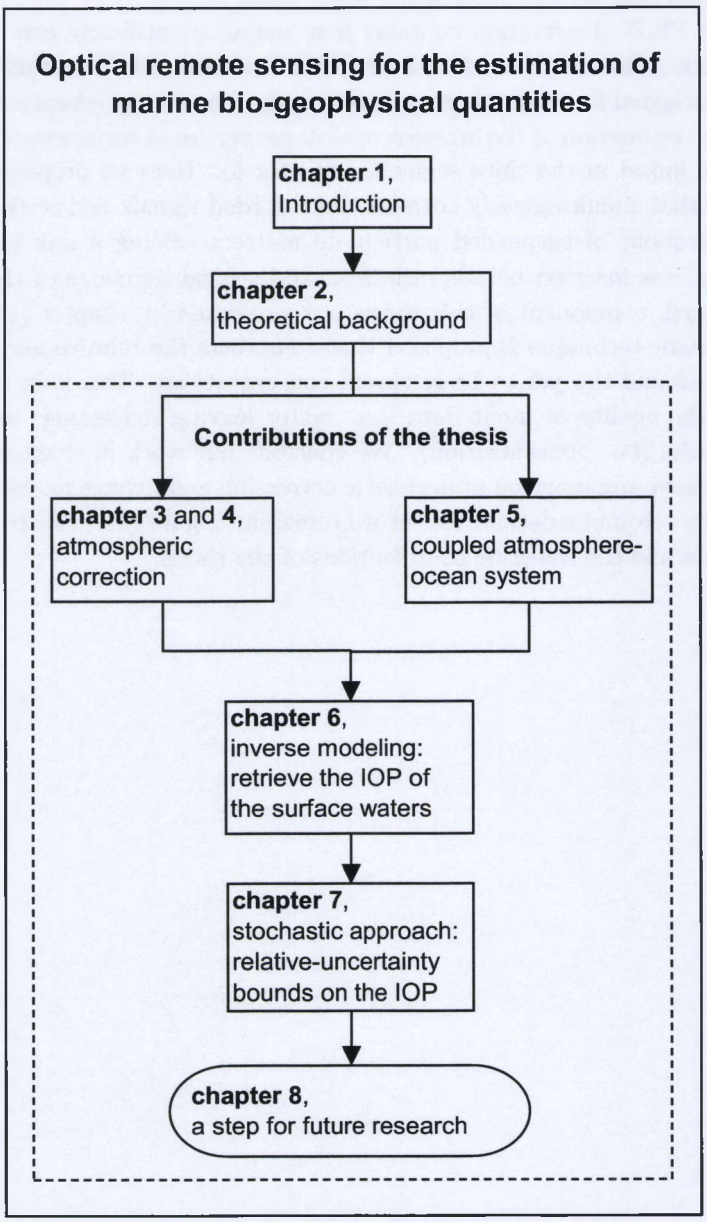

Fig. 1.1: The structure of the thesis with the main contributions.

Chapter 2

The interaction of the solar light with water and atmosphere

Abstract

Through out its path in the water, sunlight is subjected to several attenuation events. This is due to the scattering, absorption and emittance properties of the water molecules and the suspended and dissolved matter within the water column. From this perspective, light leaving the water surface (i.e. transmitted from below the sea surface) can be characterized by the optical properties of everything in the water column, including the water itself. This relationship can mathematically be represented by a forward model in the radiative transfer theory (i.e. radiative transfer equation).

The theoretical background was summarized from Preseindorfer (1976)[1], Mobley (1994)[2], Spinrad *et al.* (1994)[3], Bukata *et al.* (1995)[4] and Thomas and Stemans (1999)[5].

2.1 Introduction

2.1.1 Radiance and irradiance

The spectral radiant flux P is the time rate of radiant energy Q in a specific wavelength interval $\Delta\lambda$ flowing through a given point $\vec{X} = (x, y, z)$ on a surface S. Thus the spectral radiant flux is the time density of radiant energy $[W\mu\mathrm{m}^{-1}]$.

$$P(\vec{X}, \lambda) = \frac{\Delta Q}{\Delta\lambda\Delta t} \tag{2.1}$$

The adjective "spectral" means; per unit wavelength ($\Delta\lambda$ monochromatic). From here on λ dependence is implied and the adjective "spectral" is dropped for brevity. There are two modes to describe the transport of solar radiant energy passing a point $\vec{X} = (x, y, z)$ through a direction $\xi(\theta, \phi)$ (i.e. zenith and azimuth angle) on a plane (sea surface) in three-dimensional space (the coordinate system of this three-dimensional space is defined in appendix B):

- Parallel flow of the photons: which can be described as the amount of radiant flux $P(\vec{X}, \lambda)$ passing a small surface S on a plane normal to the direction of propagation. Thus the area density of radiant flux is the *irradiance*: $E(\vec{X}, \lambda) = P(S)/A(S)$ $[Wm^{-2}\mu m^{-1}]$. Where A is the area of S:

  $$E(\vec{X}, \lambda) = \frac{\Delta Q}{\Delta\lambda\Delta t\Delta A} \tag{2.2}$$

  If the photons are travelling at an angle θ relative to the surface-normal, then the actual area is modified as $A\cos\theta$. Thus the irradiance is proportional to the cosine of the angle between the direction of incident light and the surface normal. This statement is called the cosine law of irradiance.

- A complementary mode of flow is in terms of the passage of photons through a solid angle bounding a set of directions D around $\xi(\theta, \phi)$. The solid angle density of the radiant flux is the *intensity* $I(\vec{X}, \xi, \lambda) = P(D)/\Omega(D)$ $[W\mu m^{-1}sr^{-1}]$. Where Ω is the solid angle content of the bundle D of directions normal to S at $\vec{X}$.

These two modes can also be combined in a direct union. This is the *radiance* which is the density of radiant flux across a surface S and a set of directions D. This is equivalent to the irradiance viewed from a small solid angle around a given direction $\xi(\theta, \phi)$ through the point $\vec{X}$ on the surface S. This can be written as $L(\vec{X}, \xi, \lambda) = P(S, D)/A(S)\Omega(D)$; it has unit of

power per area per wavelength per steradian $[Wm^{-2}\mu m^{-1}sr^{-1}]$:

$$L(\vec{X},\xi,\lambda) = \frac{\Delta Q}{\Delta\lambda\Delta t\Delta A\Delta\Omega} \tag{2.3}$$

The radiance is the fundamental radiometric quantity of interest in ocean color. It specifies the spatial, temporal, directional and wavelength structure of the light field. Actually all other radiometric quantities can be derived from the radiance $L(\vec{X},\xi,\lambda)$. The radiance at point $\vec{X}$ and direction ξ can be linked to the associated irradiance as:

$$E(\vec{X},\lambda) = \int_{\xi\in\Xi} L(\vec{X},\xi,\lambda)\cos\theta d\Omega \tag{2.4}$$

Where Ξ is the set of zenith and azimuth angels on a unit sphere. The set Ξ has two subsets (Ξ_u and Ξ_d) each of which defines an upper and a lower half-sphere of zenith and azimuth angels (see appendix B). The downward irradiance can be calculated from L by integrating the quantity $L(\vec{X},\xi,\lambda)\cos\theta$ over all downward directions:

$$E_d(\vec{X},\lambda) = \int_{\xi\in\Xi_d} L(\vec{X},\xi,\lambda)\cos\theta d\Omega \tag{2.5}$$

From the definition of incremental solid angle (see appendix B equation B-5) we can write the above equation as:

$$E_d(\vec{X},\lambda) = \int_{\phi=0}^{2\pi}\int_{\theta=0}^{\pi/2} L(\vec{X},\xi,\lambda)\sin\theta\cos\theta d\theta d\phi \tag{2.6}$$

In an equivalent manner, the upward irradiance can be expressed as:

$$E_u(\vec{X},\lambda) = \int_{\phi=0}^{2\pi}\int_{\theta=\pi/2}^{\pi} L(\vec{X},\xi,\lambda)\sin\theta\cos\theta d\theta d\phi \tag{2.7}$$

The total irradiance that is incident on a point (e.g. particle of suspended sediment) in all directions is the *scalar irradiance*. It can be calculated from (2.4) by dropping the cosine term ($\cos\theta$):

$$E_o(\vec{X},\lambda) = \int_{\phi=0}^{2\pi}\int_{\theta=0}^{\pi} L(\vec{X},\lambda)\sin\theta d\theta d\phi \tag{2.8}$$

The total scalar irradiance can be partitioned into two terms corresponding to the subsets Ξ_u and Ξ_d (integrating by parts):

$$\begin{aligned} E_o(\overrightarrow{X},\lambda) &= \int_{\Xi} L(\overrightarrow{X},\xi,\lambda)d\Omega \\ &= \int_{\Xi_d} L(\overrightarrow{X},\xi,\lambda)d\Omega + \int_{\Xi_u} L(\overrightarrow{X},\xi,\lambda)d\Omega \\ &= E_{od}(\overrightarrow{X},\lambda) + E_{ou}(\overrightarrow{X},\lambda) \end{aligned} \quad (2.9)$$

The projection of the scalar irradiance (2.8) on the direction $\overrightarrow{\xi}$ is the *vector irradiance*:

$$\overrightarrow{E}(\overrightarrow{X},\lambda) = \int_{\phi=0}^{2\pi}\int_{\theta=0}^{\pi} L(\overrightarrow{X},\xi,\lambda)\overrightarrow{\xi}\sin\theta d\theta d\phi \quad (2.10)$$

Note that the vector irradiance has three components corresponding with the direction vector $\overrightarrow{\xi}$. The magnitude of the vector irradiance is the maximum net irradiance attainable when sampling all possible directions ξ of flow at point $\overrightarrow{X}$.

2.1.2 Properties of radiance and irradiance

If $L(\overrightarrow{X},\xi,\lambda)$ is uniform (i.e. independent of ξ at $\overrightarrow{X}$) and of magnitude L then from (2.4):

$$\begin{aligned} E(\overrightarrow{X},\lambda) &= L\int_{\phi=0}^{2\pi}\int_{\theta=0}^{\pi}\sin\theta\cos\theta d\theta d\phi \\ E(\overrightarrow{X},\lambda) &= 2\pi L \end{aligned} \quad (2.11)$$

The downward irradiance is then (2.6):

$$\begin{aligned} E_d(\overrightarrow{X},\lambda) &= L\int_{\phi=0}^{2\pi}\int_{\theta=0}^{\pi/2}\sin\theta\cos\theta d\theta d\phi \\ E_d(\overrightarrow{X},\lambda) &= \pi L \end{aligned} \quad (2.12)$$

The scalar irradiance is (2.8) :

$$\begin{aligned} E_o(\overrightarrow{X},\lambda) &= L\int_{\phi=0}^{2\pi}\int_{\theta=0}^{\pi}\sin\theta d\theta d\phi \\ E_o(\overrightarrow{X},\lambda) &= 4\pi L \end{aligned} \quad (2.13)$$

The irradiance at the surface of an imaginary sphere (emitted from its center), by conservation of energy, is independent of the sphere radius r. However since the area of the spherical surface increases as r^2 the irradiance must decrease as r^{-2}. Thus :

$$\frac{E(\overrightarrow{X_1}\lambda)}{E(\overrightarrow{X_2},\lambda)} = \frac{r^2_{(2)}}{r^2_{(1)}} \tag{2.14}$$

The n^2 law of radiance (where n is the medium's index of refraction) states that the ratio L/n^2 is invariant along its path ξ (in the air)$-\xi'$(in the water) with respect to the transmittance function t of the air-water interface. In other words:

$$\frac{L(\overrightarrow{X},\xi,\lambda)}{{n_a}^2} = t\frac{L(\overrightarrow{X},\xi',\lambda)}{{n_w}^2} \tag{2.15}$$

Where n_a and n_w are the index of refraction of air and water respectively. The transmittance function t is defined as being the ratio of the transmitted spectral radiant power to the incident spectral radiant power on a surface.

2.2 Apparent optical properties

The above discussed radiometric quantities are apparent optical properties (AOP). In other words they vary with respect to the viewing-illumination geometry for a giving water body. The AOP are function of the whole set-up of the viewing-illumination geometry, boundary-conditions and the inherent optical properties of the medium. Other apparent optical properties can be derived from the radiance and irradiance as follows. The reduction in the solar irradiance $E_0(\overrightarrow{X},\lambda)$ that travels a distance dl through uniformly mixed medium will be proportional to the attenuation coefficient of that medium $K(\overrightarrow{X},\lambda)$:

$$\frac{dE(\overrightarrow{X},\lambda)}{dl} = -K(\overrightarrow{X},\lambda)E(\overrightarrow{X},\lambda) \tag{2.16}$$

Considering the vertical attenuation ($z = lcos(\theta)$) and integrating the above equation (2.16) over the depth z:

$$E(z,\lambda) = E_0(z,\lambda)\exp\left[-\frac{1}{cos(\theta)}\int_{z_0}^{z} K(z,\lambda)dz\right] \tag{2.17}$$

This is Beer's law, which states that the light is exponentially attenuated through a homogeneous media travelling a distance l. The transmittance T

and optical thickness τ of this medium are:

$$T(z,\lambda) = \exp\left[-\frac{1}{cos(\theta)}\int_{z_0}^{z} K(z,\lambda)dz\right] \tag{2.18}$$
$$\tau(z,\lambda) = \int_{z_0}^{z} K(z,\lambda)dz$$

The coefficient $K(z,\lambda)$ is called the diffuse attenuation coefficient. This AOP is a measure of the attenuation rate of radiometric quantities (radiance, irradiance or scalar irradiance) per unit vertical distance. The down-/up- welling average cosine (μ_d, μ_u), by definition, is the ratio of the down (up) welling irradiance to the down-/up- welling scalar irradiance:

$$\mu_d(z,\lambda) = \frac{1}{D_d(z,\lambda)} = \frac{E_d(z,\lambda)}{E_{od}(z,\lambda)} \tag{2.19}$$
$$\mu_u(z,\lambda) = \frac{1}{D_u(z,\lambda)} = \frac{E_u(z,\lambda)}{E_{ou}(z,\lambda)}$$

Where $D_d(z,\lambda)$ and $D_u(z,\lambda)$ are the down-welling and the up-welling distribution function respectively. The unit-less irradiance reflectance is the ratio of the upward irradiance to the downward irradiance:

$$R(z,\lambda) = \frac{E_u(z,\lambda)}{E_d(z,\lambda)} \tag{2.20}$$

The remote sensing reflectance is defined as being the ratio of the water leaving radiance L_u to the down-welling irradiance just above the sea surface.

$$R_{rs}(\xi,\lambda) = \frac{L_u(+0,\xi,\lambda)}{E_d(+0,\lambda)} \tag{2.21}$$

Let us note that the R_{rs} has a unit of $[sr^{-1}]$. The remote sensing reflectance just above the sea surface can be related to the irradiance reflectance just below the surface such by (Mobley 1994[2], Lee *et al.*, 1998[6]):

$$R_{rs}(\xi,\lambda) \approx \frac{1}{Q}\frac{XR(-0,\lambda)}{1-YR(-0,\lambda)} \tag{2.22}$$

Where X and Y describe the fraction of the transmitted and internally-reflected light, respectively. The parameter Q is the ratio of the water up-welling irradiance to up welling radiance just beneath the surface (-0) in

the direction ξ':

$$Q(-0,\xi') = \frac{E_u(-0,\lambda)}{L_u(-0,\xi',\lambda)} \tag{2.23}$$

Note that the direction ξ' (of a light-beam under water) is refracted and transmitted at the sea surface to ξ. The values of Q varies from 3 to 6 with low value occurring in clear waters at blue wavelength (Morel and Gentili 1993[7] and 1996[8]). Let us note that for $Y = 0$ the right hand side of equation (2.22) is the subsurface remote sensing reflectance (similar to 2.21). The parameter X represents the surface transmittance. Its value can be assumed constant (X=0.54 Gordon *et al.*, 1988[9] or 0.5 from Lee *et al.*, 1999[10]). Note that equation (2.22) is for sun at zenith angle, nadir viewing angle, flat surface and constant water-index of refraction. The denominator in equation (2.22) accounts for the effects of internal reflection from water to air with Y=1.5 (Gordon *et al.*, 1988)[9].

Apparent optical properties can be measured, but they are very difficult to interpret. This is due to their dependency on illumination, sea state, depth and viewing geometry. Moreover the AOP's are not additive nor linear with respect to the concentration of water-constituents.

2.3 Inherent optical properties

2.3.1 Introduction

Inherent optical properties (IOP) characterize the optical behavior of the medium. These properties are independent of illumination-viewing geometry and sea state. For a given illumination-viewing geometry the IOP entirely determines the water leaving radiance (i.e. apparent optical properties of the water). These properties are: absorption coefficient $a(\lambda)$, scattering coefficient $b(\lambda)$ and the volume scattering function $\beta(\psi,\lambda)$. The absorption/scattering coefficient is a measure of the fraction of incident radiation power that is absorbed/scattered per unit path-length of the water medium. These coefficients ($a(\lambda)$ and $b(\lambda)$) have units of $[m^{-1}]$. The sum of the absorption and scattering coefficients is the beam attenuation coefficient:

$$c(\lambda) = a(\lambda) + b(\lambda) \tag{2.24}$$

The medium is characterized as being scatterer or absorber by the single scattering albedo:

$$\omega(\lambda) = \frac{b(\lambda)}{c(\lambda)} = 1 - \frac{a(\lambda)}{c(\lambda)} \tag{2.25}$$

The function that describes the angular distribution of the single-event scattering around the incident direction is the volume scattering function $\beta(\psi, \lambda)$ $[m^{-1}sr^{-1}]$. Integrating $\beta(\psi, \lambda)$ over all directions (solid angles) will give the the scattering coefficient $b(\lambda)$.

$$b(\lambda) = \int_{\Xi} \beta(\psi, \lambda) d\Omega \tag{2.26}$$

Where ψ is the scattering angle between the incident beam with direction ξ and the scattered beam with direction ξ'. The scattering in natural water can be assumed independent of the azimuthal direction (Mobley 1994)[2]. The above equation can then be simplified to:

$$b(\lambda) = 2\pi \int_0^{\pi} \beta(\psi, \lambda) \sin\psi d\psi \tag{2.27}$$

The scattering coefficient is decomposed to the sum of forward scattering b_f by integrating (2.27) over $0 \leq \psi \leq \pi/2$ and backward scattering b_b by integrating (2.27) over $\pi/2 \leq \psi \leq \pi$. The volume scattering phase function is defined as being the ratio:

$$\tilde{\beta}(\psi, \lambda) = \frac{\beta(\psi, \lambda)}{b(\lambda)} \tag{2.28}$$

In this way the volume scattering function is decomposed into two components. The first represents the strength of the scattering $b(\lambda)$. The second describes the angular distribution of the scattered photon $\tilde{\beta}(\psi, \lambda)$.

Sea water is a complex (physical, chemical and biological) medium composed of dissolved and suspended living and non-living materials. These quantities can be regarded as being scattering, absorbing and scattering-absorbing centers. Sea-water constituents are water molecules, living materials (plankton), dissolved salts and gases, dissolved organic matter, suspended matter and air/gas bubbles. Each one of these components has its own optical property that contributes, in proportion to its concentration, to the up-welling reflectance leaving the water body. The IOP (absorption and scattering coefficients) of a constituent i can be linearly related to its

concentrations C_i through the specific inherent optical properties (SIOP):

$$\begin{aligned} a_i(\lambda) &= a_i^*(\lambda) \times C_i \\ b_i(\lambda) &= b_i^*(\lambda) \times C_i \end{aligned} \tag{2.29}$$

Where $(a_i(\lambda),\ b_i(\lambda))$ and $(a_i^*(\lambda),\ b_i^*(\lambda))$ are the IOP and the SIOP of the constituent i respectively. The notation a is used to represent the absorption coefficient while b is used to represent the scattering coefficient. Note that the specific inherent optical properties have unit of $[m^2 g^{-1}]$. The SIOP can therefore be viewed as being the projected area per unit weight of the constituent i. The bulk IOP of the water column can be regarded as the sum of the N IOPs of the N constituents presented in the water plus the IOP of water molecules:

$$\begin{aligned} a(\lambda) &= a_w(\lambda) + \sum_{i=2}^{N} a_i(\lambda) \\ b(\lambda) &= b_w(\lambda) + \sum_{i=2}^{N} b_i(\lambda) \\ \beta(\psi, \lambda) &= \beta_w(\psi, \lambda) + \sum_{i=2}^{N} \beta_i(\psi, \lambda) \end{aligned} \tag{2.30}$$

2.3.2 Purified sea-water

Purified sea-water is defined, here, as sea-water free from optical effects caused by components other than the water molecules and dissolved salt. The adjective purified will be dropped for brevity. Inorganic salts dissolved in sea waters affect the absorption and scattering occurring within the water column. The most significant absorption is observable at ultraviolet rather than visible wavelengths. The presence of dissolved inorganic salts increases the scattering by about 30-40% which will be accounted for in equation (2.32).

Scattering

The scattering of sea-water can be assumed symmetric (Morel 1974). In other words the backward scattering is numerically equal to scattering in the forward direction. The scattering coefficient of pure sea-water can be

calculated as (Mobley 1994[2], equation 3.44 page 124):

$$b_w(\lambda) = 5.826 \times 10^{-3} \left(\frac{400}{\lambda}\right)^{4.322} \tag{2.31}$$

This equation is compared to the in-situ measurements (performed by IVM 2000[11]) in the North Sea (figure 2.1(a)). There is a relative-difference of about 40.8% between the measured and calculated values (from equation 2.31) of sea-water scattering coefficient. This difference-value (40.8%) is comparable to the difference-value (30%) between the scattering coefficient of pure-water and pure sea-waters with salinity 35-39% (Mobley 1994)[2]. This encourages us to compare the results of equation (2.31) with tabulated values of scattering coefficients (Morel 1974[12], Mobley 1994[2]). It was found that the scattering coefficient calculated from (equation 2.31) is for pure-water and not for sea-water. Thus equation (2.31) has to be modified for saline waters of the North Sea (multiplied by the factor 1.408):

$$b_w(\lambda) = 8.2030 \times 10^{-3} \left(\frac{400}{\lambda}\right)^{4.322} \tag{2.32}$$

Absorption

The absorption coefficient of sea-water molecules has been reported by many authors (Pop and Fry 1997[13], Smith and Baker 1981[14], Hale and Querry

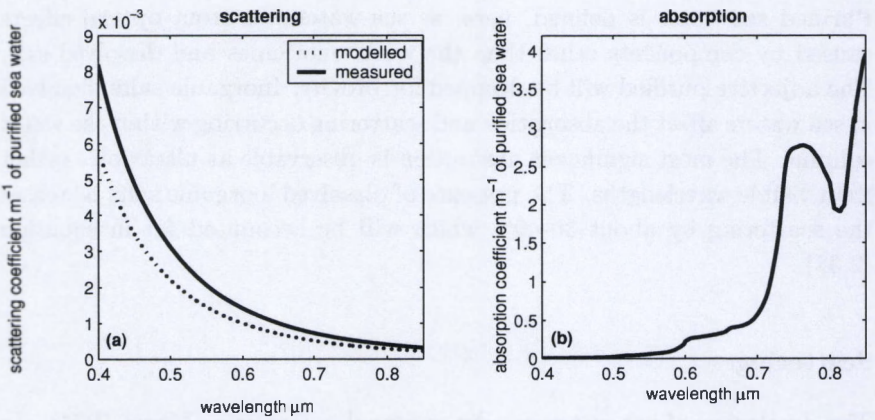

Fig. 2.1: Optical properties of purified sea water; (a): measured and modelled (equation 2.31) scattering coefficient. (b) absorption coefficient.

1973[15], and Palmer and Williams 1974[16]). Figure (2.1(b)) illustrates the absorption coefficient of sea waters. At the NIR range of the spectrum the sea-water absorbs most of the light that penetrates its surface. This fact was used in developing most atmospheric correction algorithms. Note that dissolved gases have no significant effect on the total absorption of sea-waters (Bukata *et al.*, 1995)[4].

2.3.3 Dissolved organic matter (DOM)

Dissolved organic matter (DOM) is the results of decaying living organism.

Scattering

Dissolved organic matters have no significant influence on the total scattering occurring in the water column.

Absorption

The DOM are good absorber of the blue light (figure 2.2). The absorption spectra of DOM can be measured or evaluated as (Bricuad *et al.*, 1981)[17]:

$$a_{dom}(\lambda) = a_{dom}(\lambda_0) \exp\left[-0.014(\lambda - \lambda_0)\right] \tag{2.33}$$

Where λ_0 is a reference wavelength. The common reference wavelength is λ_0=0.44 μm (Mobley 1994)[2]. The performance of equation (2.33) is

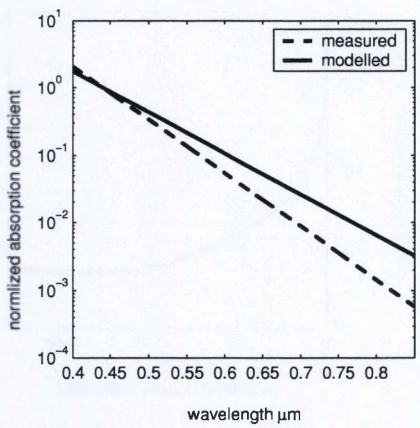

Fig. 2.2: The modelled and measured normalized-absorption of DOM.

compared to the measurements of IVM in figure (2.2). There is a clear discrepancy between the measured and modelled values of DOM absorption. This might be attributed to the spectral variations of DOM in the North Sea which is different than that of equation (2.33) (i.e. the constant 0.014). However the most important observation is that the absorption coefficient of DOM decreases dramatically with increasing wavelength.

The concentration of DOM is usually given in unit of grams of carbon per unit volume, which is about four times lower than the concentration of dissolved salts (Bukata *et al.*, 1995)[4]. However the impact of DOM absorption is greater than that of dissolved salts. Although the abundance of DOM considerably increases the absorption of light in the water, it does not significantly impact the bulk scattering of the water.

2.3.4 Suspended particulate matter (SPM)

The Southern Bight of the North Sea exhibits a permanent high load of suspended matter (Eisma and Kalf 1979)[18]. This arises from transport and re-suspension of sediment materials through hydrodynamic processes, from river discharge and from the nearly continuous dredging activities in the area. Suspended particulate matter (SPM) consists of organic and inorganic material. The light absorption of SPM can be decomposed as being the sum of pigmented SPM absorption and de-pigmented SPM absorption. This separation is of vital importance for biological studies. On the other hand,

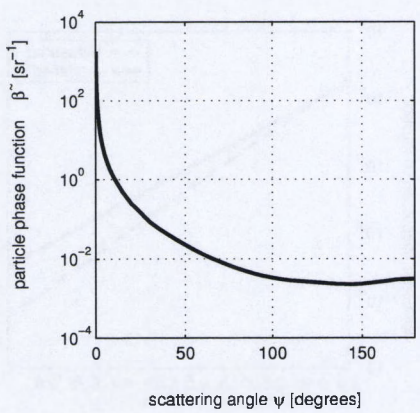

Fig. 2.3: The particle phase-function ($\lambda = 0.514$ μm) averaged from Petzold's scattering phase-functions.

similar separation of the scattering coefficient of SPM is not considered in the course of this thesis.

Scattering

Suspended particulate matter is the main scatterer of light in the water. The presence of SPM dramatically changes the volume scattering function and hence the scattering coefficient. Mobley (1994)[2] defined a typical (average) particle phase function. This phase function was averaged from those measured by Petzold (1972)[19]. Figure (2.3) shows that this phase function is strongly peaked in the forward directions. This feature (forward-peaked scattering) allows us to use the quasi-single scattering approximation of Gordon (1994)[20]. The measured specific scattering coefficient is illustrated in figure (2.4(a)). Figure (2.4(b)) shows the predictions of the specific scattering coefficient of small and large particles using the two-component model of Kopelevich (1983)[21] and its extension by Hatrin and Kattawar (1991)[22]. This model has the form:

$$b_b^*(\lambda) = b_b^*(0.4)\left(\frac{0.4}{\lambda}\right)^y \tag{2.34}$$

Where y is the spectral-shape parameter which can take the values (0.3 and

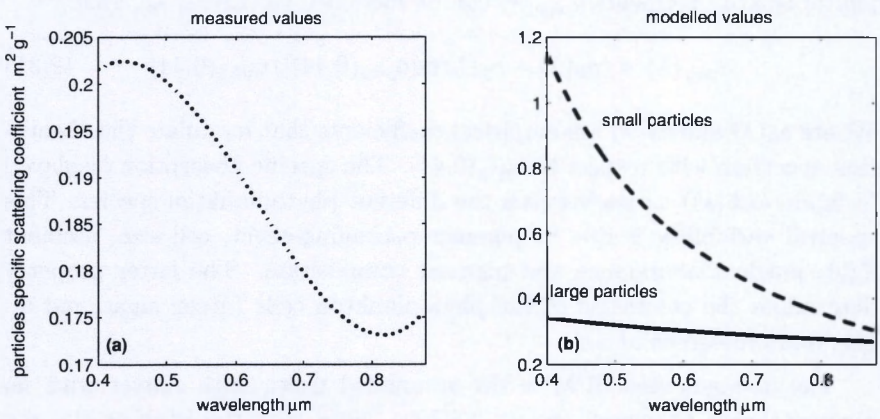

Fig. 2.4: (a): Measured specific-scattering coefficient of suspended particles; (b): The predictions from Kopelevich's model.

This can be attributed to equation (2.34) which neglects the variations in the refraction-index and size distribution of SPM. Or to the procedure used by IVM[11] to calculate the scattering coefficient (Robert Vos 2001 personal communication). Their procedure was by fitting the measured water leaving reflectance to the modelled spectrum using the model of Gordon *et al.* (1988)[9]. Then a backscattering fraction value (the ratio $b_b(\lambda)/b(\lambda)$) of 0.019 was used to estimate the scattering coefficient of SPM. This value can be anything else than the 0.019. The backscattering fraction of suspended particles vary from 0.02 to 0.5 depending on particles load (number per volume), composition and size distribution in the water column (see Mobley 1994[2], table 3.11).

Absorption

Phytoplankton is the main source of SPM light absorption. The most important pigment is chlorophyll and especially chlorophyll-a (Chl-a) since all green algae contain chlorophyll-a. Chlorophyll-a can be considered as being the major pigment affecting the absorption property of the water medium. The specific absorption coefficient was measured during IVM in-situ campaigns. Generally chlorophyll-a has two strong absorption bands in the blue (0.443 μm) and in the red (0.675 μm) respectively. Let us note that the blue peak is higher than the red. This is due to the accessory pigments which absorb the light at the short wavelengths. The total absorption of phytoplankton pigments $a_{phy}(\lambda)$ can be modelled as (Lee *et al.*, 1998)[6]:

$$a_{phy}(\lambda) = (a_0(\lambda) + a_1(\lambda) \ln[a_{phy}(0.44)])\, a_{phy}(0.44) \qquad (2.35)$$

Where $a_0(\lambda)$ and $a_1(\lambda)$ are empirical coefficients that modulate the absorption spectrum with respect to $a_{phy}(0.44)$. The specific absorption displayed in figure (2.5(a)) varies between the different phytoplankton species. This spectral variability is due to pigment packaging-effect, cell size, ambient light, nutrient abundance and pigment composition. The latter property determines the coloration of the phytoplankton cells (green algae, red algae, and blue-green algae).

The de-pigmented SPM is the suspended particulate matter with no pigment being presented (figure 2.5(b)). Note that the peak at the red band is artificial. This is probably due to the imperfect bleaching of the sample (Fargion and Muller, 2000)[23].

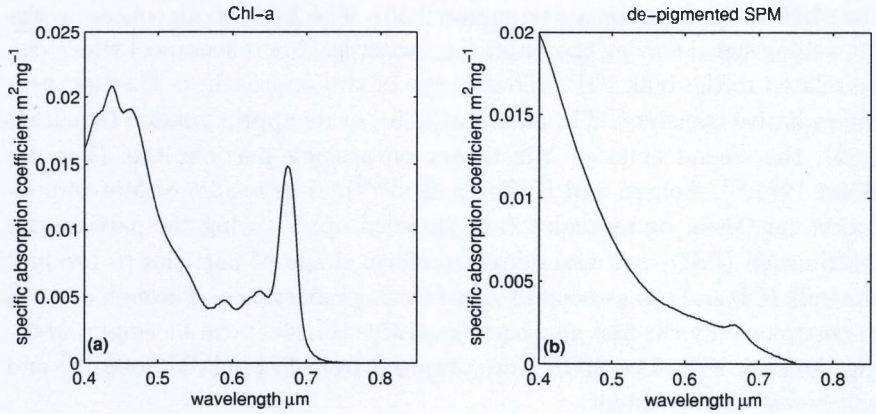

Fig. 2.5: The specific-absorption coefficient of: (a) chlorophyll-a; (b) de-pigmented suspended particulate matter.

2.3.5 Air bubbles

Two processes might be considered as the main sources of air bubbles in the sea surface-layer. The first is breaking waves at the sea surface and the second is due to biological processes. In consequence two types of bubbles can be recognized, the first being clean air bubbles and the second being gas bubbles coated with organic film. Regardless of their origin and type; air bubbles are strong scattering centers (Terrill *et al.*, 2001)[24]. The presence of a large number of bubbles in the near-surface will modify (increase) the observable water leaving reflectance. This might be, erroneously, attributed to the presence of suspended particulate matter. The effect of air bubbles on the backscattering coefficient will not be considered in this study. For more details we refer the reader to the work of Yan *et al.* (2002)[25] and Zhang *et al.* (2002)[26].

2.4 Relationships between the AOP and the IOP of the water

2.4.1 Analytical methods

For given illumination conditions the apparent optical properties (AOP) are entirely determined by the bulk inherent optical properties (IOP) of the water. In turns, these bulk IOP can be estimated from the concentration and

the SIOP of the constituents (equation 2.30). The AOP of our concern is the up-welling signal leaving the water (i.e. water leaving reflectance) which can be related to the bulk IOP following one of two approaches. The first uses the radiative transfer (RTE, equation 2.36), or its approximation (equation 2.39), the second employs Mie theory on a single-particle level (Van De Hulst 1981[27], Bohren and Huffman 1983[28]). The results of Mie computation can, then, be up-scaled (i.e. summed up) knowing the particle-size distribution (PSD) and assuming a uniform shape of particles to produce the bulk IOP and the associated water leaving reflectance. Through out this dissertation only the first approach (radiative transfer) will be employed using the bulk IOP. The SIOP were obtained from IVM (IVM 2000)[11] and will be assumed constant.

The radiance leaving the water body can be related to the bulk inherent optical properties of the water column through the radiative transfer equation. This equation describes the gain and losses of the light-energy during its transfer through a medium. Supposing a plane parallel water body (i.e. IOP are only depth dependent for a location) with neither inelastic scattering (e.g. fluorescence) nor internal source (e.g. bioluminescence), then the RTE is:

$$\cos\theta \frac{dL(z,\xi,\lambda)}{dz} = -c(z,\lambda)L(z,\xi,\lambda) + \int_{\Xi} \beta(z,\psi,\lambda)L(z,\xi',\lambda)d\Omega' \quad (2.36)$$

The first term on the right hand side represents the attenuation of the incident radiance, in the direction $\xi(\theta,\phi)$, by scattering and absorption. The gain of radiance due to scattering into the radiance path from other directions $\xi'(\theta,\phi)$ is represented in the second term. Good text books for the derived solution of RTE are (Preisendorfer 1976[1], Mobley 1994[2], Gordon 1994[20] and Thomas and Stamnes 1999[5]).

2.4.2 Semianalytical methods: Hydro-optical models

Surface water model

Gordon *et al.* (1988)[9] developed a semianalytical model that links the sub-surface irradiance reflectance (equation 2.20) to the IOP of the water:

$$\frac{R(-0,\lambda)}{Q} = \sum_{i=1}^{i=2} l_i \left(\frac{b_b(\lambda)}{b_b(\lambda)+a(\lambda)} \right)^i \quad (2.37)$$

Where $l_1 = 0.0949$ and $l_2 = 0.0794$ are the subsurface expansion coefficients due to internal refraction, reflection and sun zenith. Substituting equation (2.37) in equation (2.22) and assuming Y=0 and X=0.54 (see section 2.3) we will have:

$$R_{rs}(\xi, \lambda) = 0.54 \sum_{i=1}^{i=2} l_i \left(\frac{b_b(\lambda)}{b_b(\lambda) + a(\lambda)} \right)^i \tag{2.38}$$

The second power of the right hand side of equation (2.38) can be ignored (i.e. $i = 1$)(Kirk 1994)[29]. For uniform radiance field (equation 2.12) the water leaving reflectance can be linked to the IOP as:

$$\frac{\rho_w^{(\lambda)}}{T_0^{(\lambda)}} = 0.54 \pi l_1 \frac{b_b(\lambda)}{b_b(\lambda) + a(\lambda)} \tag{2.39}$$

where $\rho_w^{(\lambda)}$ is the water leaving reflectance normalized to the solar transmittance from sun-to-target ($T_0^{(\lambda)}$). Note that the water leaving reflectance is unit-less, in contrary to the remote sensing reflectance which has a unit of $[sr^{-1}]$. The above equation is for the surface layer of sea-waters, a nadir viewing angle and negligible internal reflection of the sea surface.

Shallow water model

Lee *et al.* (1996[30], 1998[6] and 1999[10]) derived a model for shallow waters. They assumed that the subsurface remote sensing reflectance (equation 2.37) can be approximated as being the sum of a deep water signal $R_{rs}(-0, \lambda)^{dp}$ and a bottom signal ρ. Both signals are exponentially attenuated along their path to the surface (Gordon *et al.*, 1975[31], Gordon 1976[32]):

$$\begin{aligned} R_{rs}(-0, \lambda) = {} & R_{rs}(-0, \lambda)^{dp} \\ & \times \left(1 - \alpha_0 \exp\left\{ - \left[D_u + \frac{1}{\cos\theta_v} d_0 (1 + d_1 u)^{0.5} \right] \kappa h \right\} \right) \\ & + \alpha_1 \rho \exp\left\{ - \left[D_u + \frac{1}{\cos\theta_v} d_2 (1 + d_3 u)^{0.5} \right] \kappa h \right\} \end{aligned} \tag{2.40}$$

The term $1/\cos\theta_v$ accounts for the effect of the viewing angle θ_v on the pathlength of the light through the water column with depth h. The subsurface

remote sensing reflectance of deep water was estimated as:

$$R_{rs}(-0,\lambda)^{dp} = (g_0 + g_1 u)u \tag{2.41}$$

With:

$$\begin{aligned} \kappa &= b_b(\lambda) + a(\lambda) \\ u &= \frac{b_b(\lambda)}{\kappa} \end{aligned}$$

Let us note that equation (2.41) is similar to equation (2.37) with adjusted values of the coefficients l_i. The coefficients $g_0, g_1, \alpha_0, \alpha_1, d_0, d_1, d_2$ and d_3 are empirical-parameters and might take the values (Lee *et al.*, 1999)[10]:

$$\begin{aligned} g_0 &\approx 0.084, & g_1 &\approx 017 \\ \alpha_0 &= 1, & \alpha_1 &= 1/\pi \\ d_0 &\approx 1.03, & d_1 &\approx 2.4 \\ d_2 &\approx 1.04, & d_3 &\approx 5.4 \end{aligned} \tag{2.42}$$

Estimating the IOP

The IOP of the water can be quantified by inverting the model of surface (equation 2.39) or shallow (equation 2.40) waters. The IOPs are assumed as being the sum of IOPs from three constituents plus the sea-water molecules. These constituents are phytoplankton pigment (chlorophyll-a), dissolved organic matter (DOM) and suspended particulate matter (SPM). The IOP at wavelength λ can be parameterized as a function of its value at the blue (section 2.4). This approach will reduce the number of IOPs to three. These are: the absorption coefficients of chlorophyll-a and DOM at 0.44 μm and the backscattering coefficient of SPM at 0.4 μm. A further assumption is that the IOP can be parameterized as a function of constituents's concentration. This is true if the specific inherent optical property (SIOP) of each constituent is known. Measurements of the SIOPs in the North Sea were performed by IVM(2000)[11]. These measurements are used throughout this dissertation and assumed spatially and temporally homogenous. An important difference between the two models (equations 2.39 and 2.40) is the number of variables to be retrieved. This number will increase from 3-variables in the surface model to 5-variables in the shallow water model. This is because the shallow water model has two new variables, the first being the water depth and second being the bottom reflectance. Let us note

that this model implicitly assumed a homogenous water column (i.e. the IOP are constant over the water depth). In both models there is no unique solution for the inversion problem due to degeneracy effects (i.e. many-from-one). However, the degeneracy of the solution can be reduced by reducing the number of variables in the model. Therefore the surface model (equation 2.39) will be used throughout this work. This model of surface water can further be simplified (i.e. reduce the number of variables) in waters with one constituent. Open oceans are a very good example for this type where the water is optically governed by phytoplankton. All other constituents can be related to the water-content of phytoplankton. The one-component-simplification allows to introduce empirical models (i.e. bio-optical model) where pigment concentration is directly related to the measured water leaving reflectance. This type of water was classified as case-I waters (Morel 1977)[33]. On the other hand, areas of river outflow, sewage outfall, or intense land runoff, near the coasts, may contain large amounts of suspended sediments and dissolved organic material which can cause changes in the properties of the sea waters. This water with relative high concentrations of dissolved organic matter or/and suspended sediments is optically classified as case II waters. Due to their optical complexities, shallow bottom and neighboring land-surfaces, case II waters are the challenge for remote sensing applications.

Limitations

The used forward models (equation 2.39 and 2.40), however, are not appropriate for phytoplankton-rich waters. This is because both models omit the fluorescence effects. In this type of water the fluorescence signal (e.g. of chlorophyll-a) occurs between 0.668 and 0.695 μm (Kiefer 1994)[34]. These models are for un-polarized (also the RTE) light and they neglect:

- The source term and fluorescence effects (Kiefer 1994)[34].
- The effects of Raman scattering (Smith and Marshall 1994)[35].
- The effects of air bubbles (Terrill *et al.*, 2001[24] and Zhang *et al.*, 1998[36])
- The state of sea surface and bottom reflectance i.e. boundary conditions (Baker and Smith 1990[37], Mobley 1994[2]).

However taking the above effects into consideration will not achieve the (ever sought never reached) model closure (Zanveld 1994)[38]. Thus model

inversion will not be exact or even close to accurate. This might be due to the optical effect of large particles and the closure from single to bulk IOP (Carder and Castello 1994[39] and Morel 1994[40]) and the effects of polarization (Kattawar 1994)[41]. Let us note that the state of light polarization is not even considered in the equation (2.36) (Mobley 1994)[2].

2.5 Recorded reflectance

The total recorded radiance $L_t(\overrightarrow{X}, \theta_0, \theta, \phi - \phi_0, \lambda)$ at the sensor level is converted to reflectance $\rho_t^{(\lambda)}$:

$$\rho_t^{(\lambda)} = \frac{\pi L_t(\overrightarrow{X}, \theta_0, \theta, \phi - \phi_0, \lambda)}{\cos\theta_0 E_0^{(\lambda)}} \tag{2.43}$$

Where θ_0, θ are the sun and sensor zenith angles respectively with relative azimuth angle of $(\phi - \phi_0)$. The term $E_0^{(\lambda)}$ is the extraterrestrial solar irradiance (see appendix A, equation A-1). The viewing-geometry of all reflectance terms will be dropped for brevity. The reflectance is a relative measure, therefore it is preferable on radiance (Gordon 1997)[42]. The total received reflectance can thus be divided into three categories:

- The portion of photons that enters the water which is absorbed and scattered back to the sensor by water constituents ($\rho_w^{(\lambda)}$). This is the desired quantity that can be related to the ocean-surface layer physical and biological properties.
- The presence of atmosphere attenuates and scatters back a considerable amount of the incident radiation to the sensor ($\rho_{path}^{(\lambda)}$). This is the atmospheric path reflectance that never reaches to the water body.
- The still air-water surface reflects (sun glint) only about 2% ($\rho_{sfc}^{(\lambda)}$) of an unpolarized light normally incident upon it (Preisendorfer 1976)[1].

The recorded reflectance at the sensor level can be written as the sum of the above components:

$$\rho_t^{(\lambda)} = T_g^{(\lambda)} \left\{ T_v^{(\lambda)} \rho_{sfc}^{(\lambda)} + \rho_{path}^{(\lambda)} + T_v^{(\lambda)} \rho_w^{(\lambda)} \right\} \tag{2.44}$$

Where $T_g^{(\lambda)}$ and $T_v^{(\lambda)}$ are respectively the gaseous transmittance and the viewing diffuse-transmittance from ocean to sensor. The subscript of the

reflectance represents the contribution from surface reflectance (*sfc*), the atmospheric path (*path*) and water (*w*).

2.5.1 Gaseous transmittance

Any signal received at the sensor level will be attenuated by gaseous absorption. Only few gases produce observable absorption features in the spectral region between 0.4 μm and 1 μm (see table 2.1, source Jacobson 1999[43]).

Gas	absorption peak	comments
O_3	0.45-0.75 μm	vary with altitude
O_2	0.76 μm	spectral shift correction
H_2o	0.72, 0.82 and 0.94 μm	high variability

Table 2.1: Gaseous absorption-peaks with relative importance to the ocean color imagery.

The considered gases are ozone (O_3), oxygen (O_2) and water vapor (H_2o). The transmittance of any of these gases is affected by its vertical and spatial distributions in the atmosphere. Except for water vapor, these gases are uniformly mixed within each layer of the atmosphere and vary with height, season and wavelength. Therefore their transmittance can be, eventually, calculated knowing the altitude and the season (figure 2.6). Water vapor transmittance is the only spatial variable left to be evaluated. The water vapor content can be estimated from its absorption band

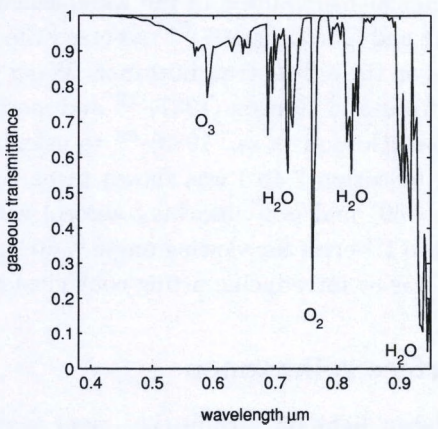

Fig. 2.6: The gaseous transmittance calculated by 6S for mid-latitude summer at 800 km altitude.

which is centered at 0.94 μm and its atmospheric window at 0.86-0.88 μm (Gao *et al.*, 2000)[44]. Gaseous transmittances are calculated using 6S (Vermote 1997)[45]. 6S uses the transmittance models of Goody (1964)[46] and Malkums(1967)[47]. The absorption features in figure (2.6) correspond to table (2.1). The narrow band of oxygen absorption at 0.76 μm can be used to correct for possible spectral shift in the sensor.

2.5.2 Diffuse transmittance

The diffuse transmittance of the atmosphere is approximated as (Gordon *et al.*, 1983)[48]:

$$T_v(\lambda, z) = \exp[-(0.5\tau_r(\lambda, z) + \tau_{Oz}(\lambda))/\cos(\theta)]t_a(\lambda, z) \tag{2.45}$$

where $\tau_r(\lambda, z)$ and $\tau_{Oz}(\lambda)$ are the optical thickness of Rayleigh and ozone respectively (see equation 2.18). The aerosol transmittance $t_a(\lambda, z)$ can be calculated as:

$$t_a(\lambda) = \exp[-(1 - \omega_a(\lambda)F(\lambda))\tau_a(\lambda)/\cos(\theta)] \tag{2.46}$$

where $F(\lambda)$ is the ratio of the forward scattering to the scattering coefficient. The terms $\omega_a(\lambda)$ and $\tau_a(\lambda)$ are the single scattering albedo and the optical thickness of aerosol. Let us note that these optical properties of aerosol ($F(\lambda)$,$\omega_a(\lambda)$ and $\tau_a(\lambda)$) are yet to be derived. Gordon *et al.* (1987)[49] has set the value of $t_a(\lambda)$ to unity. Morel and Gentili (1993[7] and 1996[8]) showed that the angular distribution of the water-leaving radiance field is non isotropic. Yang and Gordon (1997)[50] assessed the effects of this bidirectional properties on the diffuse transmittance. Wang (1999)[51] has build on the research of Yang and Gordon (1997)[50] and modified the previously suggested expression (Gordon *et al.*, 1983)[48] to calculate $t_a(\lambda)$. The analytical expression (equation 2.46) was shown to be within error of 4-5% for viewing angle $\leq 40°$ and non absorbing aerosol with $\tau_a(0.555) \leq 0.4$. This was improved to 1% error for viewing angle $\leq 60°$ and $\tau_a(0.555) \leq 0.6$. This improvement was by introducing fitting coefficients to equation (2.45).

2.5.3 Sea-surface reflectance

About 98% of incident light on a calm (i.e. flat) water surface is transmitted to the water. The other 2% are reflected back to the atmosphere (Preisendorfer 1976)[1]. In general the sea surface exhibits specular and dif-

fuse reflections. The surface reflectance can be divided to direct (dr) and diffuse (df) components:

$$\rho_{sfc}^{(\lambda)} = \rho_{dr}^{(\lambda)} + \rho_{df}^{(\lambda)} \tag{2.47}$$

Note that the whitecaps reflectance is assumed negligible for wind speed below 8 m/s (see table II in Koepke 1984[52]). The diffuse reflectance is relatively small for clear or uniform sky conditions. For wind speed ≥ 4 m/s it takes a value of 0.057% (Burt 1954[53], see Preisendorfer 1976[1]). The direct reflectance (sun glint) can be derived using the model of Cox and Munk (1954)[54] and[55]. This model is based on Fresnel reflectance $\rho_F(\psi/2)$ and the slope-probability-distribution of the wave facets g:

$$\rho_{dr}^{(\lambda)} = \frac{\pi}{4\mu_0\mu\mu_n^4}\rho_F(\psi/2)g(\tan\theta_n) \tag{2.48}$$

Where μ, μ_0 and μ_n are the cosines of the observation θ, solar zenith θ_0, and the normal of the facet θ_n angles respectively. ψ is the angle between observed and reflected light, and can be written as Gordon (1997)[42]:

$$\cos(\psi) = \cos(\theta)\cos(\theta_0) - \sin(\theta)\sin(\theta_0)\cos(\phi_0 - \phi) \tag{2.49}$$

Where $\phi_0 - \phi$ is the difference between the azimuth angles of incident ϕ_0 and observed ϕ light. θ_n is the angle between facet's normal and the zenith of which specular reflection occurs. It can be calculated from Cox and Munk (1954)[55]:

$$\theta_n = \cos^{-1}\left(\frac{\mu_0 + \mu}{2\cos(\psi/2)}\right) \tag{2.50}$$

The probability of specular reflection in the direction of the observer (μ, ϕ) is (e.g. see Thomas and Stamnes 1999[5]):

$$g(tan\theta_n) = \frac{1}{\pi\sigma^2}\exp[-tan^2(\theta_n)/\sigma^2] \tag{2.51}$$

Where σ is the standard deviation of facets slops which is assumed to be independent of wind direction:

$$\sigma^2 = 0.03 + 0.00512W \tag{2.52}$$

Where W is the wind velocity in m/s. Fresnel reflectance can be calculated

as:

$$\rho_F(\theta_r) = 0.5 \left\{ \left[\frac{\sin(\theta_r - \theta_t)}{\sin(\theta_r + \theta_t)} \right]^2 + \left[\frac{\tan(\theta_r - \theta_t)}{\tan(\theta_r + \theta_t)} \right]^2 \right\} \tag{2.53}$$

Where θ_r and θ_t are the zenith angle of reflected and the transmitted light respectively. These two angles are linked through Snell's law:

$$n_a \sin\theta_r = n_w \sin\theta_t \tag{2.54}$$

Where n_a and n_w are the index of refraction of the air and the water medium. Figure (2.7) shows the specular reflection with different geometry sets-up. The main observation is that the reflected fraction of the incident solar irradiance on the sea surface will decrease with roughened surface.

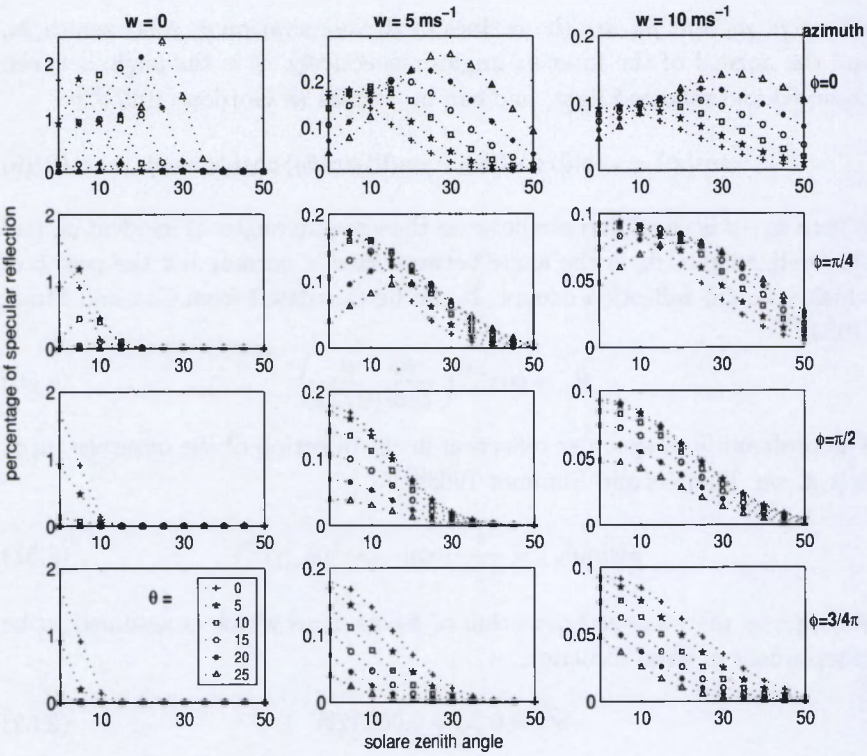

Fig. 2.7: Sun glint as a function of wind speed and illumination-viewing geometry (equation 2.48). Each curve is for a viewing angle that varies from 0 to 25 degrees at an interval of 5 degrees (see the legend).

Thus assuming a still sea-surface will underestimate the amount of solar radiation penetrating the sea surface. Another interesting feature in figure (2.7) is that the influence of the viewing angle on the surface reflectance is inverted at the azimuthal plans $\pi/2$ and $3/4\pi$.

2.5.4 Atmospheric path

The light through its path in the atmosphere experiences several scattering events. This is due to the presence of air molecules and the suspended particles in the atmosphere (aerosol). The scattering of aerosol and air molecules can be treated as separated terms i.e. aerosol scattering in the absence of molecules and molecules scattering in the absence of aerosol (conventionally, homogenous scattering). The interaction between the two scattering events (coupled term) can be accounted for, independently (Deschamp *et al.*, 1983)[56]. i.e. a photon that is scattered by aerosol particles and then by air-molecules or vice versa (conventionally heterogeneous scattering). Thus the atmospheric path can be written as:

$$\rho_{path}^{(\lambda)} = \rho_a^{(\lambda)} + \rho_r^{(\lambda)} + \rho_{ra}^{(\lambda)} \tag{2.55}$$

Where the subscripts a and r and ra are respectively the reflectances due to aerosol, air molecules and coupled scattering.

Air molecules scattering

The blue color of the sky is the direct cause of the Rayleigh scattering of air molecules to solar light. The scattered light intensity in the Rayleigh regime is proportional to λ^{-4} of the incident light. The calculation of Rayleigh scattering of air molecules is well described in terms of geometry and pressure (e.g. equation 2.58). The optical thickness of air molecules at altitude z can be calculated from Hansen and Travis (1974)[57]:

$$\tau_r(\lambda, z) = 0.008569\lambda^{-4}(1 + 0.0113\lambda^{-2} + 0.00013\lambda^{-4})P(z)/P(0) \tag{2.56}$$

Where λ is the wavelength in μm and P(0)=1013.25 mb is the standard atmosphere pressure at the sea surface. A simpler relation to calculate the Rayleigh optical thickness at the top of atmosphere can be found in Sturm (1980)[58]. The scattering phase function $\widetilde{\beta}_r(\lambda, \psi)$ in the Rayleigh regime

can be approximated as:

$$\widetilde{\beta}_r(\psi, \lambda) = \frac{1}{4}(1 + \cos^2(\psi)) \tag{2.57}$$

Where ψ is the scattering angle (i.e. the angle between the incident light and the scattered beam).

Aerosol scattering and coupled term

Mie scattering of aerosol particles is one of the most significant contributor to the total received reflectance. Aerosol particles do not have a known (unless measured) concentration or physical chemical composition. Moreover, aerosol optical properties vary with time and place. These optical properties have to be known at the time of image acquisition. This is to quantify the aerosol scattering that enters the field of view (FOV) of the sensor. Approximations of the aerosol optical properties (in the same manner as it was done for Rayleigh scattering) are constrained by this variability. Measurements of aerosol optical properties have spatial and temporal limitations. Due to these difficulties, the aerosol scattering has to be directly quantified from measured reflectance. This will be our main objective in developing an atmospheric correction algorithm. The atmospheric path reflectance is calculated using the successive order of scattering (see Vermote 1997[45]). Figure (2.8) illustrates the reflectance due to the aerosol scattering received

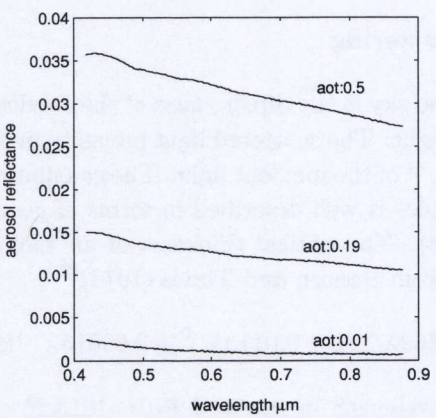

Fig. 2.8: The reflectance of maritime aerosol at 4km altitude, nadir viewing and 40° sun zenith. Three aerosol optical thicknesses (aot) are shown, namely 0.01, 0.19 and 0.5. These spectra were generated with the 6S package.

at sensor level as a function of wavelength and aerosol optical thickness. The atmospheric contents of water vapor and ozone were assumed H_2o = 2.93 cm and O_3 = 0.319 cm. Figure (2.8) shows that for a giving geometry (sun-target-sensor), concentrations of water vapor and ozone and aerosol type the atmospheric reflectance is a direct function of the aerosol optical thickness.

Single scattering approximation

Single scattering means that the photon has experienced one scattering event. Thus no further scattering by adjacent molecules or particles. Moreover there is no interaction between different scatterers (i.e. $\rho_{ra}^{(\lambda)} = 0$). In the single scattering regime the scattering reflectance of a component x ($x = a$ for aerosol and $x = r$ for air molecules) above a flat sea surface can be approximated as:

$$\rho_x^{(\lambda)} = \omega_x(\lambda)\tau_x(\lambda, z)\beta_x^{'}(\lambda, \psi)/4\cos(\theta_0)\cos(\theta) \tag{2.58}$$

Where:

$$\beta_x^{'}(\lambda, \psi) = \left(\widetilde{\beta}_x(\lambda, \psi_-) + [\rho_F(\theta) + \rho_F(\theta_0)]\widetilde{\beta}_x(\lambda, \psi_+)\right) / \cos(\psi) \tag{2.59}$$

The terms $\omega_x(\lambda)$, $\tau_x(\lambda, z)$ and $\widetilde{\beta}_x(\lambda, \psi)$ are respectively the single scattering albedo, optical thickness and scattering phase function for a component x (aerosol or air molecules). The scattering angle ψ can be calculated from the viewing-illumination geometry. i.e. sun (θ_0,ϕ_0) and sensor (θ,ϕ) zenith and azimuthal angles (similar to equation 2.49):

$$\cos(\psi_\pm) = \pm\cos(\theta)\cos(\theta_0) - \sin(\theta)\sin(\theta_0)\cos(\phi_0 - \phi) \tag{2.60}$$

Where: $\rho_F(\theta)$ is the Fresnel reflectance of an incident angle θ (equation 2.53). The term ψ_- represents the contributions of aerosol/Rayleigh scattering to the total signal entering the sensor's FOV. The term ψ_+ accounts for the specularly-reflected light at the sea surface (outside the FOV) that is scattered into the sensor's FOV ($\rho_F(\theta_0)$ term). Or, equivalently, those photons that are scattered, by air molecules or aerosol, towards the sea surface and then specularly reflected from the surface into the observer FOV (the term involving $\rho_F(\theta)$). The accuracy of the single scattering approximation for Rayleigh scattering is within 3-4% compared to the exact solution of the scalar (i.e. the polarization effects are neglected) radiative transfer

equation (Gordon *et al.*, 1988)[59]. Moreover the assumption of a flat sea surface will introduce an error to the calculated Rayleigh reflectance equivalent to $\pm$ 15 mb in the atmosphere surface pressure (Gordon and Wang 1992)[60]. For roughened sea surface the Fresnel reflectance term has to be replaced by the bidirectional reflectance distribution function. Figure(2.9) shows the results of the single scattering approximation (with flat surface) and successive order of scattering with wind roughened surface (wind speed of 5 m/s). Let us note that the best results of the single scattering approximation of Rayleigh reflectance are at the NIR part of the spectrum. This is because the magnitude of Rayleigh scattering and surface reflectance at the NIR wavelengths are very small. In consequence there is a small probability that the scattered photon (from air molecule or sea surface) hits another air molecule. In other word the coupled term is negligible.

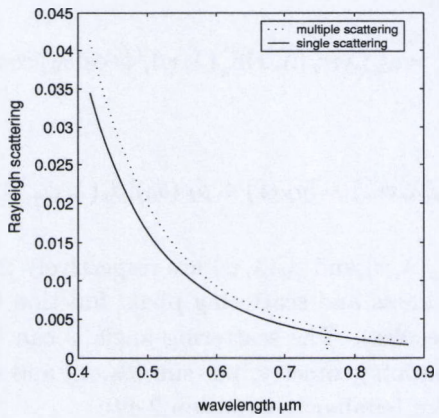

Fig. 2.9: Rayleigh scattering-reflectance (received at 4km) calculated using the single scattering (equation 2.58) and successive order of scattering (6S). The solar zenith is 40° and the viewing angle is at nadir.

On the other hand, the single scattering approximation for aerosol reflectance is only correct in the limit $\tau_r(\lambda, z)/\cos(\theta) \longrightarrow 0$, i.e. small aerosol optical thickness. For this type of aerosol the phase scattering function and the single scattering albedo can be assumed independent of wavelengths. The ratio of aerosol reflectance at two wavelengths is (see equation 2.58):

$$\varepsilon^{s}_{(\lambda_i,\lambda_j)} = \frac{\rho_a^{(\lambda_i)}}{\rho_a^{(\lambda_j)}} = \frac{\tau_{a(\lambda_i)}\omega_{(\lambda_i)}\beta'_a(\lambda_i,\psi)}{\tau_{a(\lambda_j)}\omega_{(\lambda_j)}\beta'_a(\lambda_j,\psi)} \tag{2.61}$$

The above equation can be reduced to:

$$\varepsilon^{s}_{(\lambda_i,\lambda_j)} \approx \frac{\tau_{a(\lambda_i)}}{\tau_{a(\lambda_j)}} \tag{2.62}$$

Let us note that the aerosol optical thickness is proportional to the concentration which will be cancelled out in the ratio (2.62). Thus, physically, Epsilon ratio $\varepsilon^{s}_{(\lambda_i,\lambda_j)}$ represents the relative strength of aerosol scattering and is independent of aerosol concentrations. Let us assume that the aerosol optical thicknesses vary with wavelength according to Gordon *et al.* (1983)[48]:

$$\tau_{a(\lambda_i)} = \left(\frac{\lambda_j}{\lambda_i}\right)^{\bar{n}} \tau_{a(\lambda_j)} \tag{2.63}$$

The Angstrom exponent $\bar{n}$ describes the spectral shape (i.e. dependency on wavelength) of the aerosol scattering. The ratio $\varepsilon^{s}_{(\lambda_i,\lambda_j)}$ can then be simplified to:

$$\varepsilon^{s}_{(\lambda_i,\lambda_j)} \approx \left(\frac{\lambda_j}{\lambda_i}\right)^{\bar{n}} \tag{2.64}$$

This spectral-extrapolation formula is valid for wavelengths $< 0.67\mu m$. This was adapted for longer wavelengths and SeaWiFS spectral bands such as (Gordon and Wang 1994)[61]:

$$\varepsilon^{s}_{(\lambda_i,\lambda_j)} = \exp\left[c\left(\lambda_i - \lambda_j\right)\right] \tag{2.65}$$

Where: c is a constant depending on the viewing geometry and aerosol model. From equation (2.65) we can spectrally extrapolate $\varepsilon^{s}_{(\lambda_i,\lambda_j)}$ to other wavelengths such:

$$\varepsilon^{s}_{(\lambda_k,\lambda_j)} = \left(\varepsilon^{s}_{(\lambda_i,\lambda_j)}\right)^{\delta_k} \tag{2.66}$$

Where the exponent δ_k can be determined from equation (2.65):

$$\delta_k = \frac{\lambda_j - \lambda_k}{\lambda_j - \lambda_i} \tag{2.67}$$

However, the use of equations (2.66 and 2.67) will result in an underestimation of the water signal at the blue wavelengths as it will be shown in chapters (4 and 5).

2.6 Retrieving the water leaving reflectance

The water leaving reflectance (equation 2.39) is the desired quantity that is related to the sea water physical and biological properties. Extracting this quantity from the total received reflectance is conventionally called atmospheric correction. The calculation of Rayleigh scattering of air molecules is well described in terms of geometry and pressure (e.g. equations 2.56 and 2.57). The sea surface reflectance is generally small and it can be estimated using statistical relationships and wind speed of (Cox and Munk 1954[54], and[55] and Thomas and Stamnes 1999[5]; equations 2.48 and 2.51). The gaseous transmittance can be calculated from ancillary data on ozone and water vapor concentrations using the 6S code (Vermote *et al.*, 1997)[45]. The viewing diffuse transmittance is approximated following Gordon *et al.* (1983)[48], equation (2.45). This leaves the aerosol and the coupled term reflectances and the water leaving reflectance to be derived. This requires knowledge (or assumptions) about the aerosol concentration and composition. The measurements of aerosol optical and physical properties are difficult to obtain. Thus the empirical determination of the aerosol scattering derived from remote sensing imagery is highly desired. Note that exceptional situations will not be treated. These exceptional situations are: large viewing or sun zenith angles, hot spot, windy conditions causing whitecaps and absorbing aerosol. These phenomena may occur in any acquired image regardless of the sensor. However the image can be corrected for nadir viewing angle and normalized for the sun zenith angle. Hot spot can be avoided by tilting the sensor, a capability that exists in most sensors. Good weather and clear sky are necessary conditions to perform high quality spectral measurements. Other algorithms are definitely needed to treat the presence of absorbing aerosol (Zhao and Nakajima 1997[62]; Gordon *et al.*, 1997[63]; Chomko and Gordon 1998[64]).

The aerosol multiple-scattering ratio at two wavelengths (short s and long l) can be written as:

$$\varepsilon_{(s,l)} = \frac{\rho_a^{(s)} + \rho_{ra}^{(s)}}{\rho_a^{(l)} + \rho_{ra}^{(l)}} \tag{2.68}$$

The aerosol ratio in (2.68) can be linked to $\varepsilon_{(s,l)}^{s}$ (equation 2.61) by dividing

its dominator and nominator over $\rho_a^{(l)}$:

$$\varepsilon_{(s,l)} = \varepsilon^s_{(s,l)} \left(\frac{1 + \rho_{ra}^{(s)}/\rho_a^{(s)}}{1 + \rho_{ra}^{(l)}/\rho_a^{(l)}} \right) \tag{2.69}$$

If the band l is situated far in the NIR, then the contribution from the coupled term is negligible. This is due to the small Rayleigh scattering in this part of the spectrum. Equation(2.69) can then be reduced to:

$$\varepsilon_{(s,l)} = \varepsilon^s_{(s,l)} \left(1 + \frac{\rho_{ra}^{(s)}}{\rho_a^{(s)}} \right) \tag{2.70}$$

Gordon and Castano (1987)[49] showed that the above relationship (2.70) is linear. The single scattering aerosol ratio can thus be linked to its counterpart in the multiple scattering regime with a linear relationship. This is true if the band l is situated in the NIR part of the spectrum. Once the value of $\varepsilon_{(s,l)}$ is estimated, the water leaving reflectance at the shorter channel (s) is (from equation 2.44):

$$T_v^{(s)} \rho_w^{(s)} = \rho_c^{(s)} - \varepsilon_{(s,l)} \times \left(\rho_c^{(l)} - T_v^{(l)} \rho_w^{(l)} \right) \tag{2.71}$$

Where the corrected-reflectance is defined as the total reflectance corrected for gaseous absorption and Rayleigh/surface reflectances:

$$\rho_c^{(\lambda)} = \frac{\rho_t^{(\lambda)}}{T_g^{(\lambda)}} - \rho_r^{(\lambda)} - T_v^{(\lambda)} \rho_{sfc}^{(\lambda)} \tag{2.72}$$

The unknowns in equation (2.71) are the water signal at two wavelengths and the aerosol ratio. The number of variables can be reduced by introducing some assumption on the water leaving reflectance at channel l. If this band lies far in the NIR then the water signal at l can be assumed negligible (Gordon 1978)[65]. Equation (2.71) becomes:

$$\rho_w^{(s)} = \frac{\rho_c^{(s)} - \varepsilon_{(s,l)} \rho_c^{(l)}}{T_v^{(s)}} \tag{2.73}$$

If the two bands s and l are at the NIR then the above approach can be adjusted as following. The water leaving reflectance is to the first order proportional to the water inherent optical properties (equation 2.39). At the NIR spectral region the water signal is approximated as being optically gov-

erned by suspended particulate matter (SPM) and water molecules. Thus the absorption and the backscattering coefficients are, respectively, approximated as:

$$\begin{aligned} b_b(\lambda) &= b_b^*(\lambda) \times C \\ a(\lambda) &= a_w(\lambda) \end{aligned}$$

Where $a_w(\lambda)$ is the absorption coefficient of sea-water. The quantities $b_b^*(\lambda)$ and C are respectively the specific backscattering coefficient and the concentration of SPM. The ratio of the water leaving reflectances at the two bands s and l is:

$$\alpha_{(s,l)} = \frac{T_o^{(l)} \rho_w^{(s)}}{T_o^{(s)} \rho_w^{(l)}} \tag{2.74}$$

Where $T_o^{(\lambda)}$ is the sun to sea transmittance. Substituting the right hand side of equation (2.39) in the ratio (equation 2.74) gives:

$$\alpha_{(s,l)} = \frac{b_b^*(s)}{b_b^*(l)} \times \frac{a_w(l) + b_b(l)}{a_w(s) + b_b(s)} \tag{2.75}$$

The parameter $\alpha_{(s,l)}$ is expected to be a smooth function of total suspended matter concentration. This ratio was assumed constant (Carder *et al.*, 1999[66] and[67], Ruddick *et al.*, 2000[68], Hue *et al.*, 2000[69]). This assumption can be explained as following. At the NIR wavelengths the water can be considered as optically clear due to the absorption by water molecules. In this water (optically clear) the following approximation can be applied (Kirk 1991)[70]:

$$\rho_w^{(\lambda)} = 0.33 \frac{b_b(\lambda)}{a(\lambda)} \tag{2.76}$$

This is valid when the following criteria is satisfied:

$$b_b(\lambda)/a(\lambda) \leq 0.25 \tag{2.77}$$

At the NIR the backscattering coefficient can be assumed spectrally flat (Gould 1999)[71], thus substituting equation (2.76) in the ratio (equation 2.74) gives:

$$\alpha_{(s,l)} \approx \frac{a_w(l)}{a_w(s)} \tag{2.78}$$

A further simplification can be imposed (Ruddick *et al.*, 2000)[68]:

$$\frac{T_v^{(s)} T_o^{(s)}}{T_v^{(l)} T_o^{(l)}} = 1$$

Thus;

$$\frac{T_v^{(s)}}{T_v^{(l)}} \frac{\rho_w^{(s)}}{\rho_w^{(l)}} = \alpha_{(s,l)} \tag{2.79}$$

Then the water leaving reflectance at wavelength s can be calculated by substituting (2.79) in (2.71):

$$\rho_w^{(s)} = \alpha_{(s,l)} \frac{\rho_c^{(s)} - \varepsilon_{(s,l)} \rho_c^{(l)}}{T_v^{(s)} \left(\alpha_{(s,l)} - \varepsilon_{(s,l)}\right)} \tag{2.80}$$

Equation (2.73) is used for clear waters (chapter 3). On the other hand equation (2.80) is used for turbid waters (section 3.3.3 and chapters 4 and 5).

2.7 Conclusion and remarks

The inherent optical properties of the water column define exactly its apparent optical properties. These apparent optical properties can be measured and linked to the inherent optical properties. The concentrations of water constituents can be retrieved from the inherent optical properties knowing the specific inherent optical properties of these constituents. These specific inherent optical properties are related to the particle's index of refraction and particle-size distribution. However, in optically complex waters, there is no unique estimation of the water inherent optical properties.

The reflectance at the sensor level has to be corrected for atmospheric and surface signals. This is to retrieve the water signal which is an apparent optical property. The air molecules and surface reflectance can be estimated knowing geometry, pressure and wind speed.

An interesting feature of the NIR is that the water absorbs most of the transmitted solar radiation. Thus the backscattered reflectance is expected to be very small and spatially flat in clear waters. This low-signal can either be neglected or approximated by a known constant-value. Therefore the magnitude of the aerosol scattering at this wavelength can be assessed from the corrected reflectance (equation 2.72). Another wavelength is needed to

resolve the spectral dependency of the aerosol scattering (i.e. the constant c in equation 2.65). Thus, it is sufficient to have two channels situated at the NIR to retrieve the water leaving reflectance at any wavelength i. In turbid waters the water leaving reflectance at the NIR is no longer constant and varies with water turbidity. Nevertheless the ratio of the water leaving reflectance, at two NIR bands, can be assumed constant. This leaves the aerosol ratio to be estimated. In optically complex waters (high water turbidity) the water ratio will vary with turbidity (Li 2003)[72]. In this situation the aerosol and the water ratio have to be retrieved simultaneously (e.g. chapter 5).

Chapter 3

Transformation technique to atmospherically correct AVHRR images

Abstract

The hypothesis of negligible water leaving reflectance at the near infrared NIR channels was successful for clear waters (Gordon 1978)[65]. At shorter wavelengths, the clearest pixels in a scene are assumed to have a known water leaving reflectance (Gordon and Clark 1981)[73]. Over these pixels, the aerosol ratio can be evaluated and assumed constant for a sub scene in the image. This can be replaced by the visual inspection of corrected reflectance scatter-plot (Ruddick *et al.*, 2000)[68]. Iterative methods are increasingly used with relationships between the water leaving signals at different bands (Andre and Morel 1991)[74]. However localizing a clear water region is quite difficult in the southern bight of the North Sea using the red band of AVHRR image. The visual inspection is time consuming and subjective to user error. Iterative procedures are vulnerable to degeneration effects and they need empirical relationships.

We propose to define the aerosol-dominant pixels instead of the clear water pixels. The aerosol ratio can then be estimated over these pixels from regression. This chapter was accepted for publication as Salama *et al.* (2003)[75].

3.1 Intoduction

The general approach of atmospheric correction of ocean color imagery relies on identifying a spectral range in which reasonable assumptions on the water leaving reflectance can be introduced. For case-I waters (Morel and Prieur 1977)[33] the water leaving reflectances at the near infrared (NIR) channels can be assumed zero (Gordon 1978)[65]. This will give an estimate of the aerosol reflectances at the NIR channel (e.g. CZCS or AVHRR). At a shorter wavelength, the clearest pixels in the scene are isolated assuming known water leaving reflectance (Gordon and Clark 1981)[73]. Over these pixels, the aerosol ratio (equation 2.64) can be evaluated and assumed constant for a sub scene in the image. This procedure is illustrated in figure (3.1). In this figure there is a general flow chart for sensors with one or two NIR bands. This is to achieve the link to the chapter (4). This approach can be extended by using initial values of the Angstrom exponent (obtained from figure 3.1) and water leaving reflectance (e.g. zero assumption) at the NIR channels. In consequence the water leaving reflectance at the shorter wavelengths can be calculated. To infer the Angstrom exponent directly from the image other relationships might be needed. The idea is to use these relationships to calculate backwards and evaluate till a convergence in the sought value is achieved. Logically the relationship is a bio-optical model (e.g. equation 2.39) that extracts concentration from reflectance (i.e. to allow backward calculation). The use of a bio-optical model tacitly assumes a single constituent that has to be extracted for the backward calculation. That narrows (again) the applicability of such a model to case-I waters where chlorophyll-a is the only constituent to be quantified. The output of the bio-optical model (i.e. concentration) is compared with the clear water threshold (e.g. 2 $mg.m^{-3}$ of Chl-a, Bricaud and Morel 1987[76]). If it is a clear-water-pixel then the reflectance of water and aerosol are recalculated (backward) from the concentration. The Angstrom exponent is again estimated. If the pixel is turbid the Angstrom exponent takes the value of the previous pixel (clear water). After having processed all the pixels in the scene the Angstrom exponent is averaged and compared to the initial value. This loop is continued till a convergence is realized. Bricaud and Morel (1987)[76] developed such an approach to simultaneously correct the image and estimate the pigment concentrations. The Angstrom exponent in the above approaches is an average value over the clear water pixels. This is valid if the aerosol type (i.e. particle size distribution composition, and refractive index) and optical thickness are constant. Ac-

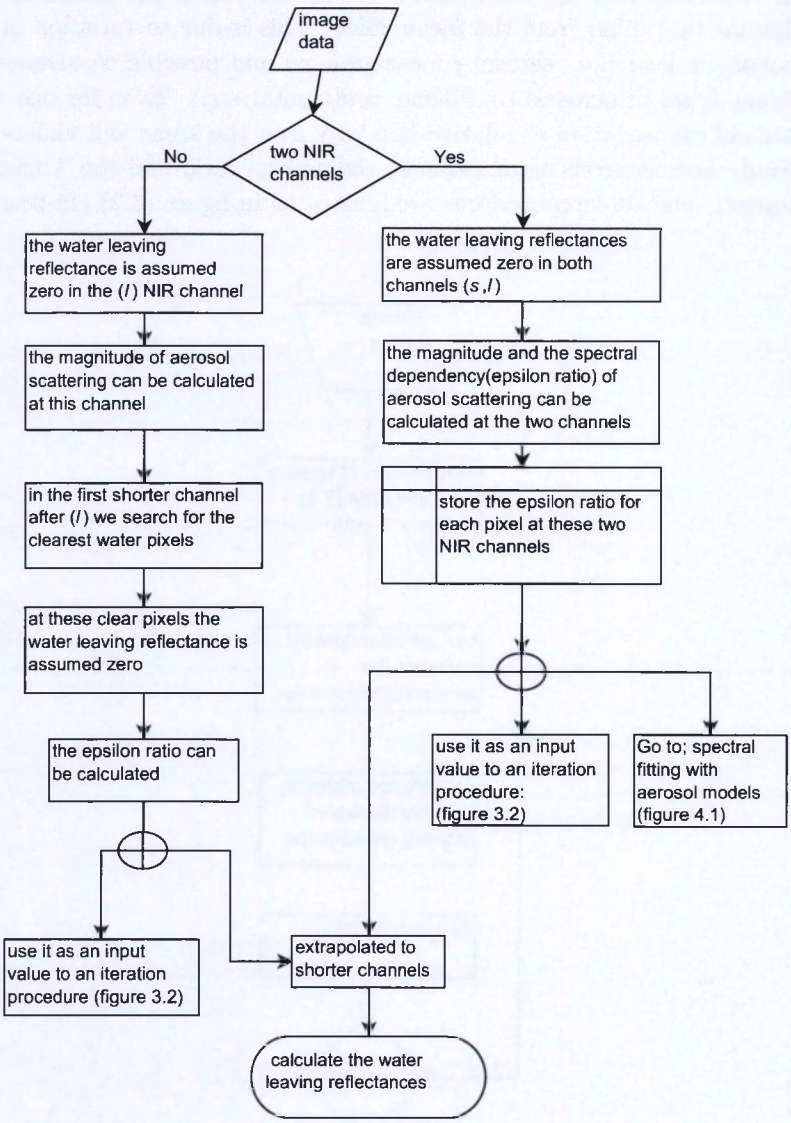

Fig. 3.1: Flow chart for the starting steps to atmospherically correct an image with 2 or less NIR bands.

tually the Angstrom exponent (and hence aerosol ratio) will exhibit spatial variations that differ from the mean value. This is due to variation in the atmospheric load (i.e. aerosol concentrations) and possible coexistence of different types of aerosols (maritime, continental *etc.*). Even for one type of aerosol the variation in relative humidity over the scene will violate the spatially homogeneous assumption of the aerosol ratio and the Angstrom exponent. The above procedures are illustrated in figure (3.2). In practice

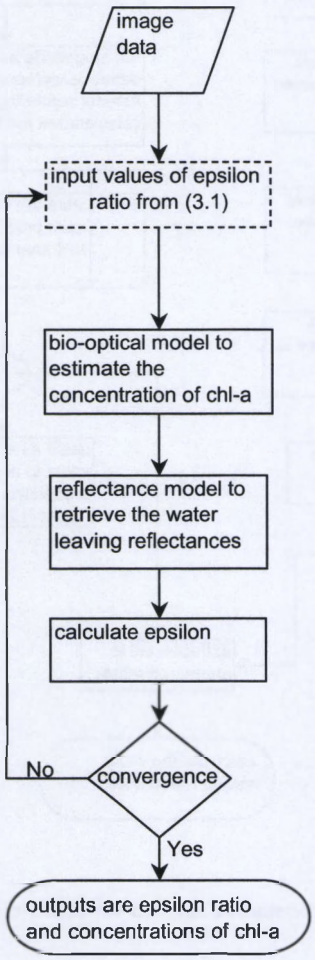

Fig. 3.2: Using bio-optical model to perform the atmospheric correction in an iterative manner.

the values of aerosol ratio has been set to one to retrieve positive water leaving reflectances for AVHRR images (Vos *et al.*, 1997[77] and 1998[78]). This value is reasonable for a maritime aerosol model at high relative humidity.

This study proposes a technique to atmospherically correct AVHRR images, modified from Gordon (1978)[65]. However instead of searching for a clear water region at the red band, the algorithm searches for an aerosol dominant region at the red and the NIR AVHRR bands. The idea is that, the aerosol reflectances will be always present in the scene of an AVHRR image. On the other hand it is difficult to allocate a clear water region in the southern bight of the North Sea. The proposed technique is based on the principal component transformation of the AVHRR image. The resulting images are used to classify the aerosol dominant pixels. The aerosol ratio was then estimated over these pixels from regression.

3.2 Method

The Advanced Very High Resolution Radiometer (AVHRR) sensors have one visible band (s : $0.58 - 0.68$ μm), one NIR band (l : $0.725 - 1.1$ μm) and three thermal bands. The AVHRR sensor proved to be efficient for suspended particulate matter (SPM) quantification (Althuis and Shimwell 1995)[79]. However, about 76% of the signals at the red band are due to the atmospheric path (Sturm 1980)[58]. Therefore, the quality of the retrieved geophysical quantities is directly related to the accuracy of the atmospheric correction algorithm. There are always aerosols present in the atmosphere that vary in composition and concentration. An approach is to utilize the fact that the total recorded reflectance at AVHRR NIR band is mainly (95% Sturm 1980[58]) due to aerosol scattering. Moreover the water at this band is optically clear (high absorption coefficient). Thus aerosol dominant pixels can always be allocated in the scene. The aerosol ratio can then be estimated over pixels with high aerosol optical thickness. This is because the retrieved aerosol ratio will be less affected by the water signal. This is contrary to searching clear water region which in most cases does not exist (strictly speaking for the North Sea and AVHRR spectral bands). Having aerosol-dominant pixels isolated, the ratio $\varepsilon_{(s,l)}$ will be approximately equal to the slope of the regression line for these pixels. Thus the aerosol dominant pixels have to be classified before finding their relationship at both bands. In principle the retrieved water leaving reflectance should have a small correlation with the aerosol reflectance. In other words the covari-

ance should be small or zero. A straight forward technique, to de-correlate different contributors, is the principal component transform (PCT). The new components are linear combinations of the original data (Emery and Thomson 2001)[80]:

$$PCT = \begin{bmatrix} PC1 \\ PC2 \end{bmatrix} = \begin{bmatrix} g_{ii} & g_{ij} \\ g_{ji} & g_{jj} \end{bmatrix} \begin{bmatrix} \rho_c^{(\lambda i)} - \bar{\rho}_c^{(\lambda i)} \\ \rho_c^{(\lambda j)} - \bar{\rho}_c^{(\lambda j)} \end{bmatrix} \tag{3.1}$$

Where the first term at the right hand side of equation (3.1) is the eigenvector of the covariance matrix of $(\rho_c^{(\lambda i)}, \rho_c^{(\lambda j)})$. The mean corrected reflectance at wavelength λ is $\bar{\rho}_c^{(\lambda)}$. This is a rotation-translation of the axes which will catch most of the data variance in the first axis (PC1). These variations are mainly due to atmospheric perturbation. The second axis (PC2) will contain very little variance, which is due to water-signal and some anomalies (Richards 1994)[81]. The rotation angle of the first principle (θ_{pc1}) with respect to the horizontal (w.r.t.h.) can be related to the angle of the regression line (θ_{reg}) (w.r.t.h.) of the data set (Aage *et al.*, 1998)[82]:

$$\tan 2\theta_{pc1} = r \tan 2\theta_{reg} \tag{3.2}$$

Where r is the correlation coefficient between corrected reflectances at the two bands. For high correlation coefficient ($r > 0.9$), the regression line will therefore be a good approximation of the PCT. The interpretation of data variations on the new axes is related to the position of the NIR band being used. This will be more clear in chapter (4).

3.3 Results and discussion

3.3.1 The data-set

For this exercise we use a cloud-free AVHRR image (figure 3.3) with simultaneous in-situ measurements (table 3.2). The image was calibrated and converted to reflectance for channels 1 & 2 and temperatures for channels 3, 4, and 5. The land and cloud were masked using the algorithm of Sospedra *et al.* (2000)[83]. The total reflectances at AVHRR visible channels were corrected for Rayleigh scattering and surface reflectance. Ancillary data of ozone and water vapour transmittance were used (from the SeaWiFs project) to generate gaseous transmittance values using the 6S code (Vermote *et al.*, 1997)[45].

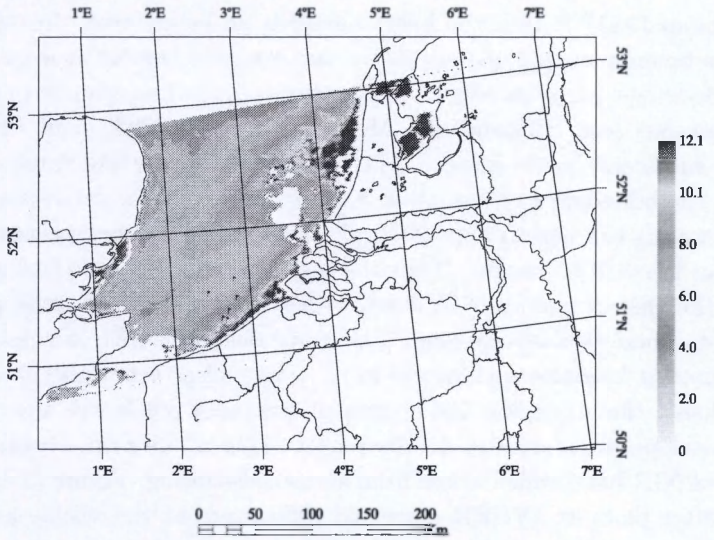

Fig. 3.3: The aerosol reflectance (%) at the NIR band of AVHRR. The image was acquired on 27-April 1999 at 15:04 UT. The flags are the sampling sites.

3.3.2 Clear waters

Let us assume that the received reflectance at AVHRR NIR band is due to atmospheric path, i.e. $\rho_c^{(l)} \equiv \rho_a^{(l)} + \rho_{ar}^{(l)}$. This assumption reduces the reflectance equation to (equation 2.73):

$$\rho_w^{(s)} = \frac{\rho_c^{(s)} - \varepsilon_{(s,l)}\rho_c^{(l)}}{T_v^{(s)}} \tag{3.3}$$

The ratio $\rho_c^{(s)}/\rho_c^{(l)}$ imposes boundaries on the sought aerosol ratio. For a non-absorbing aerosol and non negative water leaving reflectance the boundaries for $\varepsilon_{(s,l)}$ are :

$$1 \leq \varepsilon_{(s,l)} \leq \frac{\rho_c^{(s)}}{\rho_c^{(l)}} \tag{3.4}$$

The upper bound is simply to guarantee positive reflectance. The lower bound implicitly assumes that there is always non-absorbing aerosol in the atmosphere. The coupled term $\rho_{ra}^{(\lambda)}$ at the NIR is relatively small due to the negligible Rayleigh scattering at this wavelength interval. Lower bound can be accepted except for the extensive multi-scattering regime (occurring at the scan edge). In this regime the coupled term might be negative

(Deschamp 1983)[56] thus the lower bound is no longer true. In this exercise the bounds on $\varepsilon_{(s,l)}$ (equation 3.4) are assumed correct at least for our example-image (no scan edge). This ratio $\varepsilon_{(s,l)}$ is then assumed spatially homogeneous (e.g. Bricaud and Morel 1987[76], Ruddick *et al.*, 2000[68]) over a sub-scene in the image. The task is to allocate the value of $\varepsilon_{(s,l)}$ within the boundaries of (equation 3.4). For a very clear atmosphere over turbid waters the signal at the NIR, $\rho_c^{(l)}$, is very small in comparison to the signal at the visible channel. Thus the regression line between turbid water pixels (for the red and the NIR bands of AVHRR) will have a small positive slope at a moderate aerosol load. This slope decreases with increasing visibility until it becomes asymptotic to $\rho_c^{(s)}$ (very clear atmosphere). On the other hand, the regression line of aerosol dominant pixels will have a steep positive slope, with angle $\leq 45°$ (w.r.t.h.). This is due to the contribution from the NIR band which arises from aerosol scattering. Figure (3.4) shows the scatter plots of AVHRR corrected reflectance at the visible and NIR bands and its PCT transform. The PCT (figure 3.4(b)) is a better representative to spectral behavior of the data set (figure 3.4(a)) at both bands. The translation of the transform is equal to the mean reflectance at each band $(\bar{\rho}_c^{(s)}, \bar{\rho}_c^{(l)})$. The rotation angle of the PC1 (w.r.t.h.) can be calculated

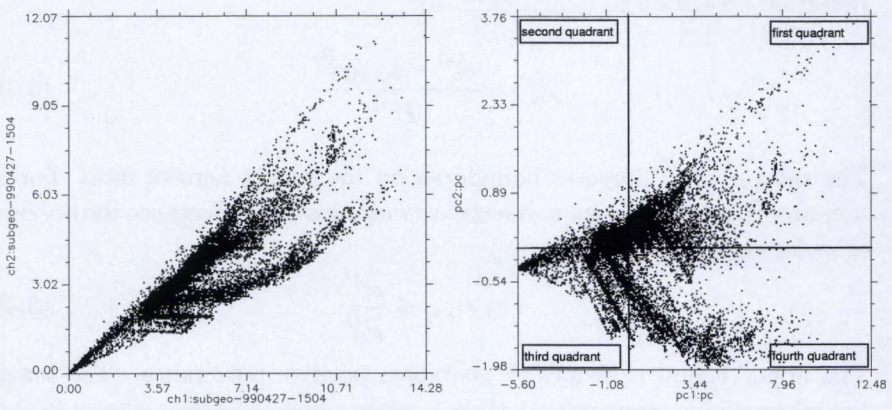

(a) original data (b) transformed data

Fig. 3.4: (a): the scatter plot of corrected reflectance at AVHRR (image subgeo-990427-1504) visible (ch1) and NIR (ch2) channels (%). (b): the PCT of the two AVHRR bands (pc).

as (Emery and Thomson 2001)[80]:

$$\tan 2\theta_{pc1} = \frac{2C_{sl}}{C_{ss} - C_{ll}} \tag{3.5}$$

Where: C_{ss}, C_{ll}, and $C_{s,l}$ are the elements of the covariance matrix of $(\rho_c^{(s)}, \rho_c^{(l)})$. The data points in the new axes of the transform can be described as follows. The reflectance values of thick aerosol over clear or turbid water pixels are expected to be larger than the mean-reflectance. Thus the aerosol dominant pixels and those associated with turbid water signals are situated in the first quadrant of the new axes (see figure 3.4(b)). The reflectance of clear water pixels with moderate aerosol load is larger than the mean NIR-reflectance and less than the mean red-reflectance (second quadrant). The expression red- or NIR- reflectance refers to the reflectance at the red or the NIR AVHRR band. Clear water pixels with clear atmospheric path will have reflectance values less than the mean reflectance at both red and NIR AVHRR bands (third quadrant). The turbid water pixels with relatively clear atmosphere will have negative slope (of the regression line) and reflectance values larger than the mean red-reflectance and smaller than the mean NIR-reflectance (fourth quadrant). Each cluster of pixels can thus be isolated using its signs on the new axes (PCT). However our interest is in the aerosol dominant pixels that are at the first quadrant. The results of this classification are illustrated in figures (3.5(a) and 3.5(b)). As we can see the proposed classification technique isolated the pixels with high reflectance values at both the red and the NIR bands (compare figure 3.3 to figure 3.5(a)). However most of the coastal waters are presented in this cluster (figure 3.5(a)). This cluster is, therefore, further treated to separate the turbid water pixels. Following the same idea, a second PCT can be applied on this class in figures (3.5(a) and 3.5(b)). Again, the aerosol dominant pixels are situated at the first quadrant of the second PCT. The results of the second classification are shown in figures (3.5(c) and 3.5(d)). Figure (3.5) shows that the second PCT-classification has improved the isolation of the aerosol dominant pixels (figure 3.5(c)). Let us note that the remaining pixels (figure 3.5(d)) are highly correlated.

From equation (3.5) the slope of the first principal axis (w.r.t.h.) is an indicator of the correlation between the data sets. The new axis (PC1) is rotated as such to reduce this correlation to its minimum. This will facilitate the separation between physically uncorrelated signals (aerosol and water). The remaining pixels after two successive PCT-classifications are mainly

dominated by one signal. Thus the angle of the first component (θ_{pc1}) is expected to increase in each step approaching 45°. This may explain why the value of the aerosol ratio was set to unity. Let us note that the angle of the second PCT (PC1) physically can not reach the value of 45°. This is due to the fact that the reflectance of the non-absorbing aerosol at NIR is less than that at the red band (consult section 2.6.4). Moreover the reflectance at the NIR is mainly from the aerosol scattering. On the other hand the reflectance at the red band is the sum of water and aerosol signals. In other words the reflectance value at the red is always larger than that at the NIR. Unless the PCT allocates few anomalous pixels that are physically and spatially unrelated. These pixels might have the same values of reflectances at both AVHRR bands, however they are not spectrally-pure pixels. Thus only two

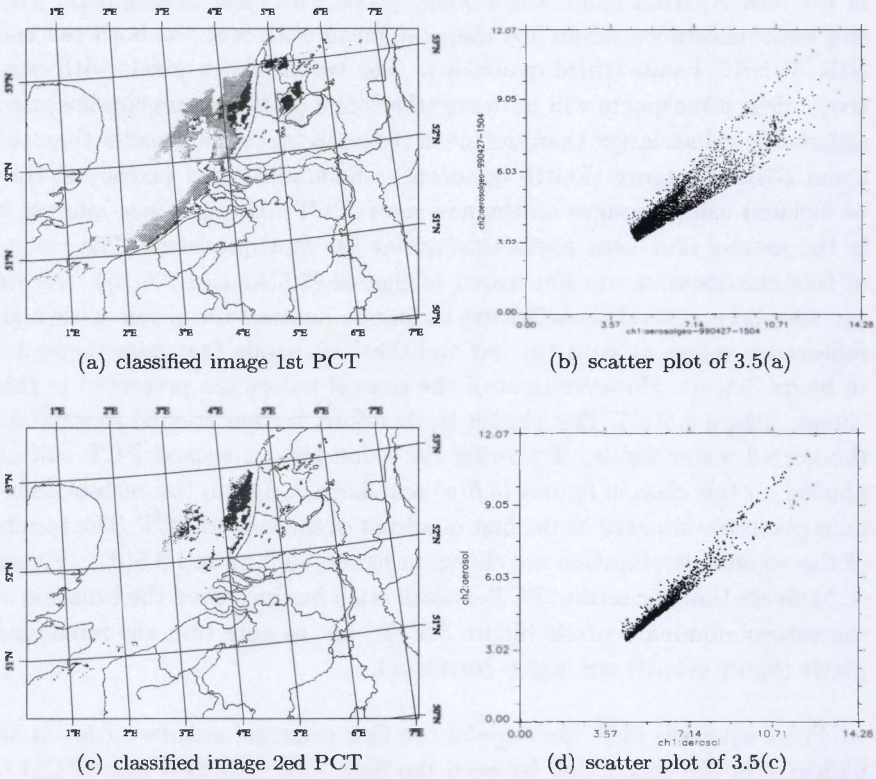

(a) classified image 1st PCT

(b) scatter plot of 3.5(a)

(c) classified image 2ed PCT

(d) scatter plot of 3.5(c)

Fig. 3.5: (a): the results of the classification after the first PCT. (b): the pixels at the first quadrant of figure (3.4(b)). (c),(d): the remaining aerosol dominant pixels after the second PCT classification.

PCT-based classifications are needed to extract the aerosol dominant pixels. The first is to isolate the regions with high reflectance at both AVHRR bands (red and NIR). The second is to uncouple the signals in this mixed class into coastal waters and aerosol dominant pixels. Table (3.1) summarizes the results of each transform associated with classification. The angle of PC1 in the first transform is 37.273°. This was improved in the second PCT to 43°. The value of $\varepsilon_{(1,2)}$ can be estimated from the slope of the regression line between $\rho_c^{(1)}$ and $\rho_c^{(2)}$ of these pixels (equation 3.5). This regression line was found to have an angle of 43° (w.r.t.h.) i.e. $\varepsilon_{(1,2)} = \cot(43°) = 1.074$. This value was assumed spatially homogeneous over the image.

The results were validated with in-situ measurements near the southern bight of the North Sea (table 3.2). The hydro-optical model (equation 2.39) was used at each station to reproduce the expected water leaving reflectance. The inputs were the measured concentrations of suspended particulate matter (SPM) and chlorophyll-a (table 3.2) and specific inherent optical properties of the Belgian coastal waters (measured and supplied by IVM[11]). The relative errors ϵ of a retrieved quantity ρ_R were calculated from the modelled value ρ_M as:

$$\epsilon(\rho_R) = \frac{\rho_R - \rho_M}{\rho_M} \times 100 \tag{3.6}$$

The concentrations of suspended particulate matters were computed by inverting the hydro-optical model (equation 2.39) with a constant concentration of chlorophyll-a (averaged from table 3.2). The presence of dissolved organic matter (DOM) will complicate the optical response of the water column. However, no measurements were available about this quantity. A simplified situation will be considered throughout this exercise. This by assuming that the water is free of DOM.

The retrieved water leaving reflectances are within 45% relative error (table 3.2). However the smallest relative-errors were at sites 250, 330 and 215. The last two sites have the closest sampling time to image acquisition.

Steps	Min	Max	Mean	Stdv	Corr	θ_{pc1}
figure (3.3)	0.004	12.07	3.07	1.142	83.4	30.07
figure (3.5(a))	3.086	12.07	4.291	1.083	93.7	37.273
figure (3.5(c))	3.437	12.07	4.8	1.262	98.1	43

Table 3.1: The statistical parameters for populations of pixels presented in figures (3.3 and 3.5). Stdv and corr are the standard deviation and the correlation coefficient resp.

Weak correlation coefficients were found between the aerosol reflectances and SPM (18%) and water leaving reflectances (16%). This suggests that the errors (table 3.2) might be due to measurement fluctuations. These fluctuations result from the temporal/spatial variations between ship measurements and AVHRR image. This is especially so in the North Sea where the tidal currents determine the near-surface concentrations of suspended matter (Eisma and Kalf 1979)[18]. The weak residual correlation between physically unrelated quantities can be attributed to the following:

- An inherent limitation of the classification procedure. This is the cluster of pixels centered at the mean reflectances. At this cluster, it is difficult to separate the aerosol from water reflectances. Instead the algorithm truncates the data set to larger or smaller than the mean. This truncation is obvious figures (3.5(b) and 3.5(d)).
- The assumption of zero water leaving reflectance at the NIR channel.
- The spatial-homogeneity assumption of the aerosol ratio.
- Generally the concentrations of SPM decrease with distance from the coast. This trend (i.e. decreasing concentration with offshore distance) can also occur for the concentration of aerosol. This common gradient of aerosol and SPM concentrations might creates a kind of correlation between the physically unrelated quantities (i.e. aerosol and SPM).

3.3.3 Turbid water

Althuis and Shimwell (1995)[79] observed that the NIR band of AVHRR is more appropriate for the estimation of suspended particulate matter. This

Sta.	time	SPM	Chl-a	$\rho_w^{(s)}$		SPM_R	relative error%	
	UTC	$g.m^{-3}$	$mg.m^{-3}$	M%	R%	$g.m^{-3}$	ρ_w	SPM
150	0:11	18.4	30.1	1.627	2.33	23.32	43.4	26.8
250	4:00	28.2	42.6	2.01	2.50	25.65	24.5	-9
435	6:13	8.7	12.7	1.09	0.73	5.72	-33.4	-34.1
421	8:42	6.0	11.2	0.81	1.10	9.17	35.8	52.9
330	11:41	12.8	13.6	1.49	1.27	10.87	-14.6	-15.1
215	17:08	11.2	20.2	1.217	0.9	7.32	-25.7	-34.6
ZG03	19:05	25.2	12.5	2.53	1.45	12.73	-42.6	-49.5
ZG01	20:01	16.0	11.5	1.83	1.35	11.72	-26.1	-26.8

Table 3.2: Measured concentrations of SPM and chlorophyll-a and the modelled (M) and retrieved (R) water leaving reflectances.

is because the AVHRR NIR band saturates at higher concentrations of SPM than the visible band. Tolk *et al.* (2000)[84] showed that the NIR band of AVHRR sensor is not affected by bottom reflectance. Han *et al.* (1996)[85] suggested a linear relationship between the reflectance at the NIR and concentration of SPM. To account for the reflectance in channel two, a linear relationship (equations 2.78 and 2.79) between the water leaving reflectance at both AVHRR channels (1,2) can be imposed. Thus the water leaving reflectance is calculated from equation (2.80). This equation is similar to (3.3) with an enhancement factor of:

$$\alpha_{(s,l)}/(\alpha_{(s,l)} - \varepsilon_{(s,l)}) \tag{3.7}$$

Table (3.3) shows that, although the water signals were considered at the NIR, the retrieved quantities (water leaving reflectance and SPM concentrations) are subjected to large errors. The use of equation (2.80), simply, added positive values to the relative errors. Thus the positive relative-errors were increased whereas the negative values were decreased. This is because the water leaving reflectance was enhanced by a constant value (equation 3.7). For the NIR band the results are even worse. While the relative error in SPM retrieved from the red band did not exceed 65%, it reached to 142% when retrieved from the NIR band. The relative errors were reduced for the sites with underestimated water leaving reflectance. However, these sites do not represent turbid water. Thus, in comparison to the clear water approach (equation 2.73) there is no obvious improvement on the red band (table 3.4).

Table (3.4) shows the mean relative error for all eight stations using clear (equation 2.73) and turbid (equation 2.80 with constant $\alpha_{(s,l)}$) water

Sta.	$\rho_w^{(2)}$%		SPM g.m^{-}3		relative error%			
	M	R	band1	band2	$\rho_w^{(1)}$	$\rho_w^{(2)}$	SPM1	SPM2
150	0.056	0.112	25.0	31.1	50.8	97.9	35.8	68.9
250	0.086	0.199	27.5	33.3	30.9	38.9	-2.3	18.266
435	0.027	0.035	6.1	9.6	-30.0	30.0	-30.2	10.6
421	0.019	0.053	9.7	14.6	42.8	183.9	62.1	142.88
330	0.039	0.061	11.5	16.9	-10.2	54.7	-9.8	31.72
215	0.034	0.043	7.8	12.0	-21.9	25.6	-30.8	6.78
ZG03	0.077	0.097	13.5	19.3	-39.7	-9.9	-46.3	-23.6
ZG01	0.0492	0.065	12.4	18.0	-22.0	32.0	-22.2	12.28

Table 3.3: The modelled and retrieved (equation 2.80) water leaving reflectance and the associated SPM concentrations. M and R are for the modelled and retrieved quantity respectively.

quantity	equation (2.73)	equation (2.80)	
	red	red	NIR
WLR	-4.84 ± 33.9	0.06 ± 35.7	56.6 ± 49.7
SPM	-11.15 ± 34.5	-5.46 ± 36.9	33.48 ± 51.3

Table 3.4: The mean values of the relative error ± standard deviation of the water leaving reflectance (WLR) and the concentrations of SPM.

approach. The parameter $\alpha_{(s,l)}$ was approximated for the AVHRR visible and NIR band from equation (2.78). Introducing a constant value of the water ratio will slightly reduce the mean relative-error however the standard deviation is still the same (even slightly increased). On the other hand the relative error in the NIR band is scattered within a large standard deviation. This variance might be attributed to the introduced assumptions on the aerosol and water ratios. The relative errors of $\alpha_{(s,l)}$ and $\varepsilon_{(s,l)}$ were evaluated from the modelled values of $\varepsilon_{(s,l)}$ and $\alpha_{(s,l)}$ (table 3.5). The modelled values of $\varepsilon_{(s,l)}$ and $\alpha_{(s,l)}$ were estimated from the modelled values of water leaving reflectances (using measured concentrations of SPM and Chl-a, table 3.2) and the corrected reflectance of AVHRR red and NIR bands. Table (3.5) shows that the smallest relative error in the aerosol ratio $\varepsilon_{(s,l)}$ was at station 330. In other words, the principal component transform gave a good estimate of $\varepsilon_{(s,l)}$ value at the site with closest sampling time to image acquisition. However the use of equation (2.78) in calculating the water leaving reflectance (equation 2.80) is not accurate for AVHRR spectral bands. This limitation is due to the spectral position of AVHRR red band. The water leaving reflectance at this red band is governed by chlorophyll-a (Chl-a), dissolved organic matter (DOM) and suspended particulate matter (SPM). Thus the total absorption coefficient cannot be estimated accurately from the water absorption coefficient (i.e. $a^{(red)} \neq a_w^{(red)}$). Additional information on the concentrations of Chl-a and DOM are necessary to estimate the

Sta.	modelled		relative error%	
	$\alpha_{(s,l)}$	$\varepsilon_{(s,l)}$	α	ε
150	28.79	1.26	-23.81	-15.07
250	23.29	1.22	-5.8	-11.95
435	40.73	1.03	-46.14	4.77
421	43.61	1.24	-49.7	-13.1
330	37.78	1.07	-41.94	0.55
215	35.26	1.09	-37.79	-1.5
ZG03	32.76	0.9	-33.04	19.79
ZG01	37.26	1	-41.13	7.28

Table 3.5: Modelled values of $\varepsilon_{(s,l)}$ and $\alpha_{(s,l)}$ and their relative errors

ratio $\alpha_{(s,l)}$. The value of $\alpha_{(s,l)}$ is assessed using equation (2.75) for the upper panel of figure (3.6) and $\alpha_{(red,nir)} = \frac{a(nir)}{a(red)}$) for the lower panel. The last approximation was based on equation (2.76) for the water leaving reflectance with flat backscattering coefficient (Gould 1999)[71]. The concentrations were varied from 0 to 20 mg.m^{-3} and from 1 to 80 g.m^{-3} for Chl-a and SPM respectively. The DOM absorption coefficient was given three values of (0, 0.5 and 1 m^{-1}) at 0.4 μ m. The DOM absorption extrapolated to the AVHRR red and NIR bands using equation (2.33).

Figure (3.6) shows that the presence of Chl-a and DOM dramatically change the value of $\alpha_{(s,l)}$. This is especially for low concentration of SPM. This also can be observed in table (3.5). The largest relative-errors in the assumed value of $\alpha_{(s,l)}$ were obtained at stations 421 and 435. These two sites have the lowest values of the measured SPM concentrations. Figure (3.6) clearly illustrates that $\alpha_{(s,l)}$ is not constant and has to be related to the actual turbidity of the water surface layer. This is to reflect the

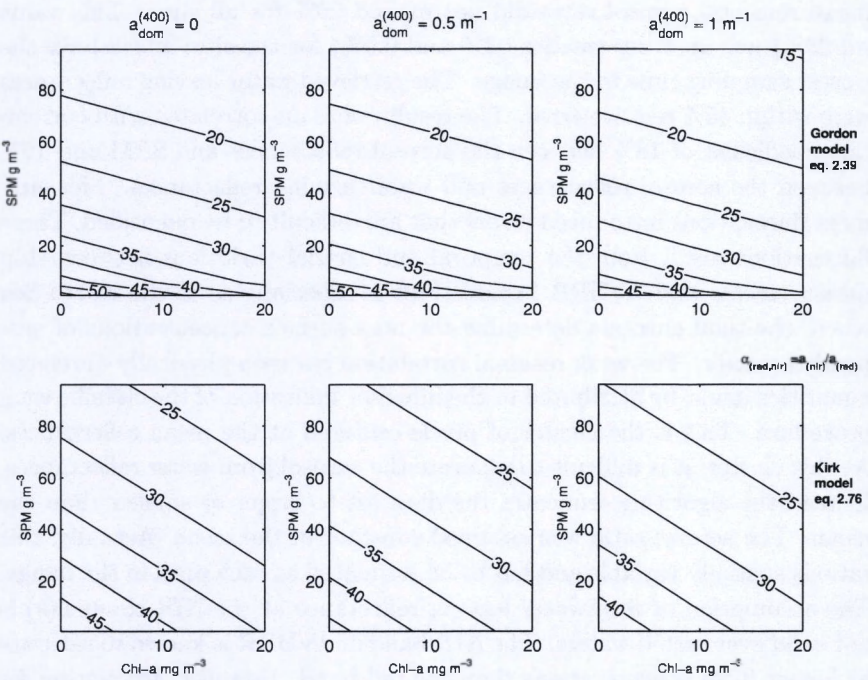

Fig. 3.6: The variation of the water ratio for AVHRR spectral bands plotted as a function of Chl-a, DOM and SPM.

underlying physical and optical processes in the water column at the red band of AVHRR.

3.4 Conclusion and remarks

The proposed atmospheric correction algorithm utilized the clear water approach. In other words, the total recorded reflectance at AVHRR NIR band is mainly due to aerosol scattering. However instead of allocating a clear water region at the red band, the algorithm allocates an aerosol dominant region at the red and the NIR AVHRR bands. This implies that the aerosol reflectances is always present in the scene of an AVHRR image. The aerosol dominant pixels were classified using two consecutive principle component transform. The aerosol ratio was then estimated over these pixels. The estimated aerosol ratio from these pixels was within acceptable accuracy for the sites that were the closest, in sampling time, to the image acquisition. The relative difference between the retrieved and modelled (based on measurements) aerosol ratio did not exceed 20% for all sites. This value (of 20%) was an order smaller (-1.5 and 0.5%) for the sites which have the closest sampling time to the image. The retrieved water leaving reflectances were within 45% relative error. The results were un-correlated with correlation coefficient of 18% between the aerosol reflectances and SPM and 16% between the aerosol reflectances and water leaving reflectances. Measurement fluctuations introduced errors that are difficult to be quantified. These fluctuations result from the temporal and spatial variations between ship measurements and AVHRR image. This is especially so in the North Sea where the tidal currents determine the near-surface concentrations of suspended matter. The weak residual correlation between physically unrelated quantities might be attributed to the inherent limitation of the classification procedure. This is the cluster of pixels centered at the mean reflectances. At this cluster, it is difficult to separate the aerosol from water reflectances. Instead the algorithm truncates the data set to larger or smaller than the mean. The aerosol ratio was assumed constant of the scene. Actually, this ratio is spatially variable and has to be estimated at each pixel in the image. The assumption of zero water leaving reflectance at the NIR channel(s) is not valid over turbid waters. The NIR band of AVHRR is known to saturate at higher SPM concentrations than the red band. However, accounting for the water signal at the NIR by assuming a constant value of $\alpha_{(s,l)}$, had no advantages over the clear water approach (zero water leaving reflectance at

the NIR). The water leaving reflectances at AVHRR NIR band were noisy and not reliable for low concentration of suspended sediments (i.e. relatively clear waters). This might either be due to the weak water leaving signal at the NIR band of AVHRR or to the assumption of constant water ratio. The water ratio for AVHRR red and NIR bands has to be linked to the underlying physical and optical processes in the water. It is advisable to atmospherically correct clear and turbid waters separately. For validation purposes, it is essential to perform simultaneous in-situ measurement with ± 1 hour of image acquisition.

Chapter 4

Transformation technique to atmospherically correct SeaWiFS images

Abstract

Recently the assumption of known or negligible water leaving reflectance and the model-produced empirical relationships were replaced with relationships that are only dependent on the absorption property of seawater (Carder *et al.*, 1999[66], Ruddick *et al.*, 2000[68], and Hu *et al.*, 2000[69]). The aerosol ratio was estimated over turbid waters following a general approach. First classify the image into clear and turbid waters regions. The aerosol ratio is then estimated over the clear water region. The value of this ratio can either be spatially extrapolated to turbid water pixels (Hu *et al.*, 2000) [69] or assumed constant (Ruddick *et al.*, 2000)[68]. The clear water region can be classified either through a defined threshold (Bricaud and Morel 1987)[76], visual inspection approach (Ruddick *et al.*, 2000)[68], or failure of the atmospheric correction algorithm of clear waters (Hu *et al.*, 2000)[69]. In the following chapter, we will use the principal component transform technique to classify the clear water pixels from a SeaWiFs image. The algorithm retrieved an accurate value of the aerosol ratio that was reasonable for all sampling stations. The relative errors in the estimated aerosol ratio (at the NIR) did not exceed 2%. The smallest value (i.e. of the relative error) was at the station which had the closest sampling time to

image acquisition. Moreover, low correlations (-2.15%) were found between the aerosol and the water leaving reflectance at 0.765 μm. The correlation was slightly increased to -4.14% for aerosol and SPM. However a sensitivity study (developed in section 4.4.1) shows that the accuracy of the retrieved water leaving reflectance is mainly affected by the spectral extrapolation of the aerosol ratio. This chapter is complementary to chapter (3).

4.1 Introduction

4.1.1 Standard algorithm for the atmospheric correction of SeaWiFS images: clear waters

The second generation of ocean color sensors (SeaWiFS, MERIS) enabled the development of more complicated algorithms (Gordon and Wang 1994)[61]. This is because the spectral position of the NIR channels is more appropriate to impose reasonable assumptions on the water leaving reflectances. Most of these sensors have two (or more) NIR bands at which the water signals can be assumed known (or zero). This yields the aerosol reflectance at both channels and hence the Angstrom exponent can be calculated (equation 2.64). In turn, the Angstrom exponent allows the extrapolation of the aerosol signal at NIR to shorter wavelengths. In principle the aerosol signal can be simulated for each identified aerosol-model (geometry, type and relative humidity). Then each pixel is compared to the model-produced-aerosol reflectance to define the associated aerosol model. This will produce the aerosol types and optical thicknesses for each pixel in the image. The algorithm of Gordon and Wang (1994)[61] was based on the aerosol ratio as the key parameter to allocate the appropriate aerosol model. The zero water-signal at NIR channels renders the aerosol terms (multiple scattering and coupling term). The aerosol ratios (in the single and multiple scattering regimes) were linked with a relationship for each aerosol model (equation 2.69). Then the aerosol ratio can be calculated and averaged over the different aerosol models. Two aerosol-candidates that bound this averaged-aerosol ratio are allocated. The weighted-sum of these models is the sought aerosol model. The position of the averaged-aerosol ratio relative to the bracketing models is proportional to these weights. The strength of this method is that it combines the solution of the radiative transfer equation (RTE) in the atmosphere, with a spectral fitting that retrieves the aerosol optical properties (i.e. the necessary missing- inputs to the RTE). The overlap of the oxygen absorption band at 0.759 μm was corrected for following

Ding and Gordon (1995)[86]. The Gordon and Wang (1994) approach is illustrated in figure (4.1).

4.1.2 Extending the atmospheric correction algorithms of SeaWiFS for turbid waters

The assumption of zero water leaving reflectance at NIR channels was successful for case-I waters. However, any water-leaving signal at these NIR channels (e.g. water optically governed by suspended sediment) will result in underestimation of the whole water leaving-reflectance spectrum. The inadequacy of the clear water approach in turbid-water regions appeals for a different treatment of the water leaving reflectance at the NIR region of the spectrum. A possible approach is by establishing relationships between the water signals at the NIR wavelengths. Smith and Wilson (1981)[87] originally proposed empirical relationships to estimate the reflectance at NIR of the CZCS channels from shorter-wavelengths. The empirical constants were determined from in-situ measurements, therefore they were adjustable based on the water type under study (Muller 1984[88], Viollier and Sturm 1984[89]). Thus, the empirical constants (which are in reality variables) have to be reassessed for each sensor's overpass. Austin and Petzold (1981)[90] performed a direct study of the relationships between the water leaving reflectances from measurements of up-welling sub-surface reflectances. The relationships among the water leaving signals were successfully applied to determine the pigment concentrations (Bricaud and Morel 1987[76], Andre and Morel 1991[74]). They were regionally employed to develop an appropriate algorithm for case-II waters (Gould and Arnone 1994)[91]. Lavender *et al.* (1997)[92] and their extended work by Moore *et al.* (1999)[93] evaluated the ratio of the water leaving reflectance at two NIR channels (water-ratio) as a function of suspended sediment concentrations. The algorithm of Moore *et al.* (1999)[93] assumed two types of waters each of which is optically governed by one constituent (i.e. chlorophyll-a and suspended sediment). The first category is obviously case-I water, therefore the clear water approach (Antoine and Morel 1998)[94] is used. For the second water type (i.e. case-II water) the water-ratio is calculated for a variety of suspended sediment concentrations at selected NIR channels. The algorithm is initialized by fixing the water-ratio (at concentration of 50 mg/l) and the Angstrom exponents (equal to zero). Then an iterative procedure is used to solve the reflectance equation for concentrations and the Angstrom exponent (see figure 4.2). Figure (4.2) can be linked to figure (3.2) to solve for the atmosphere-ocean

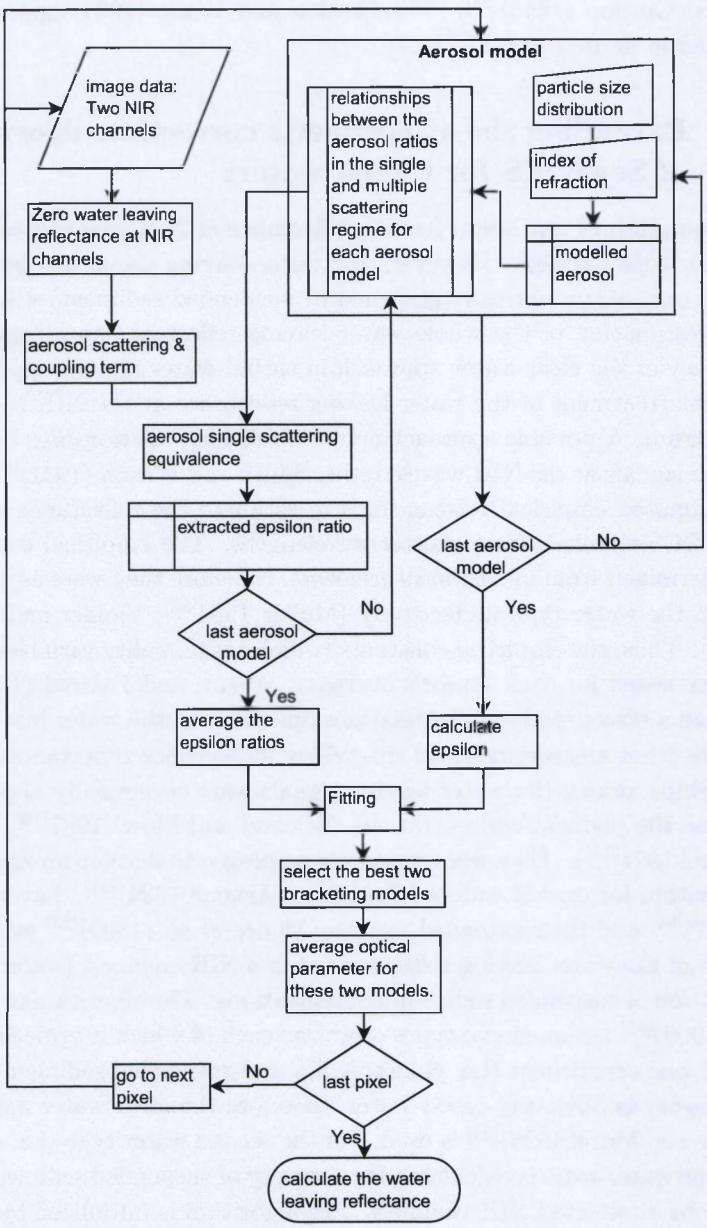

Fig. 4.1: The atmospheric correction algorithm of Gordon and Wang (1994).

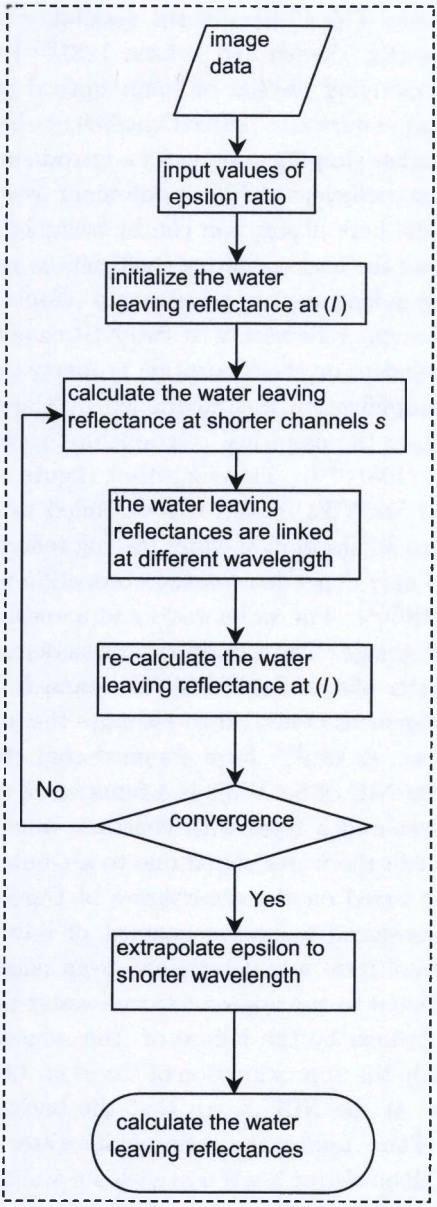

Fig. 4.2: Atmospheric correction algorithm which uses relationships between the water leaving reflectance at different wavelength.

system simultaneously. This illustrates the possibility of replacing the empirical relationships (e.g. Smith and Wilson 1981[87]) with a relationship that reflects the underlying physics of water optical properties (equation 2.75). Therefore, no empirically derived coefficients have to be evaluated for each image. Further simplification can be introduced by assuming that the water absorption coefficient at NIR is dominant over other constituents-absorption. Thus the bulk absorption can be assumed equal to the water absorption. Moreover the backscattering coefficient is spectrally flat at NIR and can be assumed independent of wavelengths (Gould *et al.*, 1999)[71]. So the ratio of water-leaving reflectances at two NIR channels can be approximated as being dependent on the absorption property of seawater (equation 2.78) only. This simplification was mentioned by Carder *et al.* (1999)[67] for MODIS to replace the empirical relationships previously proposed by Smith and Wilson (1981)[87]. The algorithm (figure 4.1) of Gordon and Wang (1994)[61] for SeaWiFs images was extended to turbid water. This by replacing the zero assumption of water leaving reflectance at NIR with a relationship that is only dependent on the absorption property of seawater (Ruddick *et al.*, 2000)[68]. The water ratio and aerosol ratio were assumed constant over a sub-image. The aerosol ratio was determined by visual inspection of the scatter plot of SeaWiFS NIR channels. Thus, for each sub scene an expert judgement is needed to estimate the aerosol ratio. On the other hand Hu *et al.* (2000)[69] have assumed that the water leaving reflectances at the two NIR of SeaWiFs is a function of the associated water absorption coefficient and a term with constant value. This term represents the increment in the water signal due to air-bubbles and SPM. This approximation was based on the observation of Carder *et al.* (1999)[66]. The constant was assumed to be independent of wavelength but variable in space. The aerosol ratio was determined from neighboring clear water pixels and extrapolated to the adjacent turbid water pixels. The region of turbid water was defined by the failure of the atmospheric correction of clear water. Actually the approximation of Hu *et al.* (2000)[69] of the water leaving reflectances at the NIR means that the backscattering coefficient is spectrally flat. Thus, taking the ratio of the water leaving reflectances at these two NIR channels (of SeaWiFs) yields a similar approximation to Ruddick *et al.* (2000)[68]. Besides, any error in the estimated aerosol ratio (over clear waters) will propagate (and possibly magnify) to turbid-water pixels through the spatial extrapolation procedure. This might impose a kind of correlation between the atmospheric path with its lower boundary (i.e. water leaving reflectance). In the following chapter, we propose a tech-

nique to classify the clear water pixels in the SeaWiFs images. The value of the aerosol ratio over these pixels is then estimated from regression. A sensitivity study (developed in section 4.4.1) shows that the accuracy of the retrieved water leaving reflectance is mainly affected by the spectral extrapolation of the aerosol ratio.

4.2 Method

SeaWiFS sensor was especially designed for water studies (ocean color). It has two NIR bands (centered at 0.765 μm and 0.865 μm with 0.04μm spectral interval) for the purpose of atmospheric correction. The position of SeaWiFS NIR bands facilitates the assumption of optically clear water. This is due to the sea-water molecules which absorb most of the backscattered energy at the NIR. The water column can thus be assumed to be optically governed by the inherent optical properties of SPM and sea-water molecules. Therefore the water ratio $\alpha_{(s,l)}$ at these two NIR bands can be estimated from equation (2.78). On the other hand, the values of the aerosol ratio can be inferred from the clear water region. This is because the SeaWiFS NIR bands are spectrally close and highly correlated. Therefore, the corrected reflectances (equation 2.72) of SeaWiFS NIR bands will have two major classes. The first has high reflectance which arises from turbid water, turbid atmosphere or the sum of both high-signals. The second class has low reflectance which is the sum of clear water and relatively clear atmosphere signals. However the signal of clear water observed by optically-clear bands (i.e. NIR) is negligible. Thus, the signals over clear water pixels will give a close approximation to the aerosol scattering. These pixels are situated at the third quadrant of the PCT axes. In other words, these pixels have small reflectance at both bands which is smaller than the mean reflectance. These pixels can be classified from the transformed images. The aerosol ratio $\varepsilon_{(s,l)}$ can then be estimated over the clear water pixels from regression. This approach is applied on a SeaWiFS image (figure 4.3), acquired at the same time as the previous AVHRR image (figure 3.3).

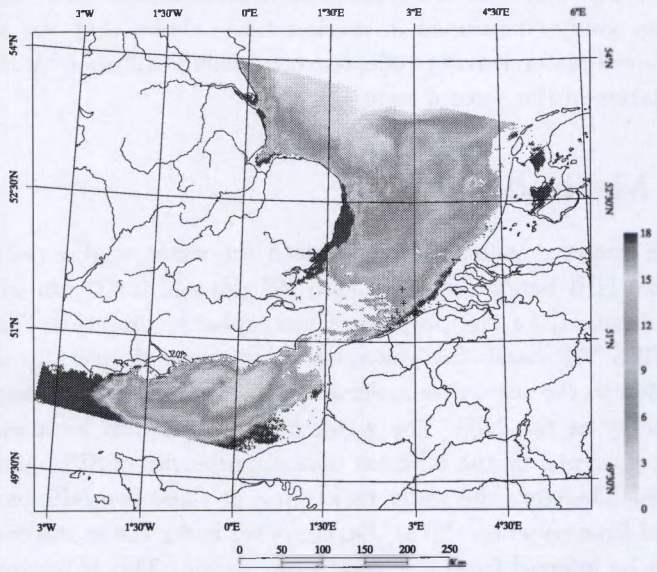

Fig. 4.3: The first NIR band (0.765 μm) of SeaWiFS image at the tope of atmosphere acquired in 27 April 1999 at 12:38 UTC. Sampling sites are indicated by '+'.

4.3 Results and discussion

4.3.1 PCT transformation

The result of the PCT is illustrated in figure (4.4) and its statistical parameters are shown in table (4.1). Table (4.1) shows that the two NIR bands are highly correlated and the PCT has a small influence on the correlation coefficient. The benefit of the transform can be evaluated by calculating

step	min %	max%	mean%	Stdv%	corr%	θ_{pc1} degrees
image, band7	4.42	18.25	7.01	1.67		
image, band8	3.84	17.35	6.47	1.55	99.02	42.696
PCT, band7	4.42	7.22	5.85	0.57		
PCT, band8	3.84	6.47	5.26	0.55	99.13	43.619

Table 4.1: The statistical parameters for the populations of pixels presented in figures (4.4). Stdv and corr are the standard deviation and the correlation coefficient respectively.

the value of the aerosol ratio $\varepsilon_{(s,l)}$ at each classification step (table 4.1). In a highly correlated data-set the angle of PC1 (w.r.t.h.) is, approximately, equal to that of the regression line (equation 3.2). The value of $\varepsilon_{(s,l)}$ can therefore be calculated from the angles of PCT presented in table (4.1). These values are 1.084 for the original data set and 1.0494 after the PCT. The transform has reduced the estimated value of $\varepsilon_{(s,l)}$ about 3.3%. This difference (3.3%) will be increased (using equation 2.66) to 14.67% at the blue band 0.443μm. This error will underestimate the water signal at 0.443 μm about 1% for corrected reflectance >0.05% at 0.865μm. This error (1%) is an order of magnitude larger than the value of acceptable error (0.1-0.5%) at the blue (Gordon 1997)[42]. Let us note that a second classification is not necessary since it will classify the cluster of pixels (resulting from the first classification step) that, most probably, belongs to the same class. Table (4.2) shows the retrieved water leaving reflectance using the estimated value of the aerosol ratio $\varepsilon_{(s,l)} = 1.0494$. The water ratio for SeaWiFS NIR bands is the inverse of the corresponding water absorption coefficients

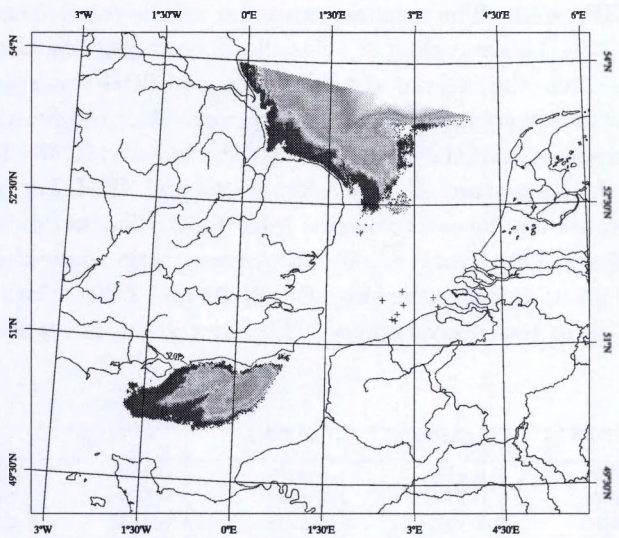

Fig. 4.4: The clear water pixels resultant from the PCT.

ratio $\alpha_{(s,l)} = 1.72$ (Ruddick *et al.*, 2000)[68]. The concentration of SPM were calculated from the first NIR band (0.765 μm). Let us note that the variations in SPM concentrations are not reproduced (compare to the in-situ measurements in table 3.2). Actually there is a kind of averaging in the estimated SPM concentrations. This might be due to the large value of water absorption coefficient that suppresses the backscattered signals. Moreover the assumption of constant values of water and atmospheric parameters $\alpha_{(s,l)}$ and $\varepsilon_{(s,l)}$ might reduced the spatial variations of the water signal. The second assumption (constant $\varepsilon_{0.765,0.865}$) will introduce errors to the water leaving reflectance at shorter wavelengths. These errors can be calculated from the modelled and retrieved water leaving reflectances (table 4.3). The water leaving reflectance was modelled using equation (2.39) and the measured concentrations (table 3.2) and the SIOP (IVM[11]). We can observe (from table 4.3) that the assumed value of $\alpha_{(s,l)} = 1.72$ was larger than the modelled values by approximately 7-9%. The constant value (1.72) is a close estimate of the water reflectance ratio for the SeaWiFs NIR bands. On the other hand the relative error between retrieved and modelled aerosol ratio (at the NIR) did not exceed 2% (table 4.3). The aerosol ratio was calculated from the modelled water leaving reflectance (using the model 2.39 and the in-situ measurement of table 3.2) and the corrected reflectance of SeaWiFS NIR bands. The smallest value (i.e. of the relative error) was at the station 330. This sampling site has the closest sampling time to image acquisition. Thus the estimated value of $\varepsilon_{(s,l)}$=1.0494 was reasonable for all stations. This was confirmed by the low correlation coefficient of -2.15% between the aerosol and the water leaving reflectance at 0.765. The correlation was slightly increased to -4.14% for aerosol and SPM. Let us note that two main groups can be categorized in table (4.3). The first group includes the sites 435 and 330. Over these sites the aerosol ratio was underestimated. The second group includes the sites 250, ZG03 and ZG01. Over this group the aerosol ratio was overestimated. The first group is representative to

sta.	$\rho_c^{(0.765)}$ %	$\rho_c^{(0.865)}$ %	$\rho_{wM}^{(0.765)}$%	$\rho_{wR}^{(0.765)}$%	SPM g.m^{-3}
250	8.919	8.422	0.4844	0.4387	23.6
435	7.1841	6.7736	0.1534	0.3808	20.4
330	7.6363	7.1922	0.2248	0.4256	22.87
ZG03	8.0647	7.6601	0.435	0.2761	14.8
ZG01	7.708	7.2909	0.2796	0.3457	18.53

Table 4.2: Corrected reflectance ρ_c, modelled ρ_{wM}, retrieved ρ_{wR}water leaving reflectances and the estimated SPM concentrations from 0.765μm.

clear water region whereas the second group is for turbid waters (see table 3.2). Therefor the water leaving reflectance will be underestimated for turbid water and overestimated for clear water sites. An important observation is that the underestimation of the water leaving spectrum begins at SPM concentrations 15 $g.m^{-3}$.

sta.	modelled parameters		relative error%	
	$\varepsilon_{(s,l)}$	$\alpha_{(s,l)}$	$\varepsilon_{(s,l)}$	$\alpha_{(s,l)}$
250	1.0393	1.58	0.97	8.7
435	1.0529	1.6	-0.33	7.51
330	1.0511	1.591	-0.16	7.85
Zg03	1.0331	1.58	1.58	8.54
Zg01	1.044	1.59	0.529	8.03

Table 4.3: The modelled aerosol and water ratios, and the associated relative errors.

4.3.2 Spectral extrapolation of the aerosol ratio

Although the proposed technique accurately retrieved the aerosol ratio at the NIR, the spectral extrapolation of this ratio might be not appropriate. Normally the performance of an atmospheric correction algorithm is assessed at shorter wavelengths. Negative values of water leaving reflectance at the blue channels is an indication of algorithm failure. Let us note that the value of $\varepsilon_{(s,l)}$ was directly extracted from the image hence it is a multiple scattering ratio. The aerosol ratio (at bands i and l) in the multiple scattering regime $\varepsilon_{(i,l)}$ can be linearly related to that of the single scattering state $\varepsilon^{s}_{(i,l)}$ (Gordon and Castano 1987)[49] see equation (2.70).

$$\varepsilon_{(i,l)} = \kappa_{(i)}\varepsilon^{s}_{(i,l)} \tag{4.1}$$

Where $\kappa_{(i)}$ is the second term on the right hand side of equation (2.70). This (equation 4.1) can be substituted in the extrapolation formula of Gordon and Wang (1994)[61], (equation 2.66):

$$\varepsilon_{(i,l)} = \kappa_{(i)} \left(\frac{\varepsilon_{(s,l)}}{\kappa_{(s)}} \right)^{\delta_i} \tag{4.2}$$

Suppose that the coefficient $\kappa_{(\lambda)}$ at the NIR is spectrally flat (i.e. $\kappa_{(i)} = \kappa_{(s)}$), then equation (4.2) becomes:

$$\varepsilon_{(i,l)} = \kappa^{(1-\delta_i)}\varepsilon^{\delta_i}_{(s,l)} \tag{4.3}$$

Equation(4.3) allows to spectrally extrapolate the multiple scattering aerosol ratio ($\varepsilon_{(s,l)}$=1.0494) to shorter wavelengths. Another approach is to include the coupling-term in the extrapolation-exponent. The new exponent values are calculated from the modelled values of the aerosol ratios as:

$$\delta_i^* = \log \frac{\varepsilon_{(i,l)}}{\varepsilon_{(s,l)}} \tag{4.4}$$

First, the measured concentrations of SPM and Chl-a (table 3.2) were used to simulate the spectrum of the water leaving reflectance at each station (using equation 2.39). Note that the missing stations (from table 3.2) were under cloud covers. The parameter κ (in equation 4.3) was estimated, at the NIR, from the modelled water leaving reflectance and the corrected reflectance recorded by the sensor. In the same manner, the exponent δ_i^* was calculated from the modelled water leaving reflectance and the corrected reflectance. Second, for the same retrieved-value of the aerosol ratio (i.e. $\varepsilon_{(0.765,0.865)}$=1.0494) three different water leaving spectra were obtained. These spectra were estimated using three atmospheric correction algorithms. Each scheme spectrally extrapolates the aerosol reflectance in a different manner, namely equation (4.3), equation (2.66) in the multiple scattering regime (i.e. using 4.4) and equation (2.66) in the single scattering regime.

The first scheme (Gordon and Castno 1987[49] coupled with Gordon and Wang 1994[61]) assumes a linear relationship between the aerosol ratio at the single scattering regime and that of multiple scattering. The parameter κ was calculated from the modelled values of water leaving reflectance and measured values of total reflectance at each site. The value ($\varepsilon_{(s,l)}$=1.0494) was then spectrally extrapolated to shorter wavelengths using equation (4.3). The retrieved spectra of water leaving reflectance are illustrated in figure (4.5). The numbers at the panels in figure (4.5) are the root-mean-square between both spectra. This was used as a measure of the total fit of the retrieved spectra ($\rho_{wR}^{(i)}$) to the modelled spectra ($\rho_{wM}^{(i)}$). There is a good agreement between the modelled and the measured values of water leaving reflectance. The root-mean-square between the two spectra did not exceed 0.7% of reflectance. The second scheme uses modelled values of the aerosol ratio in equation (4.4). The aerosol ratio is then extrapolated using equation (2.66). In other words the aerosol ratio in the multiple scattering regime is spectrally extrapolated in a similar manner to the that of the single scattering regime with different exponent, however. Figure (4.6) illustrates the retrieved water signals using the estimated value of the aerosol ratio 1.0494 with the appropriate values of the extrapolation-

exponent. Three important observations can be drawn from figure (4.6). First the overall fit is far improved over the approach which uses the parameter κ. Second, the chlorophyll absorption feature at 0.443μm is reproduced for all spectra. Third, there is no overcorrection of the aerosol signals at the short wavelengths. This might lead to the conclusion that the correction scheme is more sensitive to the spectral extrapolation of the aerosol ratio than its value at the NIR.

This outcome can be reinforced (figure 4.7) by using the third scheme (Gordon and Wang 1994)[61] which neglects the coupled term in the spec-

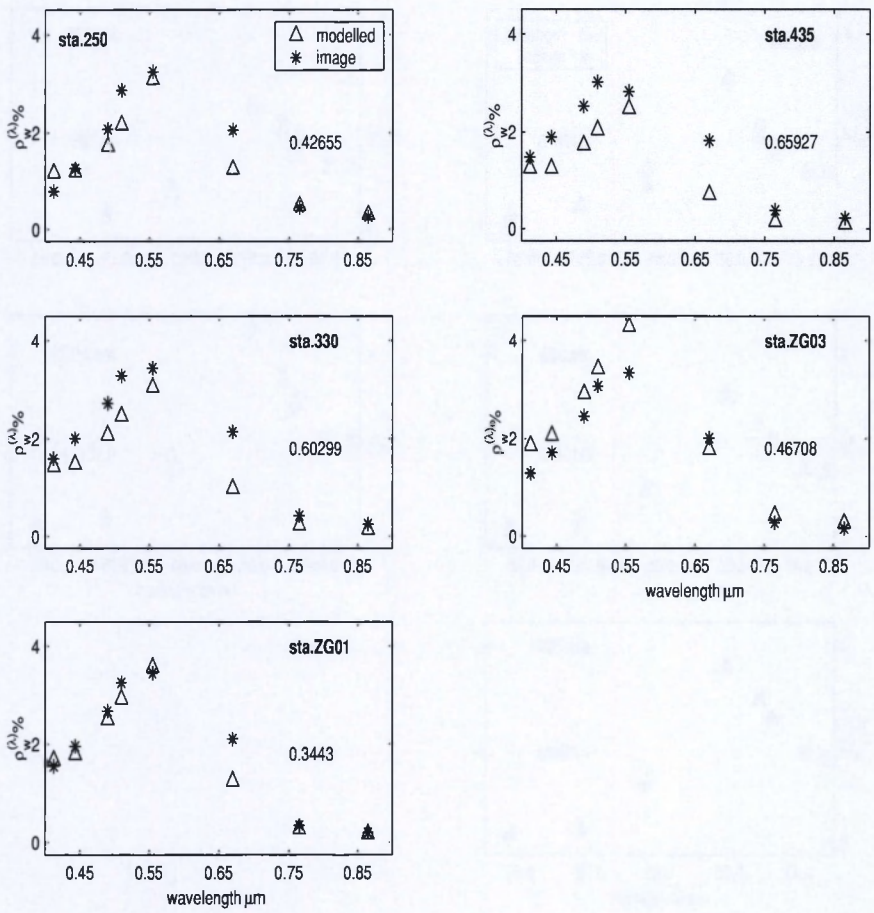

Fig. 4.5: The spectra of the modelled and retrieved (with modelled value of κ) water leaving reflectance at the sampling stations.

tral extrapolation. In other word using equations (equation 2.66 and 2.67) to spectrally extrapolate the multiple scattering aerosol ratio. Figure(4.7) shows an overestimation of the aerosol reflectance at the blue bands. In other words the atmospheric correction algorithm will fail in retrieving the water leaving reflectance from the total recorded reflectance at the blue bands. This is due to neglecting the coupled term in the extrapolation formula of the aerosol ratio. We can conclude that the failure of an atmospheric correction is due to the procedure being used to spectrally extrapolate the aerosol reflectance form the NIR to the blue wavelengths.

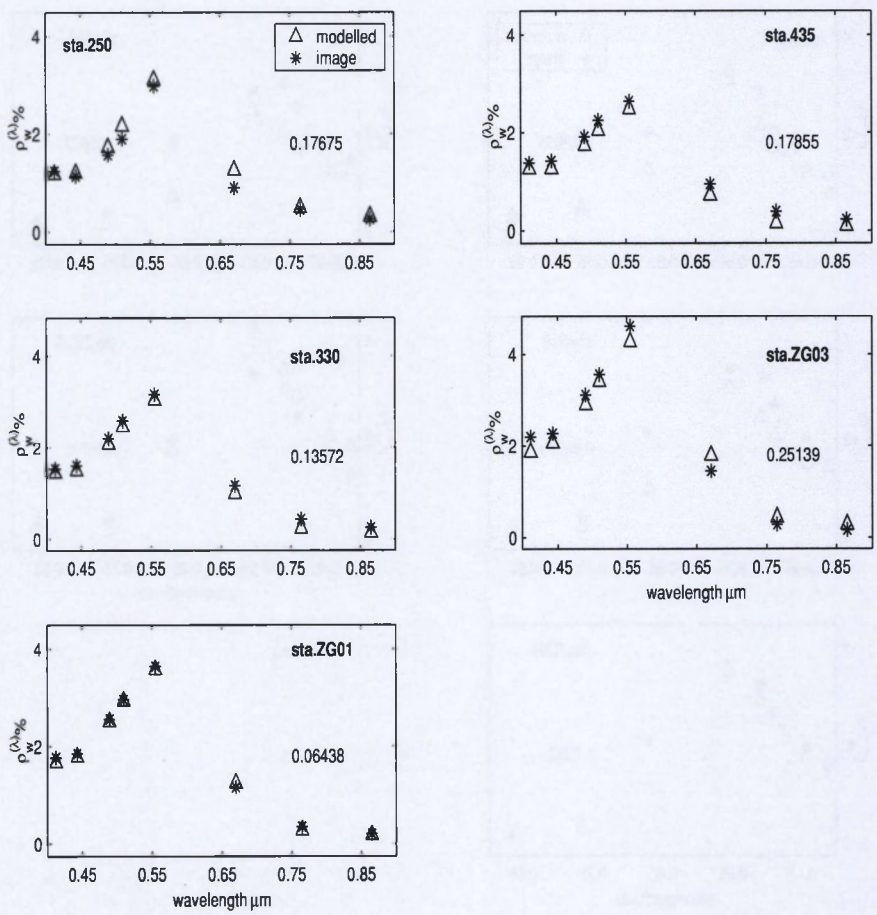

Fig. 4.6: Atmospherically corrected reflectances using the estimated value of $\varepsilon_{(s,l)}$ and modelled values of the extrapolation-exponent.

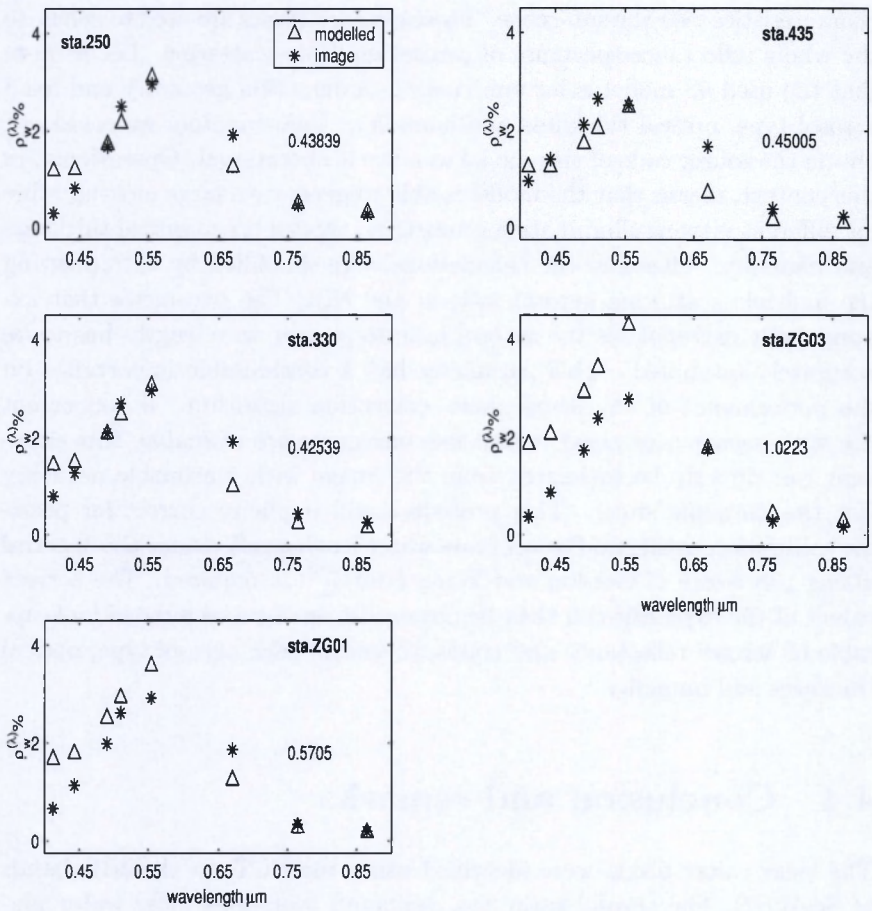

Fig. 4.7: Atmospherically corrected reflectances neglecting the coupled term in the extrapolation formula κ=1.

4.3.3 Operational set up

The aerosol dominant pixels over clear water pixels are isolated using the principal component transform. The aerosol ratio at the NIR is then derived from these pixels and assumed constant or spatially extrapolated to the neighboring pixels. This can be easily performed by calculating the eigenvectors of the covariance matrix of the data set. Then the aerosol ratio is simply the slope of the first eigenvector (w.r.t.v.). These values of estimated $\varepsilon_{(s,l)}$ are compared to pre-generated values for different aerosol types, optical thicknesses and humidities. The best fit will allocate the aerosol optical

characteristics over the sub-scene. These characteristics are used to generate the whole reflectance-spectrum of aerosol multiple scattering. Let us note that the used 6S model is for one viewing-illumination geometry and fixed aerosol type, optical thickness and humidity. Unfortunately we could not obtain the source code of this model to make it operational. Operational, in this context, means that the model is able to generate a large look-up table for different viewing-illumination geometries, aerosol type, optical thickness and humidity. Therefore the calculations were simplified by extrapolating the multiple scattering aerosol ratio at the NIR. The parameter that exponentially extrapolates the aerosol ratio to shorter wavelengths has to be accurately estimated. This parameter has a considerable importance on the performance of any atmospheric correction algorithm. If concurrent (i.e with sensor over pass) in-situ measurements are available, this exponent can directly be estimated from the image with reasonable accuracy (for the sampling sites). This procedure will implicity correct for possible calibration-artifacts. For accurate water leaving reflectance the spectral fitting procedure of Gordon and Wang (1994)[61] is required. The correct values of the exponent can then be obtained from a pre-simulated look-up-table of aerosol reflectance and coupled term for each aerosol type, optical thickness and humidity.

4.4 Conclusion and remarks

The clear water pixels were identified using the PCT on the NIR bands of SeaWiFS. The aerosol ratio was estimated over these clear water pixels. This was performed by calculating the eigenvectors of the covariance matrix of the clear water pixels. The aerosol ratio was then approximated as being the slope of the first eigenvector (w.r.t.v.). The resultant aerosol ratio was an accurate estimate of the aerosol scattering ratio at the NIR. The relative errors in the aerosol ratio (at the NIR) did not exceed 2% over all sites. The smallest value of the relative error (-0.16%) was at the station 330. This sampling site has the closest sampling time to image acquisition. The estimated value of $\varepsilon_{(s,l)}$=1.0494 was reasonable for all stations. This was confirmed by the low correlation coefficient of -2.15% between the aerosol and the water leaving reflectance at 0.765 μm. The correlation was slightly increased to -4.14% for aerosol and SPM. Two main groups were categorized from the relative errors in the aerosol ratio. The first group included clear water sites over which the aerosol ratio was underestimated.

The second group included turbid waters over which the aerosol ratio was overestimated. The separation between the two groups started at SPM concentrations of 15 g.m^{-3}. Suspended particles can be assumed as the only optically active component at the NIR. In other words the assumed value of the water reflectance ratio ($\alpha_{(s,l)} = a_w^{(l)}/a_w^{(s)}$) was reasonable for the SeaWiFS NIR bands. This ratio was larger than the modelled values by approximately 7-9%. However the assumption of constant values of water and atmospheric parameters $\alpha_{(s,l)}$ and $\varepsilon_{(s,l)}$ might reduced the spatial variations of water signal at the NIR. The aerosol ratio at the NIR has to be accurately extrapolated to shorter wavelengths to avoid overcorrection of recorded signals. This can only be realized by including the coupled term in the extrapolation exponent. On the other hand, good results were obtained by accounting for the coupled term using a linear relationship between single and multiple scattering aerosol ratio. This leads to the conclusion that the correction scheme is more sensitive to the spectral extrapolation of the aerosol ratio than its value at the NIR. These conclusions are correct for a well calibrated reflectance. This was implicitly included in the calculation of the extrapolation-exponent over the measurement sites. Actually without this implicit-correction the retrieved water leaving spectrum might fail in reproducing the chlorophyll absorption feature at 0.443μm.

Chapter 5

Coupled atmosphere-ocean model for rigorous solution of the atmospheric correction problem

Abstract

Most of the atmospheric correction procedures fail over turbid waters. This is due to the spatial variability of the water and aerosol reflectances and ratios at the NIR.

In this chapter a coupled atmosphere-ocean model is proposed for turbid waters. This algorithms considers, and retrieves, the spatial variability of the aerosol and water reflectance ratios at the NIR. Two assumptions were imposed on three bands at the NIR (>0.8 μm). First, the water leaving reflectance is optically governed by the SPM and water molecules. Second, the aerosol in the multiple scattering regime follows the same spectral dependency of the single scattering regime. With respect to these assumptions a rigorous solution to the atmospheric-correction problem was established. For each triplet of corrected reflectance exact values of the aerosol and water reflectance ratios are found.

The proposed method showed superiority on iterative approaches that do not employ a cost function. Moreover it retrieved the concentrations of SPM in turbid water from fluctuated data within acceptable accuracies ($<$ 10%).

Part of this chapter was published as (Salama and Monbaliu 2002)[95].

5.1 Introduction

The atmospheric correction algorithms discussed so far (sections 3.2 and 4.2), used a two-step procedure. The water leaving reflectance is first retrieved from the recorded signal (i.e. atmospheric correction). Then, the concentrations are derived via hydro-optical models (providing the specific inherent optical properties of the water column). In the first step, the water signal is assumed to have a known value at the NIR. This is equivalent to a constant value of SPM concentration. Which, in turn, determines the atmospheric path at this spectral region. This assumption is therefore not valid for optically complex waters (i.e. case II waters). An alternative approach is to retrieve the optical properties of both water and atmosphere simultaneously. For each atmosphere-ocean set-up a total reflectance can be simulated at a specific location and date. The parameters that define each media are tuned until the best convergence to the recorded reflectance is found. Figure (5.1) schematizes the above processing steps for the coupled system. This coupled atmosphere-ocean approach is increasingly used (Chomko *et al.*, 2003[96], Stamnes *et al.*, 2003[97], Gordon *et al.*, 1997[63], Zhao and Nakajima 1997[62]). However, all these algorithms were developed for case I waters (i.e. clear water). Again the water signal at the NIR was assumed spatially homogenous. Although the algorithm of Land and Haigh (1996)[98] was intended for case-II waters, it failed for waters with concentrations of chlorophyll-a and SPM larger than 0.2 mg.m^{-3} and 12.8 g.m^{-3} respectively. The Belgian coastal waters are more turbid than the above limits (Salama and Monbaliu 2003[99] and 2003[100]).

To the present there is no procedure that is applicable for turbid waters. This is due, as we argue in this chapter, to the spatial variability of the water signal at the NIR which was never accounted. At the NIR the the water leaving reflectance can be assumed to have only two unknowns. These are the ratio of aerosol reflectances (at bands s and l) $\varepsilon_{(s,l)}$ and the ratio of water leaving reflectances $\alpha_{(s,l)}$. A good atmospheric correction algorithm, in fact, means an accurate estimation of the aerosol and water

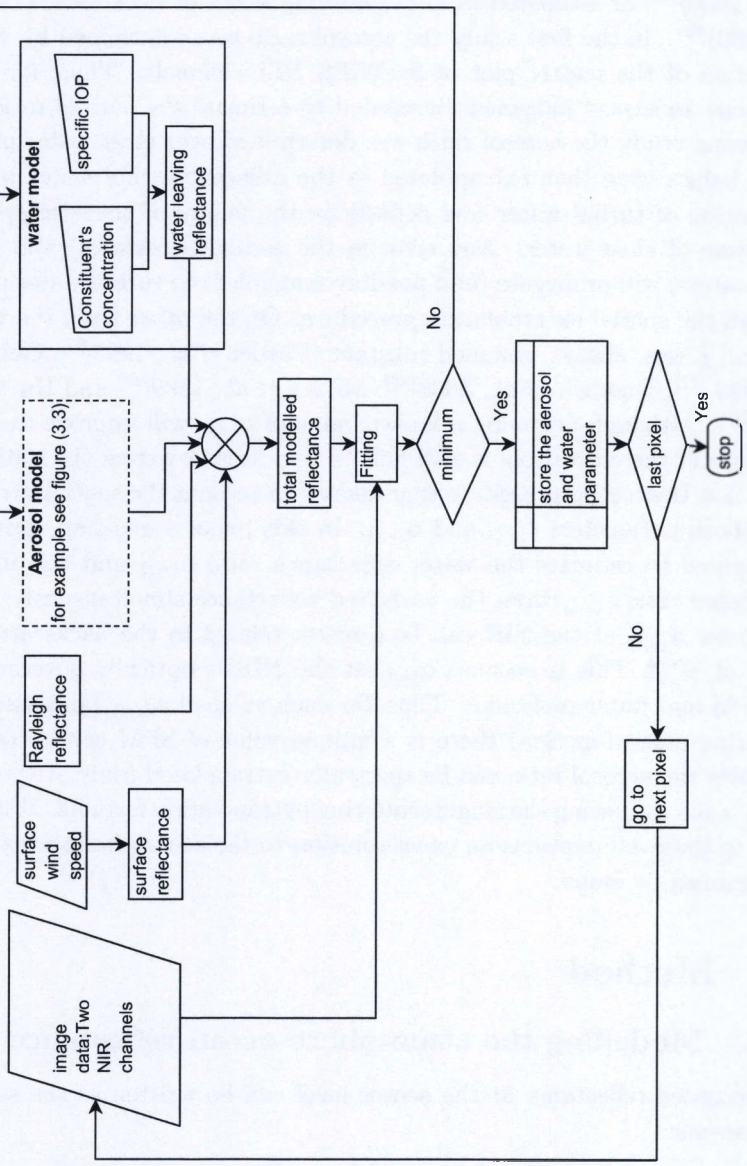

Fig. 5.1: The processing step for coupled atmosphere-ocean optimization.

reflectance ratios. The aerosol ratio was either assumed constant (Ruddick *et al.*, 2000)[68] or estimated from neighboring pixels of clear waters (Hu *et al.*, 2000)[69]. In the first study the aerosol ratio was determined by visual inspection of the scatter plot of SeaWiFS NIR channels. Thus, for each sub scene an expert judgement is needed to estimate the aerosol ratio. In the second study the aerosol ratio was determined over clear water pixels. These values were then extrapolated to the adjacent turbid water pixels. The region of turbid water was defined by the failure of the atmospheric correction of clear water. Any error in the estimated aerosol ratio (over clear waters) will propagate (and possibly magnified) to turbid-water pixels through the spatial extrapolation procedure. On the other hand the water ratio $\alpha_{(s,l)}$ was, always, assumed constant (Carder *et al.*, 1999[67], Gould *et al.*, 1999 [71], Ruddick *et al.*, 2000[68], Moore *et al.*, 1999[93] and Hu *et al.*, 2000[69]). Although assuming a known value of $\alpha_{(s,l)}$ will improve the performance of the correction, it still fails in very turbid waters (Li 2003)[72]. Up to now there is no procedure that takes into account the spatial variability of both parameters $\varepsilon_{(s,l)}$ and $\alpha_{(s,l)}$. In this paper a one-step approach is proposed to estimate the water reflectance ratio $\alpha_{(s,l)}$ and the aerosol reflectance ratio $\varepsilon_{(s,l)}$ from the corrected reflectance simultaneously. The parameter $\alpha_{(s,l)}$ at the NIR can be directly related to the backscattered-signal of SPM. This is because $\alpha_{(s,l)}$ at the NIR is optically governed by the SPM and water molecules. Thus, for each value of $\alpha_{(s,l)}$ (and assumed scattering phase-function) there is a unique value of SPM concentration. Moreover the aerosol ratio can be spectrally-extrapolated (only at the NIR bands > 0.8 μm) using the single scattering extrapolation formula. With respect to these assumptions an exact solution to the atmospheric-correction problem can be found.

5.2 Method

5.2.1 Modelling the atmosphere-ocean reflectance

The recorded reflectance at the sensor level can be written as the sum of components:

$$\rho_t^{(\lambda)} = T_g^{(\lambda)} \left\{ T_v^{(\lambda)} \rho_{sfc}^{(\lambda)} + \rho_a^{(\lambda)} + \rho_r^{(\lambda)} + \rho_{ra}^{(\lambda)} + T_v^{(\lambda)} \rho_w^{(\lambda)} \right\} \tag{5.1}$$

Where $T_g^{(\lambda)}$ and $T_v^{(\lambda)}$ are respectively the gaseous transmittance and the viewing diffuse-transmittance from ocean to sensor. The subscript of the

reflectance represents the contribution from surface (sfc) aerosol (a), air molecules (r), coupled scattering (ra) and the water leaving reflectance (w). The water leaving reflectance is the desired quantity that is related to the sea water physical and biological properties. Extracting this quantity from the total received reflectance is conventionally called atmospheric correction. The calculation of Rayleigh scattering of air molecules is well described in terms of geometry and pressure (Gordon *et al.*, 1988) [59]. The sea surface reflectance is generally small and it can be estimated using statistical relationships and wind speed (Cox and Munk 1954[54] and [55]). The gaseous transmittance can be calculated from ancillary data on ozone and water vapor concentrations using the transmittance models of Goody (1964)[46] and Malkums(1967)[47]. The viewing diffuse transmittance is approximated following Gordon *et al.* (1983)[48]. This leaves the aerosol and the coupled term reflectances and the water leaving reflectance to be derived. This requires knowledge (or assumptions) about the interrelationships between aerosol/water reflectances at two or more wavelengths.

The aerosol multiple-scattering ratio at two wavelengths (short s and long l) can be written as:

$$\varepsilon_{(s,l)} = \frac{\rho_a^{(s)} + \rho_{ra}^{(s)}}{\rho_a^{(l)} + \rho_{ra}^{(l)}} \tag{5.2}$$

Once the value of $\varepsilon_{(s,l)}$ is estimated, the water leaving reflectance at the shorter channel (s) is (from equation 5.1):

$$T_v^{(s)} \rho_w^{(s)} = \rho_c^{(s)} - \varepsilon_{(s,l)} \times \left(\rho_c^{(l)} - T_v^{(l)} \rho_w^{(l)} \right) \tag{5.3}$$

Where the corrected-reflectance is defined as the total reflectance corrected for gaseous absorption and Rayleigh and surface reflectances:

$$\rho_c^{(\lambda)} = \frac{\rho_t^{(\lambda)}}{T_g^{(\lambda)}} - \rho_r^{(\lambda)} - T_v^{(\lambda)} \rho_{sfc}^{(\lambda)} \tag{5.4}$$

The water leaving reflectances at the two bands s and l can be linked through their ratio as:

$$\alpha_{(s,l)} = \frac{T_o^{(l)} \rho_w^{(s)}}{T_o^{(s)} \rho_w^{(l)}} \tag{5.5}$$

Where T_o is the sun to sea transmittance. A further simplification can be

imposed (Ruddick *et al.*, 2000)[68]:

$$\frac{T_v^{(s)} T_o^{(s)}}{T_v^{(l)} T_o^{(l)}} = 1$$

Thus;

$$\frac{T_v^{(s)}}{T_v^{(l)}} \frac{\rho_w^{(s)}}{\rho_w^{(l)}} = \alpha_{(s,l)} \tag{5.6}$$

The water leaving reflectance can then be expressed by substituting (5.2 and 5.6) in (5.3) and solving for $\rho_w^{(l)}$:

$$\rho_w^{(l)} = \frac{\rho_c^{(s)} - \varepsilon_{(s,l)} \rho_c^{(l)}}{T_v^{(l)} \left(\alpha_{(s,l)} - \varepsilon_{(s,l)} \right)} \tag{5.7}$$

Assuming constant values of $\alpha_{(s,l)}$ and $\varepsilon_{(s,l)}$ is nothing more than enhancing the value of the water leaving reflectance (equation 2.73) with a constant factor e:

$$e = \frac{\alpha_{(s,l)}}{\alpha_{(s,l)} - \varepsilon_{(s,l)}} \tag{5.8}$$

Following the spectral dependency of the aerosol ratio, in the single scattering regime (equation 2.65), this magnifying factor will increase at shorter wavelengths. The spectral behavior of e tends to decrease the aerosol contribution at the blue bands.

5.2.2 Modelling the aerosol ratio

The single scattering aerosol ratio can be spectrally extrapolated from the pair of bands (s,l) to (i,l) where $i < s < l$ (Gordon and Wang 1994)[61]:

$$\varepsilon_{(i,l)}^{s} = \left(\varepsilon_{(s,l)}^{s} \right)^{\delta_i} \tag{5.9}$$

Where the exponent δ_i is:

$$\delta_i = \frac{l - i}{l - s} \tag{5.10}$$

If the band l is situated in the NIR part of the spectrum the ratio (equation 5.2) can be linked to its counterpart in the single scattering regime as (Gordon and Castano 1987)[49]:

$$\varepsilon_{(s,l)} = \kappa_{(s)} \varepsilon_{(s,l)}^{s} \tag{5.11}$$

Where $\kappa_{(s)}$:

$$\kappa_{(s)} = \left(1 + \frac{\rho_{ra}^{(s)}}{\rho_a^{(s)}}\right) \tag{5.12}$$

The multiple scattering aerosol ratio at the pair bands (s,l) can then be extrapolate to the bands (i,l) by substitute equation (5.11) in (5.9):

$$\varepsilon_{(i,l)} = \frac{\kappa_{(i)}}{\kappa_{(s)}^{\delta_i}} \left(\varepsilon_{(s,l)}\right)^{\delta_i} \tag{5.13}$$

If the bands i, s and l are selected to be situated in the NIR part of the spectrum (where $0.8 \leq i < s < l$ μm), the parameter $\kappa_{(\lambda)}$ (equation 5.13) can then be assumed spectrally flat. This is due to the weak contributions of coupled term and aerosol scattering to the atmospheric path at this spectral region, thus (see equation 5.12):

$$\frac{\rho_{ra}^{(i)}}{\rho_a^{(i)}} \sim \frac{\rho_{ra}^{(s)}}{\rho_a^{(s)}} \tag{5.14}$$

Using this assumption (5.14) in equation (5.13) gives:

$$\varepsilon_{(i,l)} = \kappa^{1-\delta_i} \left(\varepsilon_{(s,l)}\right)^{\delta_i} \tag{5.15}$$

5.2.3 Modelling the water ratio

The water leaving reflectance is to the first order proportional to the water inherent optical properties (Gordon *et al.*, 1988)[9]:

$$\frac{\rho_w^{(\lambda)}}{T_0^{(\lambda)}} = 0.54\pi l_1 \frac{b_b(\lambda)}{b_b(\lambda) + a(\lambda)} \tag{5.16}$$

$l_1 = 0.0949$ is the subsurface expansion coefficients due to internal refraction, reflection and sun zenith; $T_0^{(\lambda)}$ is the solar transmittance from sun-to-target; $b_b(\lambda)$ and $a(\lambda)$ are the bulk backscattering and absorption coefficients of the surface water, respectively. The constant number 0.54 describes the fraction of transmitted light from below the water surface. At the NIR part of the spectrum the water leaving reflectance column is assumed to be optically governed by the SPM backscattering $b_{b(spm)}(\lambda)$ and the water

absorption $a_w(\lambda)$ coefficients:

$$a(\lambda) = a_w(\lambda) \tag{5.17}$$

$$b_b(\lambda) = b_{b(spm)}(\lambda) = b^*_{b(spm)}(\lambda) \times C_{spm} \tag{5.18}$$

Where $b^*_{b(spm)}(\lambda)$ and C_{spm} are the specific backscattering coefficient and the concentrations of SPM, respectively. Substituting the inherent optical properties of (5.17 and 5.18) in the right hand side of equation (5.16), the water ratio (equation 5.5) can then be written such as:

$$\alpha_{(s,l)} = \frac{b^*_{b(spm)}(s)}{b^*_{b(spm)}(l)} \times \frac{a_w(l) + b_{b(spm)}(l)}{a_w(s) + b_{b(spm)}(s)} \tag{5.19}$$

The parameter $\alpha_{(s,l)}$ is expected to be a smooth function of SPM in clear water. This ratio was therefore assumed to be constant (Carder *et al.*, 1999 [66] and [67], Ruddick *et al.*, 2000[68], Hu *et al.*, 2000[69]). Figure (5.2) shows that this assumption (constant $\alpha_{(s,l)}$) is only correct for a certain wavelengths and a range of SPM concentrations. For instance the value of $\alpha_{(0.858,0.87)}$ can be considered constant over a wide range of SPM concentrations. The wavelength dependency of $\alpha_{(s,l)}$ is directly related to that of

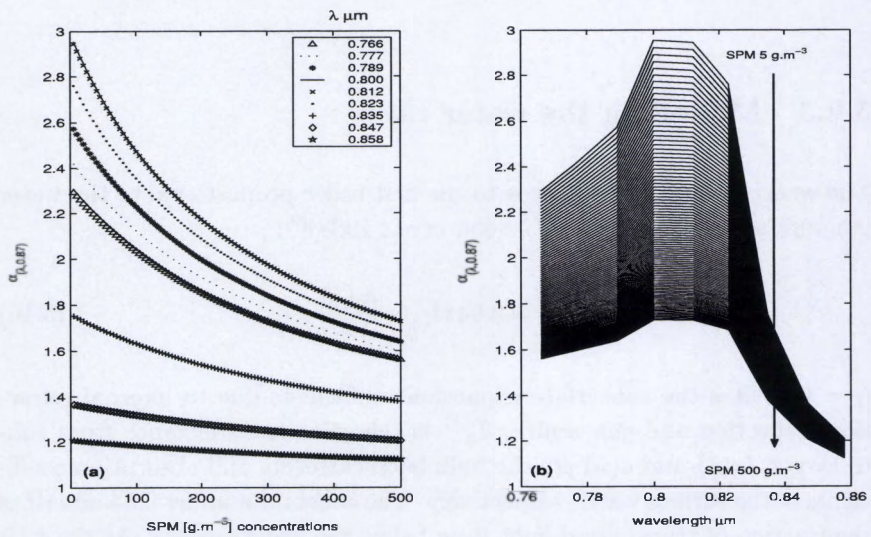

Fig. 5.2: The variation of the water ratio $\alpha_{(s,l)}$ as a function of SPM concentrations (a) and wavelength (b). The reference (l) band was fixed to 0.87μm.

the water leaving reflectance (figure 5.2(b)). The water leaving reflectance has a unique peak between 0.8-0.82 μm. This is due to the low values of the water absorption coefficient at this spectral region. Therefor $\alpha_{(s,l)}$ will have the highest variation, as a function of SPM concentrations, at the spectral range between 0.8 and 0.82 μm (figure 5.2(a)). Figure(5.2(a)) shows that for each value of $\alpha_{(s,l)}$ (and assumed scattering phase-function) there is a unique value of SPM concentrations and $\alpha_{(i,l)}$ such as (from equation 5.19):

$$C_{spm} = \frac{\eta_{(l)} - \alpha_{(s,l)}\eta_{(s)}}{\alpha_{(s,l)} - 1} \tag{5.20}$$

where:

$$\eta_{(\lambda)} = \frac{a_w(\lambda)}{b^*_{b(spm)}(\lambda)} \tag{5.21}$$

Therefore $\alpha_{(i,l)}$ can be linked to $\alpha_{(s,l)}$ (only at $\lambda \geq 0.8\mu$m) through the associated SPM concentration as:

$$\alpha_{(i,l)} = \alpha_{(s,l)} \frac{\eta_{(l)} - \eta_{(s)}}{\left(\eta_{(l)} - \eta_{(i)}\right) + \alpha_{(s,l)}\left(\eta_{(s)} - \eta_{(i)}\right)} \tag{5.22}$$

5.2.4 Imposed boundaries

The task is to find accurate estimates of $\alpha_{(s,l)}$ and $\varepsilon_{(s,l)}$ that improve the accuracy of the retrieved water leaving spectrum. It is quite important to bound our searching procedure with some physical constraints. The ratio $\rho_c^{(s)} \Big/ \rho_c^{(l)}$ (see equation 5.7) will have some boundary information about the sought parameters $\alpha_{(s,l)}$ and $\varepsilon_{(s,l)}$.

The estimated aerosol reflectance at band (l) should be positive and less than the corrected reflectance at this band:

$$\rho_a^{(l)} \leq \rho_c^{(l)} \tag{5.23}$$

The aerosol reflectance can be expresses as (substitute equation 5.7 in 5.1 and solve for $\rho_a^{(l)}$):

$$\rho_a^{(l)} = \frac{\alpha_{(s,l)}\rho_c^{(l)} - \rho_c^{(s)}}{\alpha_{(s,l)} - \varepsilon_{(s,l)}} \tag{5.24}$$

Substituting the right hand side of equation (5.24) in the inequality (5.23) yields:

$$\varepsilon_{(s,l)} \leq \frac{\rho_c^{(s)}}{\rho_c^{(l)}} \tag{5.25}$$

If a third band i is available at the NIR (where $0.8 \leq i < s < l$ μm), the boundaries on ratio $\varepsilon_{(\lambda,l)}$, for a non-absorbing aerosol, can be constructed from (5.25) such as:

$$0 \leq \varepsilon_{(s,l)} \leq \frac{\rho_c^{(s)}}{\rho_c^{(l)}} \tag{5.26}$$

$$0 \leq \varepsilon_{(i,l)} \leq \frac{\rho_c^{(i)}}{\rho_c^{(l)}} \tag{5.27}$$

Its is assumed that there is always a non-absorbing aerosol and small values of the coupled term. These assumptions are valid at the NIR due to the negligible aerosol absorption and Rayleigh scattering at this spectral range. The bound (5.27) on $\varepsilon_{(i,l)}$ can be transformed to a bound on $\varepsilon_{(s,l)}$ using equation (5.15) with $\kappa_{(\lambda \geq 0.8\mu m)} = 1$ such as:

$$0 \leq \varepsilon_{(s,l)} \leq \left(\frac{\rho_c^{(i)}}{\rho_c^{(l)}} \right)^{1/\delta_i} \tag{5.28}$$

Equivalent to (equation 5.23), the estimated water leaving reflectance at band (l or s) should be positive and less than the corrected reflectance at this band:

$$T_v^{(l)} \rho_w^{(l)} \leq \rho_c^{(l)} \tag{5.29}$$

Substituting the above inequality in equation (5.7) we can find:

$$\frac{\rho_c^{(s)}}{\rho_c^{(l)}} \leq \alpha_{(s,l)} \tag{5.30}$$

The condition of non-negative concentration C_{spm} >0 of equation (5.20) yields two cases:

$$\alpha_{(s,l)} < \frac{\eta_{(l)}}{\eta_{(s)}} \quad \text{if} \quad \alpha_{(s,l)} > 1 \tag{5.31}$$

$$\alpha_{(s,l)} > \frac{\eta_{(l)}}{\eta_{(s)}} \quad \text{if} \quad \alpha_{(s,l)} < 1 \tag{5.32}$$

Let us note that the reference band l of the water ratio was selected to be far in the NIR 0.87μm. This was to achieve a maximum variability in the $\alpha_{(s,l)}$ w.r.t. SPM concentrations (re-consult section 5.2.3). Hence the ratio $\alpha_{(s,l)}$ is always greater than 1 in the NIR (see figure 5.2). The lower and

upper bounds on $\alpha_{(s,l)}$ are therefore:

$$\frac{\rho_c^{(s)}}{\rho_c^{(l)}} \leq \alpha_{(s,l)} \leq \frac{a_w(l)}{b_{b(spm)}(l)} \frac{b_{b(spm)}(s)}{a_w(s)} \tag{5.33}$$

Assuming a spectrally flat backscattering coefficient (Gould *et al.*, 1999)[71], the upper boundary will approach a constant value of $a_w(l)/a_w(s)$. The above bounds (inequality 5.33), are valid with respect to the following condition:

$$\begin{array}{ccccc} i & < & s & < & l \\ a_w(i) & < & a_w(s) & < & a_w(l) \end{array} \tag{5.34}$$

The bands i, s and l should therefore be selected with respect to (5.34). This is not a difficult task in the NIR, where the water absorption increases with wavelengths. Nevertheless the conditions in (5.34) together with the observation of figure (5.2) exactly determine the optimum bands such as: i is within the range 0.8-0.82 μm and the bands s and l are $> 0.82\mu$m with $s < l$.

5.2.5 Rigorous solution for the atmosphere-ocean system

The water leaving reflectances at band l can be calculated using the corrected reflectance at the band i as (equivalent to equation 5.7):

$$\rho_w^{(l)} = \frac{\rho_c^{(i)} - \varepsilon_{(i,l)} \rho_c^{(l)}}{T_v^{(l)} \left(\alpha_{(i,l)} - \varepsilon_{(i,l)} \right)} \tag{5.35}$$

Equation (5.7) has two unknowns namely the aerosol ratio $\varepsilon_{(s,l)}$ and the water ratio $\alpha_{(s,l)}$. Equation (5.35) will add two other unknowns namely $\alpha_{(i,l)}$ and $\varepsilon_{(i,l)}$. The ratios $\varepsilon_{(s,l)}$ and $\varepsilon_{(i,l)}$ can be interlinked knowing their spectral dependance. At the NIR part of the spectrum (where $0.8 \leq i < s < l$ μm) the effect of the coupled term on the aerosol scattering can be neglected (i.e. κ=1). This is due to the weak contribution of Rayleigh scattering to the atmospheric path. This approximation allows to spectrally extrapolate the multiple scattering aerosol ratio at the NIR using the same spectral dependency of the single scattering aerosol ratio (equation 5.15 with κ=1). On the other hand the ratio $\alpha_{(s,l)}$ can be linked to $\alpha_{(i,l)}$ through the associated SPM concentrations (equation 5.22). This parametrization reduces the number of variables in both equations (5.7 and 5.35) to two

only. The water leaving reflectance at the NIR (equations 5.7 or 5.35) is, therefore, function of two parameters. The first is the water ratio $\alpha_{(\lambda,l)}$ which is related to SPM concentrations at specific wavelength (figure 5.2). The second is the aerosol ratio $\varepsilon_{(\lambda,l)}$ which is related to the aerosol type and optical thickness with λ being i or s. These two parameters represent two different media (atmosphere and water) and therefore are physically unrelated. Minimizing the difference between the water leaving reflectance estimated from equations (5.7 and 5.35) might result in close estimates of the sought values (i.e. $\alpha_{(s,l)}$ and $\varepsilon_{(s,l)}$):

$$f_1 = \left(\rho_w^{(l)}(\text{eq.5.7}) - \rho_w^{(l)}(\text{eq.5.35})\right)^2 \tag{5.36}$$

Where (eq.5.7) and (eq.5.35) refer to the equations from which the water leaving reflectance was calculated. The cost function (equation 5.36) is at its ultimate minimum when f_1=0. Rearranging the terms of the equation (5.36 when f_1=0) gives:

$$A_\varepsilon \varepsilon_{(s,l)}^{\delta_i} + B_\varepsilon \varepsilon_{(s,l)} + C_\varepsilon = 0 \tag{5.37}$$

Where the coefficients A_ε, B_ε and C_ε are given by:

$$\begin{aligned} A_\varepsilon &= \rho_c^{(s)} - \alpha_{(s,l)}\rho_c^{(l)} \\ B_\varepsilon &= \alpha_{(i,l)}\rho_c^{(l)} - \rho_c^{(i)} \\ C_\varepsilon &= \alpha_{(s,l)}\rho_c^{(i)} - \alpha_{(i,l)}\rho_c^{(s)} \end{aligned} \tag{5.38}$$

Equation (5.37) represents the locus of the solution region at which f_1 attained its ultimate minimum. The retrieved parameters form equation (5.36 or 5.37) are, however, interdependent. This because the two variables were extracted from one equation. This dependency can be resolved by introducing another quantity (SPM concentration) that is directly related to the water ratio $\alpha_{(s,l)}$ and independent of the aerosol ratio $\varepsilon_{(s,l)}$. As it was previously illustrated (figure 5.2) the water ratio $\alpha_{(\lambda,l)}$ is a function of SPM concentrations at the spectral range for λ between 0.8 and 0.82 μm (l being 0.87μm). These concentrations of SPM are totaly independent of the aerosol ratio when retrieved from the water ratio. Following this reasoning two values of SPM concentrations can be quantified. The first being estimated from the water leaving reflectance (equation 5.7) using the hydro-optical

model (5.16), such as:

$$C_{spm} = \frac{\eta_{(l)}\rho_w^{*(l)}}{1 - \rho_w^{*(l)}} \tag{5.39}$$

Where:

$$\rho_w^{*(\lambda)} = \frac{\rho_w^{(\lambda)}}{T_0^{(\lambda)} 0.54\pi l_1} \tag{5.40}$$

The second is computed from $\alpha_{(s,l)}$ (equation 5.20). The values of the aerosol and water ratios can be tuned until a minimum difference between the concentrations of equations (5.39) and (5.20) is realized. In other words the following function can also be minimized with respect to $\alpha_{(s,l)}$ and $\varepsilon_{(s,l)}$:

$$f_2 = \left(C_{spm}(\text{eq.5.39}) - C_{spm}(\text{eq.5.20})\right)^2 \tag{5.41}$$

Where (eq.5.39) and (eq.5.20) refer to the equations from which the SPM concentrations were calculated. In the same manner of equation (5.37), setting the cost function (5.41) to zero (ultimate minimum) and rearranging the terms yield:

$$A_\alpha \alpha_{(s,l)}^2 + B_\alpha \alpha_{(s,l)} + C_\alpha = 0 \tag{5.42}$$

Where the coefficients A_α, B_α and C_α are given by:

$$\begin{aligned} A_\alpha &= \eta_{(s)} \\ B_\alpha &= -\eta_{(l)} - \varepsilon_{(s,l)}\eta_{(s)} - \left(\eta_{(s)} - \eta_{(l)}\right)\left(\rho_c^{*(s)} - \varepsilon_{(s,l)}\rho_c^{*(l)}\right) \\ C_\alpha &= \varepsilon_{(s,l)}\eta_{(l)} \end{aligned} \tag{5.43}$$

Where $\rho_c^{*(\lambda)}$ is the corrected reflectance normalized to same dominator of equation (5.40). The curves in equation (5.42) is the locus of the smallest values of the cost function (5.41: f_2=0).

Both functions (equations 5.37 and 5.42) are under-determined in the sense that the number of variables exceed the number of equations. However the simultaneous solution of these equations, or equivalently the simultaneous minimization of the cost functions (5.36) and (5.41), is a determined problem:

$$cost = \text{Minimize}\,(f_1)\,\text{with respect to Minimizing}\,(f_2) \tag{5.44}$$

This can mathematically be explained by the inverse theory as follows (Press *et al.*, 2002)[101]. The cost function (5.36) can be regarded as a priori judgement about the likelihood of the resulting water leaving reflectance at band

l. On the other hand the cost function (5.41) measures the agreement of the SPM retrieved from two related quantities. In other words, linking the measured reflectance to the underlying scattering-processes of SPM at the NIR. Minimizing each one of these function apart will improve the accuracy of one parameter while the accuracy of the other parameter is deteriorated. The inverse theory suggests that the minimizing the weighted sum of (5.36) and (5.41), will lead to a unique solution for the sought parameters. The cost function in (equation 5.44) can be written as:

$$cost = \text{Minimize}\left((f_1)^2 + \lambda\,(f_2)^2\right) \tag{5.45}$$

where λ is the lagrange multiplier which can take a value between 0 and ∞. This term was set to one (λ=1), subjectively. The objective determination of the lagrange multiplier is left for future improvement on the algorithm. Let us note that the first term f_1 of equation (5.45) should be expressed as concentrations of SPM using equation (5.39). The cost function (equation 5.45) is at its minimum when both terms f_1 and f_2 have zero values at this minimum. In other words minimizing the cost function (5.45) should in principles give the same results as solving the equations (5.37) and (5.42) simultaneously. However, justifying this statement is out the scope of this study. Instead, it will be shown that solving 5.37 and 5.42, within the boundaries of $\varepsilon_{(s,l)}$ and $\alpha_{(s,l)}$, results in an exact and unique solution of the atmosphere-ocean system. The verification of this statement will be in section (5.3.2).

5.3 Results and discussion

5.3.1 Simulated data

The multiple scattering aerosol reflectance ratio was computed from the simulated data (figures 5.12). This ratio was then extrapolated to shorter wavelength using the single scattering extrapolation formula (equations 5.9 and 5.10). The resulting aerosol reflectance was then summed to the simulated water leaving reflectance (figure 5.13) to produce the corrected reflectance. These simulated reflectance were used through out this chapter except for section (5.3.4). Three NIR bands were chosen ($i = 0.815\mu$m, $s = 0.835\mu$m and $l = 0.87\mu$m) such that they satisfy the conditions of section (5.2.4) and the observation of figure (5.2).

5.3.2 Results of the rigorous solution

Equations (5.37 and 5.42) were applied on the simulated atmosphere-ocean reflectance. Figure (5.3) illustrates the behavior of these functions (5.37 and 5.42) with respect to the sought variables $\alpha_{(s,l)}$ and $\varepsilon_{(s,l)}$. Figure (5.3) shows that for all atmosphere-ocean combinations the two solutions curves ('LocusW' and 'LocusA' in figure 5.3) intersect at a specific point which corresponds to a pair of the aerosol and the water ratios. The coordinates of the intersection points (figure 5.3) can be retrieved by solving the set of equations (5.37 and 5.42) simultaneously. This is equivalent to minimizing the cost function (5.45) with respect to the aerosol and water reflectance ratios. This is because at this intersection point both cost functions (f_1 and f_2) have minimum values and hence their sum (5.45). Therefore, minimizing the two-component cost function (5.45) with respect to $\alpha_{(s,l)}$ and $\varepsilon_{(s,l)}$ should in principle give the coordinates of the intersection point of figure (5.3). Actually both methods (i.e. solving the set of equations 5.37 and 5.42 and minimizing 5.45) gave exactly the same answer when applied on the simulated data (section 5.5.1). The major conclusion is that, solving the set of equations (5.37 and 5.42) provides a unique solution vector $[\alpha_{(s,l)}, \varepsilon_{(s,l)}]$ for each triplet of corrected reflectances ($\rho_c^{(i)}$, $\rho_c^{(s)}$ and $\rho_c^{(l)}$). This conclusion is valid with respect to the imposed assumptions in sections (5.2.2 to 5.2.4). As we can see from figure (5.3) the solution curve 'LocusW' has relatively small variation w.r.t. $\varepsilon_{(s,l)}$ and large variation w.r.t. $\alpha_{(s,l)}$ in clear waters. This large variation is reduced w.r.t. $\alpha_{(s,l)}$ in turbid waters. This also means that the function (5.37) is less sensitive to the values of $\alpha_{(s,l)}$ in clear water. This observation will be used in section (5.3.4). On the other hand the solution curve (5.42, the curve 'LocusA' in figure 5.3) has a large variation w.r.t. $\varepsilon_{(s,l)}$ and small variation w.r.t. $\alpha_{(s,l)}$ in clear water. i.e. the function (5.42) is less sensitive to the variations in $\varepsilon_{(s,l)}$. These variations of $\alpha_{(s,l)}$ and $\varepsilon_{(s,l)}$ are increased in turbid water, hence the sensitivity of (5.42). These outcomes justify the use of the two cost-functions (5.36 and 5.41) for turbid water and high aerosol optical thickness. Moreover they validate our anticipated idea for turbid waters which was the spatial variability of the aerosol and water ratios.

Figure (5.4) shows the relative errors in the retrieved parameters ($\alpha_{(s,l)}$, $\varepsilon_{(s,l)}$ and SPM) and the root sum-of-squares of the residuals in (5.37) and (5.42). The main observation in figure (5.4) is that the relative errors in the retrieved parameters and the root sum-of-squares of the residuals are very small and independent of water types and/or aerosol models. This gives

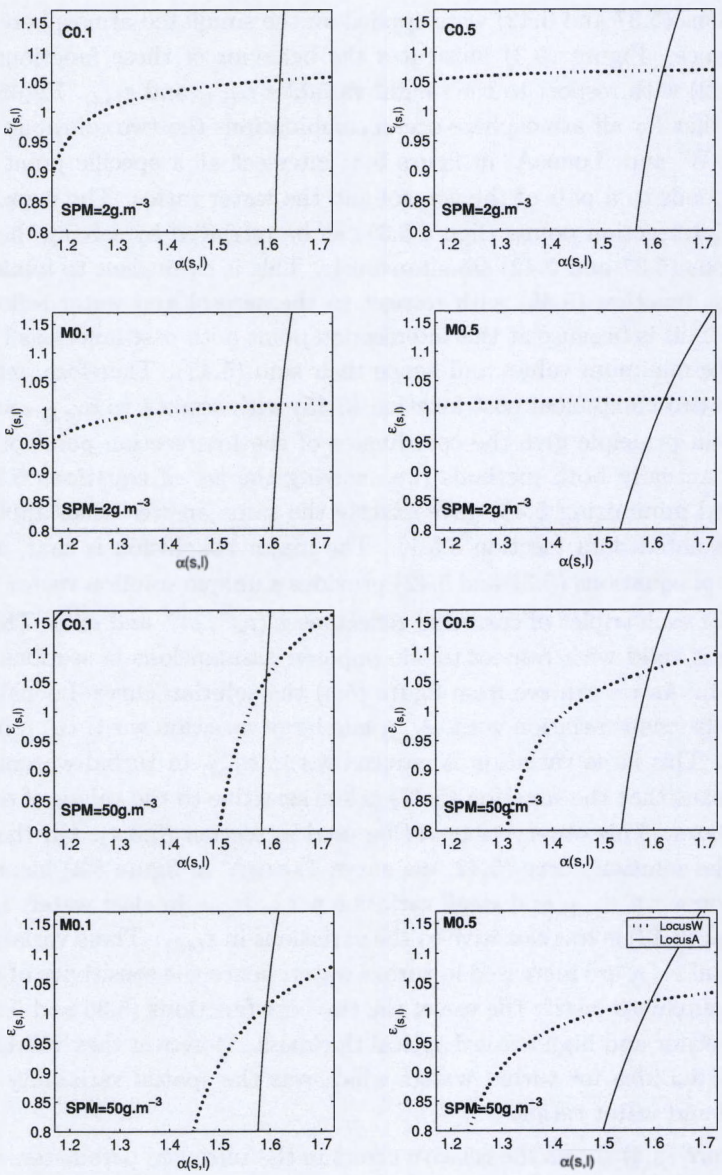

Fig. 5.3: The locus of the solution region (equations 5.37 'LocusW' and 5.42 'LocusA'). The curves are plotted within the bounds (equations 5.26 and 5.33). These curves are for extreme combinations of aerosol types with small/large optical thickness and clear/turbid waters.

confidence about the numerical scheme that has been employed to solve the set of equations(5.37 and 5.42) and /or minimize the cost function (5.45).

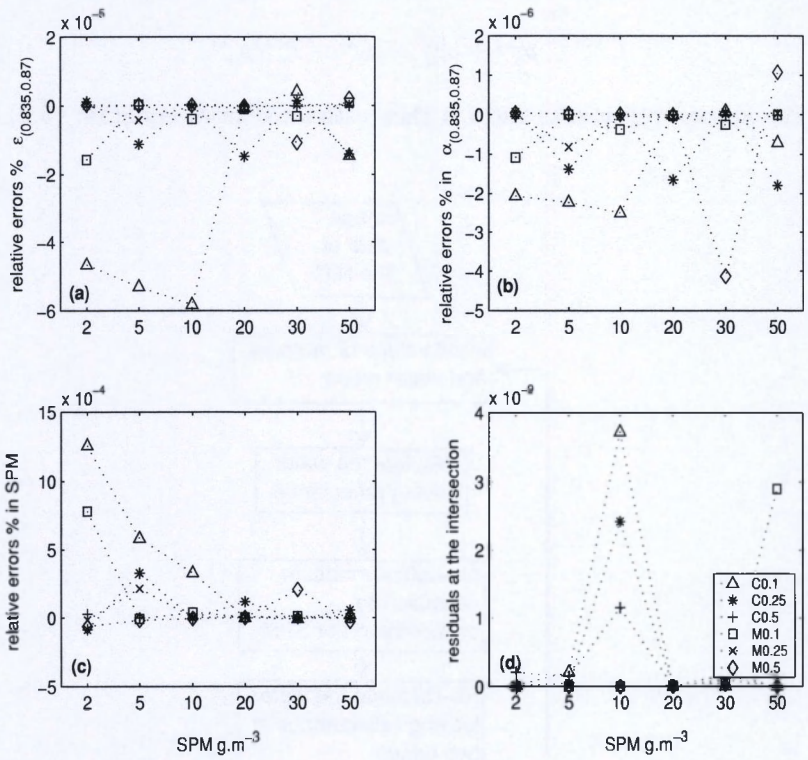

Fig. 5.4: (a): relative errors in $\varepsilon_{(0.835,0.87)}$. (b): relative errors in $\alpha_{(0.835,0.87)}$. (c): relative errors in SPM. (d): the root sum-of-squares of residuals at the intersection points (see figure 5.3).

5.3.3 Validation with iterative methods

The algorithm was compared with an iterative approach that does not employ a cost function (e.g. Andre and Morel 1991[74] and Moor *et al.*, 1999[93]) and solve for the atmosphere-ocean system. These approaches were adapted to account for the spatial variation in the water reflectance ratio as follows. The water leaving reflectance at the NIR band l is estimated from equation (5.7) using initial values of aerosol and water ratios. This reflectance is then feeded into equation (5.39) to calculate the concentration of SPM. The resulting concentration is used in equation (5.16) to compute the corre-

sponding water leaving reflectance at two bands s and l. These reflectances are substituted in equation (5.5) to evaluate the ratio $\alpha_{(s,l)}$. The aerosol reflectance at band λ is calculated as (consult equations 5.1 and 5.4):

$$\rho_a^{(\lambda)} + \rho_{ra}^{(\lambda)} = \rho_c^{(\lambda)} - T_v^{(\lambda)} \rho_w^{(\lambda)} \tag{5.46}$$

The aerosol reflectance ratio is then estimated from equation (5.2). The

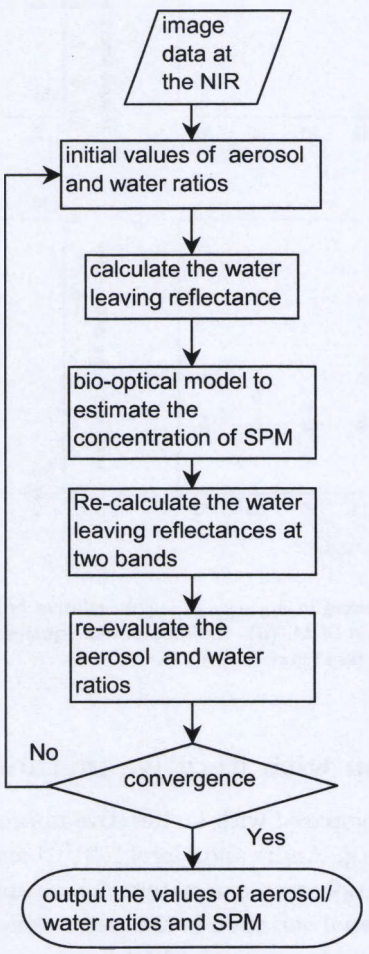

Fig. 5.5: An iterative atmospheric correction approach that does not employ a cost function.

resulting values of the aerosol and water ratios are again feeded into equation (5.7) and the above steps are repeated till convergence is achieved i.e. the values of $\varepsilon_{(s,l)}$ and $\alpha_{(s,l)}$ do not change with iterations. These steps are schematically shown in figure (5.5). This method (figure 5.5) can be regarded as a direct combination of the two pre-mentioned approaches in figures (3.2) and (4.2). The results of this approach are shown in figure (5.6). As we can see (figure 5.6(a)) there is a clear separation between maritime and continental aerosol models regarding their relative errors in $\varepsilon_{(s,l)}$. The relative errors in $\varepsilon_{(s,l)}$ for continental aerosol vary from -2% for C0.1 to -6.2% for C0.5. This variation decreased for the maritime aerosol model to be -1.8% for M0.5 and 0.25 for M0.1 %. In other words, the relative error in the aerosol ratio is larger for the continental aerosol than the maritime aerosol and increases with their optical thicknesses. The same trend can be observed for $\alpha_{s,l)}$ (figure 5.6(b)). Moreover the model overestimated and underestimated SPM concentrations in clear and turbid waters respectively. This tendency can be better illustrated for high concentration of SPM. The concentrations were assumed to vary (in the simulated data) from 10 to 250 g.m^{-3}. The SPM concentrations were then estimated using the iterative algorithm (figure 5.5) and the proposed algorithm (figure 5.3 or equivalently equation 5.45). The results of the two approaches are compared in figure (5.7) using the root-square (i.e. absolute errors) of SPM errors. The accuracy of the retrieved SPM concentrations from the iterative approach (figure 5.7(b)) is strongly related to water turbidity, aerosol

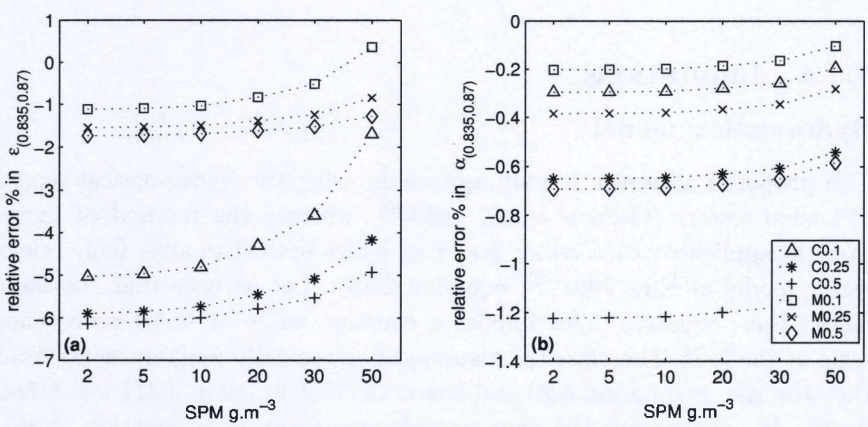

Fig. 5.6: The relative errors in the estimated values of (a): $\varepsilon_{(s,l)}$ and (b): $\alpha_{(s,l)}$ using the iterative approach of figure (5.5).

type and aerosol optical thickness. Let us note that there is a clear threshold of SPM concentration under/above which the iterative approach (figure 5.7(b)) starts to over-/under-estimate the concentration of SPM. The value of this threshold is strongly related to the aerosol optical thickness. In the sense that it is independent of aerosol type (maritime or continental) and increases with aerosol optical thickness. The iterative model (figure 5.5) is most appropriate for the maritime aerosol type with small value of aerosol optical thickness (≤ 0.1). This is in contrary to the proposed method which was appropriate for all aerosol types and waters models.

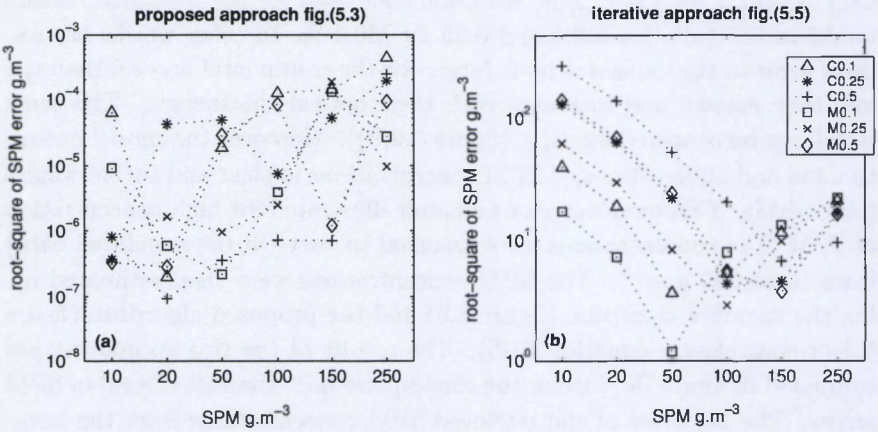

Fig. 5.7: The root-square of SPM errors using (a): the proposed approach (figure 5.3) and (b): the iterative approach (figure 5.5).

5.3.4 Limitations

Hydro-optical model

The proposed approach is only applicable using the hydro-optical model of turbid waters (Gordon *et al.*, 1988)[9], whereas the method of figure (5.5) is applicable to a wider range of hydro-optical models (e.g. clear water model of Kirk 1991[70], equation 2.76). Let us note that the later model (i.e. equation 2.76) implies a constant value of water reflectance ratio at the NIR. Therefore the assumption of spatially variably water ratio (i.e. the use of equation 5.20 and hence the cost function 5.41) will break down. In consequence the only possible cost function is equation (5.36), or equivalently equation (5.37), which is expected to be more efficient than the iterative method. This is because equation (5.37) is less sensitive to the

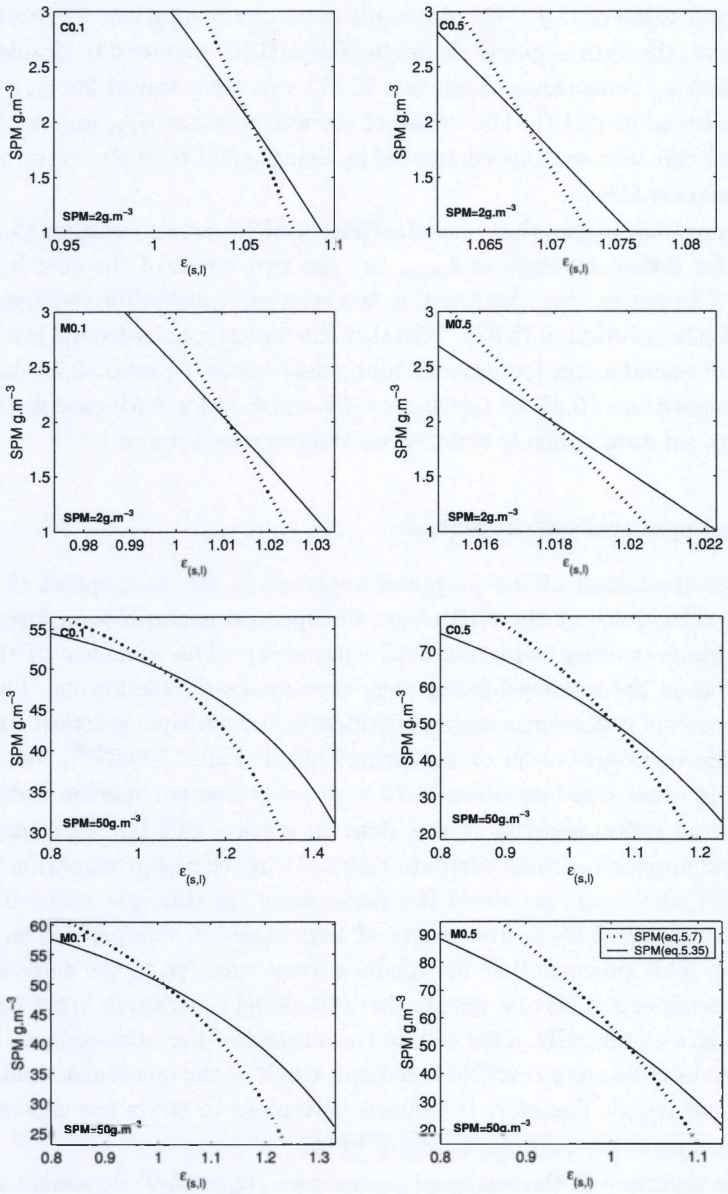

Fig. 5.8: The two terms of the cost function (5.36) expressed as SPM concentrations using Kirk-model (2.76). Note that the intersection points are the solutions of equation (5.37) with constant values of $\alpha_{(\lambda,0.87)}$.

values of $\alpha_{(s,l)}$ in clear waters (figure 5.3). If the water column optically behaves according to the Kirk-model (2.76), then solving (5.37), for $\varepsilon_{(s,l)}$ with fixed value of $\alpha_{(s,l)}$, should result in an exact solution. To verify this statement, the hydro-optical model (equation 2.76) was used to simulate the water leaving reflectance. Equation (5.37) was then solved for $\varepsilon_{(s,l)}$ using (2.76) instead of (5.16). The values of the water ratios $\alpha_{(s,l)}$ and $\alpha_{(i,l)}$ were assumed constant and approximated as being equal to their upper bounds (see equation 5.33).

Figure (5.8) shows the concentrations of SPM estimated from (5.7) and (5.35) for different values of $\varepsilon_{(s,l)}$, i.e. the two terms of the cost function (5.36). Obviously, this cost function has zero value at the intersection point which is the solution of (5.37). Whether the underlying hydro-optical model is that of turbid water (equation 5.16) or clear water (equation 2.76) the proposed algorithms (5.45 for Gordon-model and 5.37 for Kirk-model) provide an exact solution which is superior on the iterative approach.

Aerosol spectral extrapolation

A major limitation of the proposed approach is the assumption that the aerosol reflectance at the NIR obeys the spectral extrapolation formula of the single scattering (equation 5.15 with κ=1). The influence of this assumption on the retrieved parameters were assessed as following. The simulated aerosol reflectances were generated in the multiple scattering regime using the successive order of scattering (van de Hulst 1998[27], see section 5.5.1). In other word equation (5.15 with κ=1) was not used in simulating the aerosol reflectances as it was done in section (5.3.1). The algorithm was then applied on these simulated data. Using this approximation (equation 5.15 with κ=1) increased the uncertainty (in this case relative error) on SPM (figure 5.9(c)) five orders of magnitude in comparison to figure (5.4(c)). This suggests that the model is very sensitive to the aerosol spectral dependency. This also means that the model is sensitive to fluctuations in the data at the NIR. This will be the subject of the next section. Let us note the relative errors in SPM is a direct result of the combined-errors from $\varepsilon(s,l)$ and $\alpha_{(s,l)}$. Therefore it is more convenient to study the end-effect of these errors on the concentrations of SPM.

The accuracy of the retrieved parameters (figure 5.9) depends more on the water turbidity than on the aerosol type. This because the model will give the best results for the aerosol type which has the closest value of δ^* (see equation 4.4), in this case M0.25 and C0.5, to the approximation

(5.10). On the other hand it seems that the model is more suitable for turbid water than clear waters. The reason is that turbid water has a more distinctive signature at the NIR than clear water in comparison to the aerosol reflectance (consult figure 5.2 and compare the two figures 5.12 and 5.13).

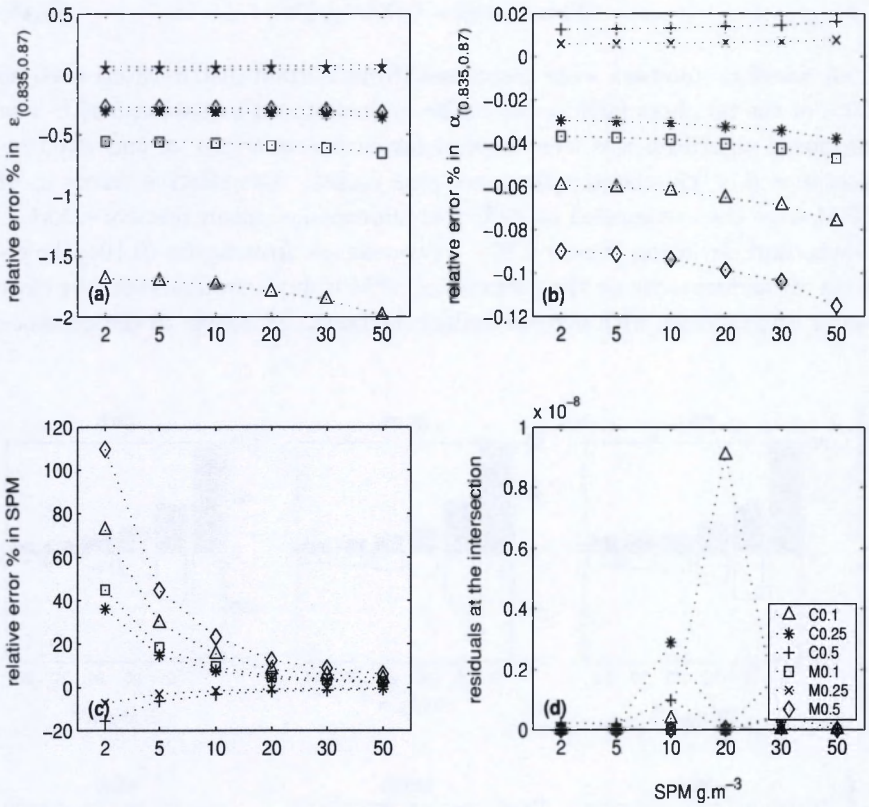

Fig. 5.9: (a): relative errors in $\varepsilon_{(0.835,0.87)}$. (b): relative errors in $\alpha_{(0.835,0.87)}$. (c): relative errors in SPM. (d): the root sum-of-squares of the residuals at the intersection points (see figure 5.3).

Sensitivity to random noise

Normally the sensitivity of the sensor plays an important role in determining the signal to noise ratio (SNR). However the SNR over water is relatively small at the NIR. This is due to the weak signal that is leaving the water

surface. Even in very turbid waters this signal will not exceed few presents. In consequence the NIR spectral range is more likely to be subjected to random noise. The sensitivity of the proposed model to small fluctuations in the data was tested as follows. The noise level was set to be 0.5% of the corrected reflectance:

$$\text{Noise-Level} = 0.005 \times \rho_c^{(\lambda)} \tag{5.47}$$

1000 random numbers were generated (from normal distribution) such as 99% of the numbers falls in the range $\pm$ Noise-Level (equation 5.47). The proposed algorithm was then applied for each new triplet of corrected reflectance (i.e. simulated reflectance plus noise). The relative errors in of SPM were then estimated at 99% of confidence i.e. mean relative errors $\pm$ 3 standard deviation (figure 5.10). As we can see from figure (5.10), the effects of random noise on the accuracy of SPM is more pronounced over clear water and increase with aerosol optical thickness. Moreover in the presence

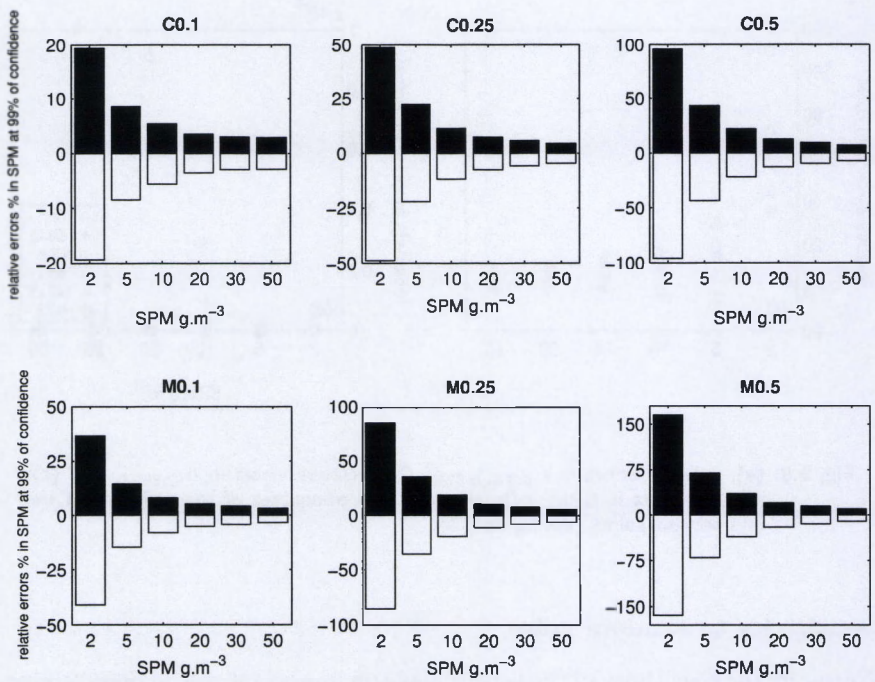

Fig. 5.10: The relative errors % in the retrieved concentrations of SPM at 99% of confidence i.e. mean $\pm$ 3 $\times$ standard deviation.

of maritime aerosol, the estimated concentration SPM is subjected to a wide range of fluctuation in comparison to continental aerosol. These two observations can be physically explained as follows. The unique shape of the turbid water signal at the NIR (0.8-0.87 μm) facilitate separating the total signal to its components (water and aerosol). This task becomes a bit more difficult for large value of aerosol optical thickness. However the peak at 0.8-0.82 of turbid water signal is still sufficient to retrieve the concentrations of SPM within acceptable accuracy ($< 10\%$). On the other hand, clear water signal at the NIR is very similar to that of aerosol reflectance. Therefor any fluctuations in the corrected reflectance will either be assigned to the aerosol or to the water signal and hence increasing the uncertainty about these signals. This uncertainty, in turn, is propagated to the estimated concentration of SPM. The aerosol ratio $\varepsilon_{(s,l)}$ has a steeper slop w.r.t. the optical thickness for continental than for maritime aerosol. The maritime aerosol will therefor be more sensitive to random fluctuation in the data (as it can be seen in figure 5.10).

5.4 Conclusion and remarks

The spatial variability of the aerosol and water signals at the NIR are characteristic features of coastal and turbid waters. This is due to the different aerosol types that may co-exist in this transection zone and to the unique shape of the water signal which can easily be separated from that of the aerosol. Considering and quantifying these variabilities are the key solution for the atmospheric correction and SPM quantification in coastal and turbid waters. In this chapter a coupled approach was proposed to compute the values of the water ratio $\alpha_{(s,l)}$ and the aerosol ratio $\varepsilon_{(s,l)}$ from the corrected reflectance simultaneously (figure 5.11). With a good choice of wavelengths it was shown that the water reflectance ratio is a strong function of SPM concentrations. These wavelengths were defined to reflect the maximum variability in the water reflectance ratio. The first bands was between 0.8 and 0.82 μm and the other two bands were longer than 0.82 μm. Two assumptions were imposed on these NIR bands. First, the water leaving reflectance is optically governed by the SPM and water molecules. Second, the aerosol in the multiple scattering regime follows the same spectral dependency of the single scattering regime. With respect to these assumptions a rigorous solution to the atmospheric-correction problem was constructed. For each triplet of corrected reflectance an exact values of the water and

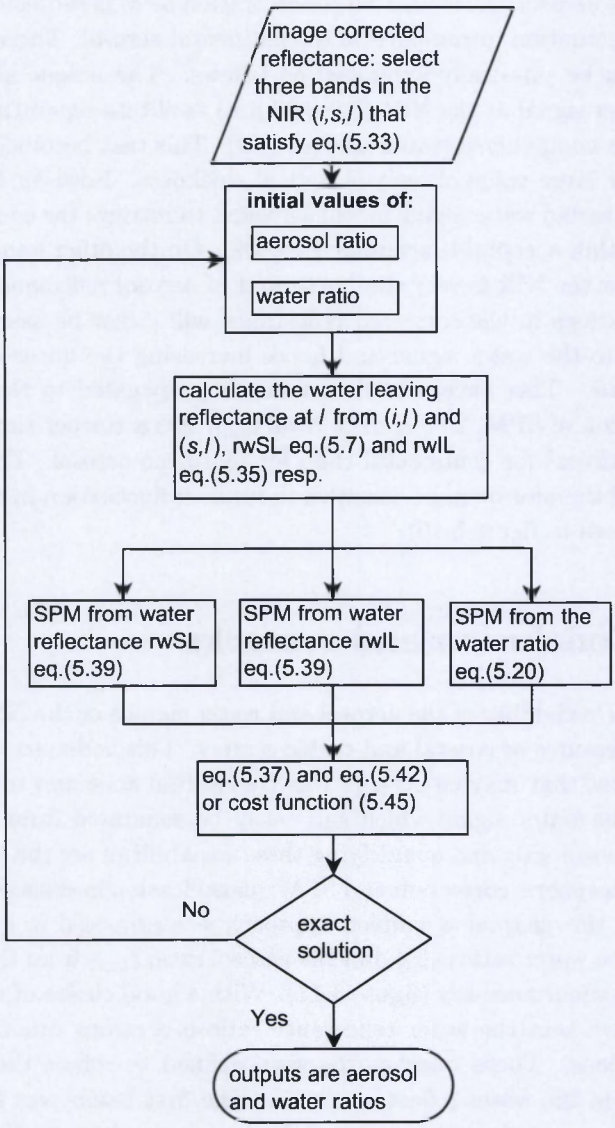

Fig. 5.11: Schematic illustration of the proposed algorithm.

aerosol reflectance ratios were found.

The superiority of the proposed model on the iterative method (that does not employ a cost function) was clearly demonstrated for two aerosol types and water models. The proposed model is limited, however, for turbid water models (i.e. the Gordon-type hydro-optical model; Gordon *et al.*, 1988[9]). For clear water model (i.e. Kirk-type hydro-optical model Kirk 1991[70]) the first component of the proposed method (equation 5.37) also provided an exact solution. The proposed approach is however sensitive to fluctuations in the data. This was more pronounced over Maritime aerosol coupled with clear water and increased with aerosol optical thickness. On the other hand, the unique shape of turbid water signal at the NIR (0.8-0.87 μm) was sufficient to retrieve the concentrations of SPM within acceptable accuracy ($< 10\%$).

5.5 Appendix

5.5.1 Atmosphere-ocean setup

The atmospheric path is generated (following Vermote *et al.*, 1997[45]) for a given viewing-illumination geometry, water and ozone content and different aerosol optical thicknesses (see figure 5.12). The zenith angles were 40° and 30° for the sun and the sensor respectively. The azimuthal angle difference was taking as 30°. The values of water vapor and ozone content were assumed as: h_2o = 2.93 cm, and O_3 = 0.319 cm. The attenuations in the spectra of the atmospheric path (figure 5.12) are due to ozone and oxygen absorption . The water leaving reflectance is modelled (equation 5.16) for varying concentrations of SPM, chlorophyll-a, and DOM (see figure 5.13). We have 36 different combinations for the atmospheric-path and the water leaving reflectance (i.e. pseudo corrected reflectance). The modelled total-reflectances, at the sensor level, are the sum of atmospheric path and water leaving reflectances.

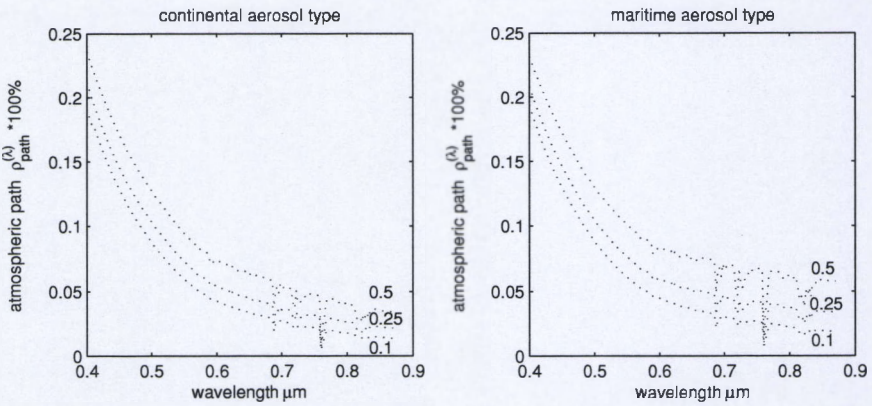

Fig. 5.12: Atmospheric path reflectances at 800 km altitude. Two aerosol types were considered (continental and maritime) and three optical thicknesses 0.1, 0.25 and 0.5. These spectra were generated with the 6S package.

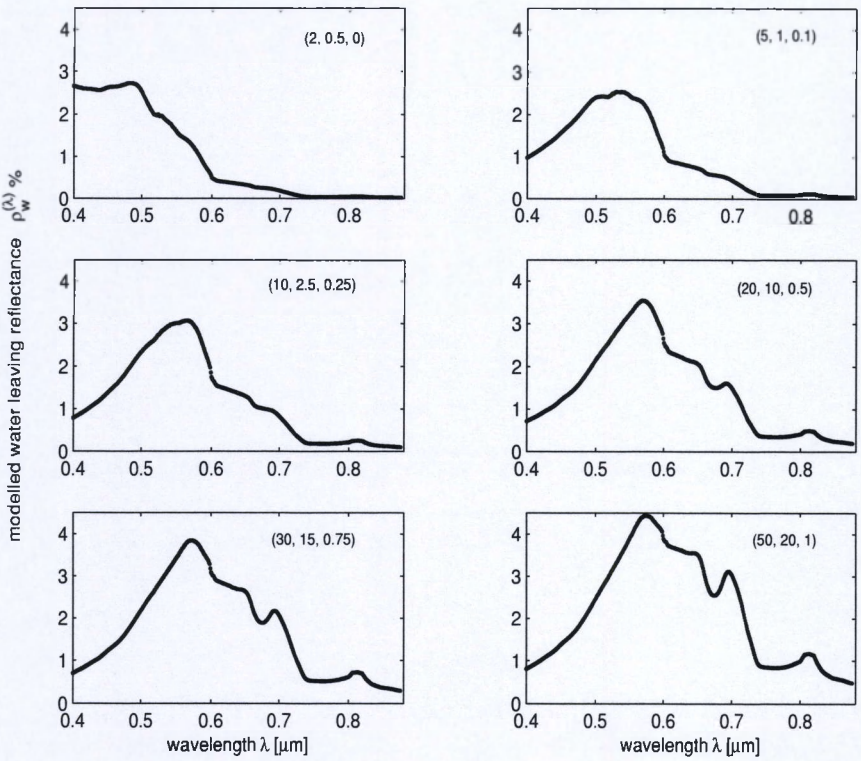

Fig. 5.13: Modelled water leaving reflectances (at the sea-surface) for varying concentrations of SPM and Chl-a and the absorption coefficient (at 0.4 μm) of DOM (the numbers on each panel).

Chapter 6

An inversion method for estimating the IOP from AOP: Simulation

Abstract

The signal leaving the water body can be described as a function of the inherent optical properties (IOP). This forward procedure supplies a unique output (water leaving reflectance) for a given set of IOP and boundary conditions. The idea behind ocean color is to remotely estimate the IOP from the recorded reflectance AOP (apparent optical properties). There are two methods to invert the AOP to the governing IOP. The first is explicit solution which is a one-to-one relationship. Thus the desired IOP are parameterized as a function of one variable. This approach is limited to specific situations (e.g. the water is optically-governed by a purely scattering or absorbing constituent). This can be realized in a controlled conditions, open ocean (case I waters) and at the NIR part of the spectrum. The second method is implicit-solution which solves a sequence of direct problems. The measured reflectance can then be fitted to these pre-generated spectra of water leaving reflectance. Inherent optical properties are retrieved from the modelled-spectrum which has the best-fit to the measurement. In this chapter the surface water model (equation 2.39) is inverted using an implicit technique (i.e. optimization technique). The inversion was verified using pseudo data (twins experiment). The performance of the inversion

was assessed by measuring the errors in the retrieved IOP, the residuals of the cost function, stability to small fluctuations and the rate of convergence.

6.1 Introduction

The knowledge on SPM loads and their spatial distributions and physical properties is essential to maintain navigational routes and to monitor coastal environments being a source or sink of SPM. Moreover these sediments in suspension play an important role in water quality management since it relates the rate of primary production (the rate at which new plant material is reproduced) to heavy metals, micro-pollutants and light attenuation (Vos *et al.*, 1998)[78]. The concentrations of SPM can be estimated either by direct or indirect measurements. Traditional in-situ measurements are the most accurate and reliable set of data. However this type of measurement is time consuming, limited in spatial and temporal coverage and subjected to a substantial variability. These points-based data may involve considerable errors if extrapolated spatially over a large area (Nanu and Robertson 1990)[102]. The data from ocean color sensors provide the best information on the spatial and temporal distribution of SPM. The SPM can be remotely quantified following either the empirical or the analytical approach. The empirical method is based on a statistical relationship between the in-situ measured SPM and the recorded reflectance. The concentrations of SPM are estimated through tuning (using in situ measurements) the parameter(s) of a regression function. Correlation between the SPM and the visible-reflectance of natural water bodies has been observed by many investigators Holyer (1978)[103], Sturm (1980)[58], Stumpf (1988)[104], Lathrop *et al.* (1989)[105], Novo *et al.* (1989)[106], Lathrop *et al.* (1991)[107], Ferrier (1995)[108], Vos *et al.* (1997)[77] and 1998[78], Han and Rundquist (1996)[85], Han (1997)[109], Gao and Oleary (1997)[110], Pozdnyakov *et al.* (1998)[111], Forget and Ouillon (1998)[112], Tolk *et al.* (2000)[84], Kallio *et al.* (2001)[113], Zhang *et al.* (2002)[26] and Doxaran *et al.* (2002)[114]. For a summary on the SPM models being used the reader is refer to Durand *et al.* (1998)[115] and Mukkelsen (2002)[116]. The conclusion of the above referenced studies can be summarized as following:

- The correlations between the SPM and reflectance vary with concentration, wavelength, sediment type, particle size distribution, viewing geometry and the presence of chlorophyll and/or DOM.
- Estimating the values of the fitting coefficients needs large numbers of

in-situ sampling-sites. This is to avoid outlier (e.g. during dredging activities) when extracting the regression parameters.

- The long wavelengths ($\geq$ 0.5 μm) are linearly correlated to the concentration of SPM.
- The range of SPM did not exceed 30 g.m^{-3} except for Lathrop *et al.* (1991)[107] with 100 g.m^{-3} and Doxaran *et al.* (2002)[114] up to 700 g.m^{-3}.
- The accuracy of the retrieved SPM concentration is 30-50%.
- The algorithms have local and seasonal variations. Therefore these algorithms should be calibrated for each site and season (i.e. new regression coefficients).

Analytical methods are either implicit or explicit. Explicit solutions are direct-inversion assuming a one-constituent water model. This method is restricted to case I waters or the NIR part of the spectrum. The NIR bands are very appropriate for SPM quantification in turbid waters. This is due to the following:

- The water column is optically governed by SPM in the NIR. This allows the use of a simple hydro optical model (Gordon *et al.*, 1988)[9] and direct inversion.
- The water-surface reflectance and bottom reflectance have small values (Tolk *et al.*, 2000)[84]. This will reduce the induced error due to roughened sea surface or/and bottom albedo.
- The radiance field is not affected by the stratification of the water column (Forget *et al.*, 2001)[117].
- The coupled term is negligible (Rayleigh contribution is very small (Gordon and Castano 1987)[49]. This allows to introduce some realistic assumptions to facilitate the atmospheric correction.

Implicit solutions are based on minimizing the difference between the modelled and measured radiance (Doeffer *et al.*, 1994[118], Lee *et al.*, 1998[6] and 1999[10], Forget *et al.*, 1999[119] and 2001[117] and Chomko *et al.*, 2003[96]). The water leaving reflectance can be modelled following one of the two approaches. The first uses the radiative transfer (equation 2.36), or its approximation, to simulate the water leaving reflectance. The results of

the inversion are the inherent optical properties of the water. The second approach employs Mie theory to model the scattering and absorption of a light beam by small particles (Twardowski *et al.*, 2001[120] and Gordon and Du 2001[121]). The outputs of Mie-inversion are the index of refraction, scattering efficiency-factors, and a parameter that describes the particle-size distribution function (PSD). These outputs can be up-scaled to the bulk IOP and the associated water-signal of the water column. Forget *et al.* (1999)[119] argued that the index of refraction and the concentration of SPM can not be retrieved from water leaving reflectance. This was due to degeneracy effect between the index of refraction and the concentrations. On the other hand Twardowski *et al.*, (2001)[120] showed that the bulk index of refraction can be retrieved from the backscattering fraction and the hyperbolic slope of the particle-size distribution. This was based on Mie computation and in situ measurements of scattering, backscattering and attenuation coefficients. Risovic (2002)[122] showed that the two-component model was an adequate PSD model for backscattering and scattering calculations. This chapter focuses on developing an implicit inversion method to retrieve the bulk IOP from the water leaving reflectance. The water leaving reflectance is, first, simulated for a set of IOP using the surface water model (equation 2.39). Then an implicit inversion technique is applied on the modelled reflectances to retrieve these IOP.

6.2 Method

The remote sensing reflectance is modelled for sets of IOP using the forward solution (equation 2.39). These spectra are fitted to the measured spectrum. The spectrum with best-fit allocates the sought IOP plus/minus some errors. A good inversion-model will rapidly converge to the actual IOP with small values of errors. Moreover, the solution should be stable for small perturbations in the original data (reflectances). The model can be accepted if the above-mentioned features are satisfied (convergence, stability and small errors). The approach is to design a cost function that measures the agreement between the data (results from atmospheric correction) and the modelled water leaving reflectance. This function can be arranged so that small values represent a close agreement (i.e. least-square minimization). Thus the objective is to minimize the cost function (equation 6.1) in an iterative manner such that the parameters (i.e. IOP) are adjusted to

achieve the minimum:

$$\phi = \sum_{i=1}^{N} \left[\rho_{w,r}^{(\lambda_i)} - \rho_{w,m}^{(\lambda_i)}(\mathbf{iop}) \right]^2 \tag{6.1}$$

Where $\rho_{w,r}^{(\lambda_i)}$ is the recorded water leaving reflectance and $\rho_{w,m}^{(\lambda_i)}(\mathbf{iop})$ is the modelled reflectance as a function of the IOP's vector **iop**. Let us note that equation (6.1) is a spacial case of Chi-square with the assumption of normally distributed errors and a constant standard deviation (see Appendix C). The IOP can be parameterized as a function of their values at the blue-band (section 2.4). The considered IOP are the absorption of DOM $a_{dom}(0.44)$ and phytoplankton pigment $a_{phy}(0.44)$ at 0.44μm and the backscattering coefficient of the SPM $b_{b(spm)}(0.4)$ at 0.4μm. Thus the vector **iop** has three components and can be written as:

$$\mathbf{iop} = \begin{bmatrix} a_{phy}(0.44) \\ a_{dom}(0.44) \\ b_{b(spm)}(0.4) \end{bmatrix} \tag{6.2}$$

The procedure we shall discuss is iterative in nature. Equation (6.1) can be started with initial values of the IOP. In each iteration (j) the values of the IOP are adjusted to decrease the cost function ($\phi_{j+1} < \phi_j$). This is proceeded until the cost function has converged to the minimum. Brief outlines are given in Appendix (C).

6.3 Results and discussions

6.3.1 Pseudo remote sensing reflectances

The water leaving reflectance was modelled from pseudo IOP (see table 6.1). The water leaving reflectance was assumed optically governed by three constituents plus the sea-water molecules. These constituents are phytoplankton pigment (chlorophyll-a), dissolved organic matter (DOM)

chlorophyll-a [mg.m^{-3}]	$a_{dom}(0.44)$ [m^{-1}]	SPM [g.m^{-3}]
5	0	5
10	0.25	15
15	0.75	30

Table 6.1: The used concentrations to generate the 27 water types of figure (6.1).

and suspended particulate matter (SPM). The IOP of a constituent were linearly related to its concentration. This is true if the specific inherent optical property (SIOP) of each constituent is known. Measurements of the SIOP in the North Sea were performed by IVM[11]. These measurements are used and assumed constant. 27 combinations were realized from table (6.1) to generate water leaving spectra using the surface water model (equation 2.39). The resultant water leaving spectra are shown in figure (6.1). The concentrations presented at the right-hand side of figure (6.1) are proportional to the backscattering coefficient. This true for a constant value of the specific backscattering coefficient (see equation 2.30).

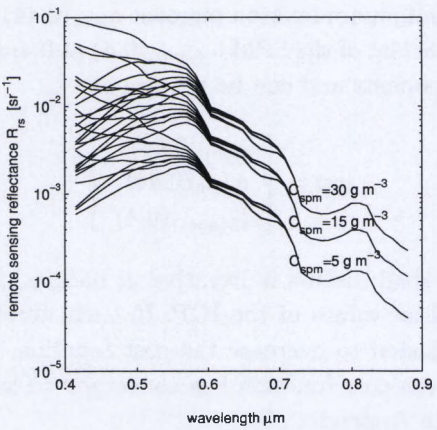

Fig. 6.1: The spectra of the remote sensing reflectance (i.e. $\rho_w^{(\lambda)}/\pi$) modelled from table (6.1).

6.3.2 Initialization

The model has three unknowns, namely $a_{phy}(0.44)$, $a_{dom}(0.44)$ and $b_{b(spm)}(0.4)$. The variables are initialized following Lee *et al.* (1999)[10]:

$$
\begin{aligned}
a_{phy}(0.44) &= 0.072 \left[\frac{\rho_w^{(0.44)}}{\rho_w^{(0.55)}} \right]^{-1.62} \\
a_{dom}(0.44) &= a_{phy}(0.44) \\
b_{b(spm)}^{\backprime}(0.4) &= 30 a_w(0.64) \rho_w^{(0.64)}
\end{aligned}
$$

Where the backscattering coefficient is corrected for viewing-geometry:

$$b_{b(spm)}^{\backprime}(\lambda) = b_{b(spm)}(\lambda)\,[1 + 0.1152 \sin\theta \sin\theta_0] \tag{6.3}$$

The above expression (equation 6.3) is limited to viewing angles $\theta < 30°$ and azimuthal difference $< 90°$. These initial values result in a spectrum which is fitted to the modelled reflectance (figure 6.1) and the sum of squared differences between the two spectra is minimized.

6.3.3 Reliability of the model and its estimates

At the minimum the cost-function ϕ will attain an approximate value of the real minimum ϕ_0 such:

$$\phi \leq \phi_0 + \epsilon \tag{6.4}$$

The error ϵ should be sufficiently small in order to initially accept the model. As previously explained (section 6.3) the function ϕ, at the minimum, is approximated using Taylor series expansion:

$$\phi = \phi_0 + \frac{1}{2}\delta\mathbf{iop}^T\mathbf{H}_0\delta\mathbf{iop} \tag{6.5}$$

Where $\delta\mathbf{iop}$ is the difference between estimated and actual values of IOP (i.e. the errors in IOP) and $\mathbf{H}_0$ is the Hessian matrix at the minimum. From the above two equations (6.4 and 6.5) the difference ϵ at the minimum (i.e. $\mathbf{H}_0$ is positive definite) is approximately:

$$\delta\mathbf{iop}^T\mathbf{H}_0\delta\mathbf{iop} \leq 2\epsilon \tag{6.6}$$

The solution-vector $\mathbf{iop}_0$ is well determined if the difference $\delta\mathbf{iop}$ is small relative to the scale by which the sought parameters are measured. In other words equation (6.6) is satisfied (Bard 1974)[123]. Otherwise (i.e. $\delta\mathbf{iop}$ is large) the vector $\mathbf{iop}_0$ is ill-determined. This is to say that a small variations in the recorded data will results in different solution. Figure (6.2) illustrates the errors (i.e. the vector $\delta\mathbf{iop}$) in the retrieved parameters. This figure shows that the errors in the retrieved IOPs are within 10^{-4} m^{-1}. Moreover the residuals in the estimated reflectance (lower panel at the right corner) are within 10^{-4} %. The residuals measure the departure of model-predictions from the simulated water leaving reflectance. The parameter ϵ was approximated as being the root mean square of the residuals (RMS). Equation (6.6) was then used for the RMS of residuals for each

water types. The RMS of residuals, in all water types, satisfied equation (6.6). In other words the solution is well determined for the mean of maximum errors in the water leaving reflectance. It might be more efficient to study the relative departure (i.e. relative error) of the solution from the real values. This is because the values of relative errors in the IOP are equal to that in the retrieved concentrations. The relative errors in the estimated parameters are quantified in figure (6.3) for each water type. Two important observations can be drawn from figure (6.3). The first is that the model is very appropriate for SPM. The retrieved values of $b_{b(spm)}(0.4)$ are very accurate with a maximum relative error less than 0.02%. This value (of 0.02%) decreases with increasing SPM concentrations to reach maximum value less than 0.005% at 30 g.m^{-3} of SPM. The second observation is that the relative-error in $a_{phy}(0.44)$ increases with increasing the concentrations of DOM. This is more pronounced at low concentrations of chlorophyll-a and SPM. On the other hand the relative-error of $a_{dom}(0.44)$ increases with

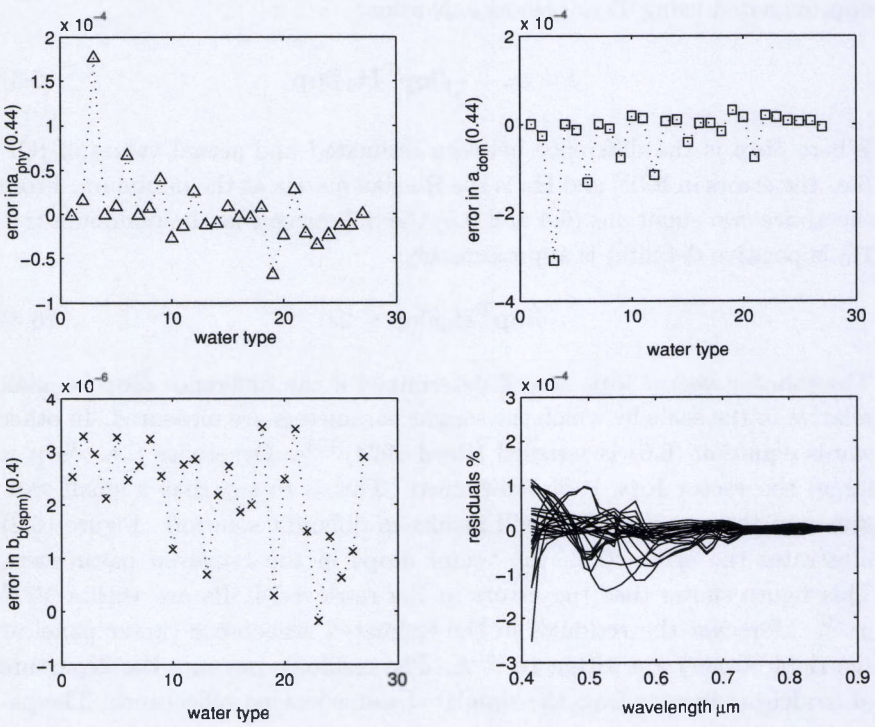

Fig. 6.2: The errors in the estimated IOP for the 27 water types.

increasing DOM concentrations and decreasing the concentrations of SPM and chlorophyll-a. In general the concentrations of chlorophyll-a are overestimated in waters with low concentrations of DOM and underestimated in waters with high concentrations of DOM. The sensitivity of the chlorophyll-a to the abundance of DOM could be due to a degeneracy effect of the inversion. This might explain why case II waters with high concentrations of DOM ($a_{dom}(0.044) \geq 0.25$) were avoided in most coastal studies by assuming a small constant value of $a_{dom}(0.044)$ (Tassan 1988)[124]. Let us note that the spectral-slop of DOM absorption can also be retrieved through the inversion. Nevertheless this will increase the degrees of freedom and hence the degeneracy of the solution. However the algorithm (as it was presented) succeeded in reproducing very good estimates of the IOPs. The relative errors were less than 0.05% in $a_{dom}(0.44)$, less than 0.018% in $b_{b(spm)}(0.4)$ and less than 1.8% in $a_{phy}(0.44)$.

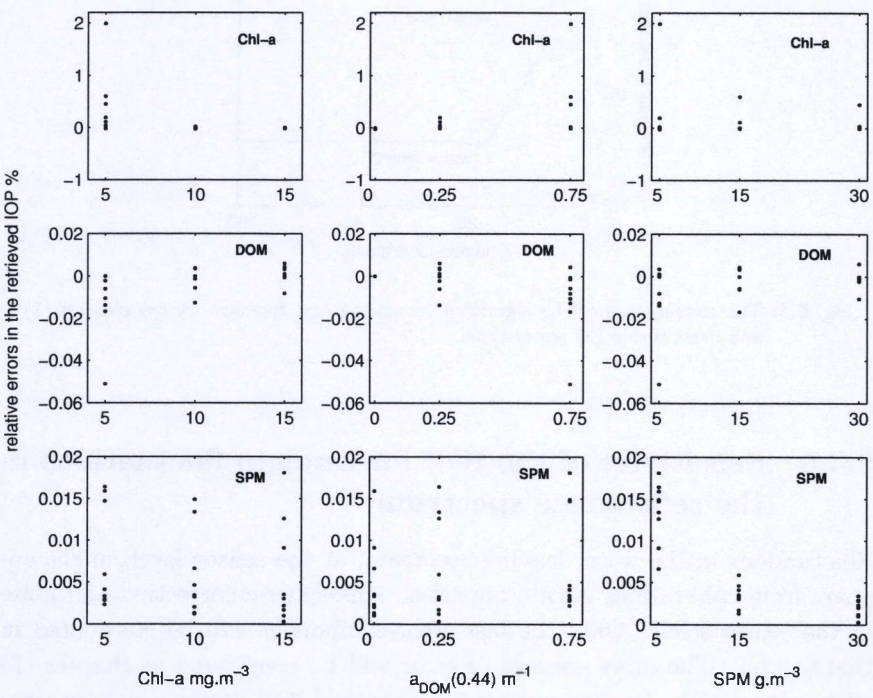

Fig. 6.3: The relative errors in the estimated parameters as functions of the actual concentrations of table (6.1).

6.3.4 Convergence and stability

A practical issue is the rate of convergence of the model to the solution. In other words the number of iterations has to be relatively small. The number of iterations did not exceed 20 for the turbid water type to reach a residual of 10^{-7} in the cost function (figure 6.4). On the other hand the number of needed iterations for clear water type increased to 50 iterations. This can be explained by the fact that in turbid waters small variations on the IOP has no significant impact on the resulting water leaving reflectance. Therefore the change in the initial IOP vector (i.e. the step) is relatively larger for turbid water than that for clear water. Thus the number of needed iterations will be less in turbid water than in clear water.

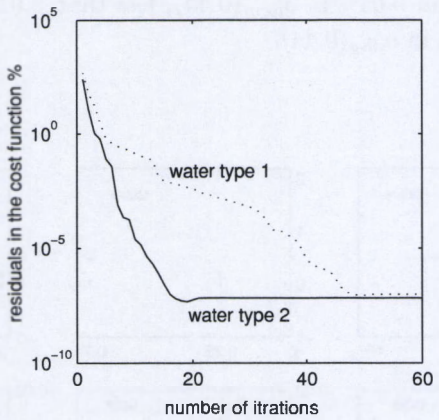

Fig. 6.4: The convergence of the algorithm versus the cost function for the clearest (1) and most turbid (2) water type.

6.3.5 Sensitivity of the IOP for random fluctuations in the reflectance spectrum

Fluctuations in the water leaving spectrum, at the sensor level, might appears from calibrations errors, imperfect atmospheric correction and noise in the sensor itself. Only the last error-component will be considered in this section. The other sources of error will be considered in chapter (7) with more details. In consequence the extracted IOP vector is not the only possible solution vector, although it is the best one. Rather, there are many other IOP vectors each of which could have given a different set of relative

errors (e.g. figure 6.3). The deviation of these relative errors (resulting from fluctuations in the reflectance spectrum) from the minimum relative errors (when no fluctuation was considered) is the quantitative measure of sensitivity. This sensitivity-measure defines the variation of the retrieved IOP to small fluctuations in the water leaving reflectance.

The fluctuations were randomly generated at each wavelength using the normal probability distribution. The standard deviation was taking as being spectrally independent and vary with the residuals only. Its value was calculated from variance of the residuals which was estimated as (Brad 1974)[123]:

$$\sigma = \sqrt{\frac{1}{N-m}\sum_{i=1}^{N} e_i^2} \tag{6.7}$$

Where (N-m) is the degree of freedom which is given by the number of bands (N) minus the number of unknowns (m). The term e_i is the residual between simulated and fitted water leaving spectrum at a band i. Due to the small values of σ (e.g. figure 6.2, the lower right panel), the resulting values from equation (6.7) were multiplied by a constant factor (100). This factor can be anything else than 100, however we shall accept it as long as the resulting water leaving spectra (with fluctuations) have positive values along the spectrum. The detailed discussion of a standard deviation that is spectrally dependent or independent is left for the next chapter. First the residuals of the best fits (figure 6.2, the lower right panel) were used in equation (6.7). Then a random numbers were drawn (for each water type) from a normally distributed probability function with a zero mean and a standard deviation equal to 100 $\times\sigma$. These randomly generated numbers (simulated fluctuations) were added to the water leaving spectra (figure 6.1). The residuals of these new fluctuated spectra were again used to calculate new values of standard deviation. In other words the residuals of each randomly generated spectrum are used (in equation 6.7) to generate a new fluctuated spectrum. This is to assign a random nature to the standard deviation that is related to the water leaving spectrum (through the residuals), rather than employing a constant value. This adaptive-value of the standard deviation enable to simulate a larger range of fluctuations (figure 6.5). Figure (6.5(a)) shows that the values of σ (i.e. residuals) increased dramatically with the first perturbation on the best fit spectrum. The resulting 1000 (random spectra) $\times$ 27 (water types) fluctuations relative to the actual spectra of (figure 6.1) are illustrated in figure (6.5(b)). The relative fluctuation is defined as being the spectral-ratio (i.e. per wavelength) of the random value

(i.e. fluctuation) to the value of the water leaving reflectance. From figure (6.5(b)) we can see that the large values of fluctuations appears in three spectral regions, namely the blue, the red absorption bands of DOM and chlorophyll-a and the NIR part of the spectrum. This means that the residuals (i.e. errors) between the best fit and simulated spectra are expected to be large at these spectral regions. Let us note that these regions are, practically, the most vulnerable spectral ranges for fluctuations due to imperfect atmospheric correction and sensor noise.

The inversion method might fail in predicting the blue and the red absorption bands of DOM and chlorophyll-a. This is because the spectral slope of the DOM was assumed constant (equation 2.33). Moreover the variation of the chlorophyll-a absorption coefficient with phytoplankton species was not modelled in equation (2.35). Let us note that the inversion will only be able to separate the absorption of chlorophyll-a from that of DOM at the blue and the red bands (centered at 0.44 μm and 0.675 μm respectively). Fluctuation in these two bands, will therefore, result in degenerated concentrations of chlorophyll-a and DOM. On the other hand the resulting concentrations of SPM are expected to be biased proportional to the residuals at the NIR.

Each one of the fluctuated water spectra (i.e. fluctuation of figure 6.5(b) plus the spectra of figure 6.1) was inverted to the governing IOP following the aforementioned approach (section 6.2 with the initialization in section

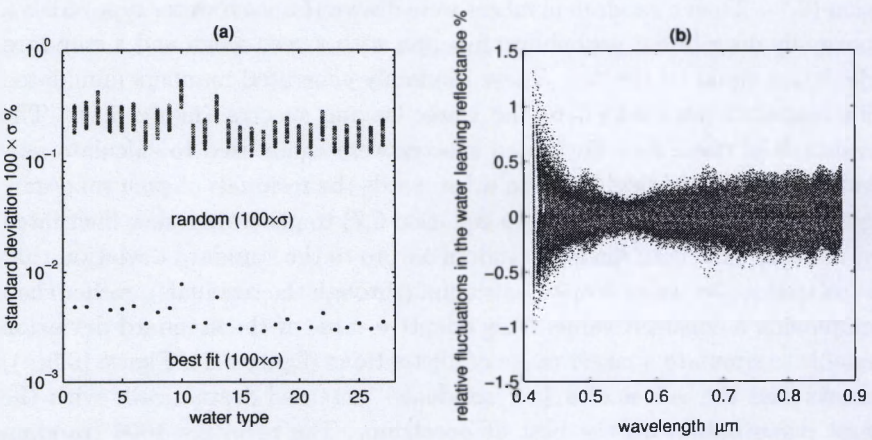

Fig. 6.5: (a): the adaptive-standard deviations (calculated from 6.7) for 1000 realizations for each spectrum in figure (6.1). (b): the relative fluctuations resulting form normally distributed probability function with adaptive-standard deviations.

6.3.2). The relative errors of these IOP (resulting from the fluctuated spectra) are calculated and assumed to follow the same shape as the probability distribution of the fluctuations (i.e. normally distributed). The means (three for each water type) of these relative errors are expected to be close to zero. Let us note that they were generated with a normally distributed probability function. More importantly is the standard deviations of these relative errors (figure 6.6) which is the quantitative measure of the sensitivity. This is the deviation of the IOP with respect to the fluctuations in the water leaving spectrum. The general observation (from figure 6.6) is that the 100 $\times\sigma$ fluctuations increased the relative error in the IOP about an order of magnitude (compare to figure 6.3) with the same trend however. The accuracy of the retrieved Chl-a, DOM and SPM concentrations increased with increasing the concentrations of SPM. This trend was inverted for DOM. i.e. the accuracy of the IOP decreased with DOM abundance.

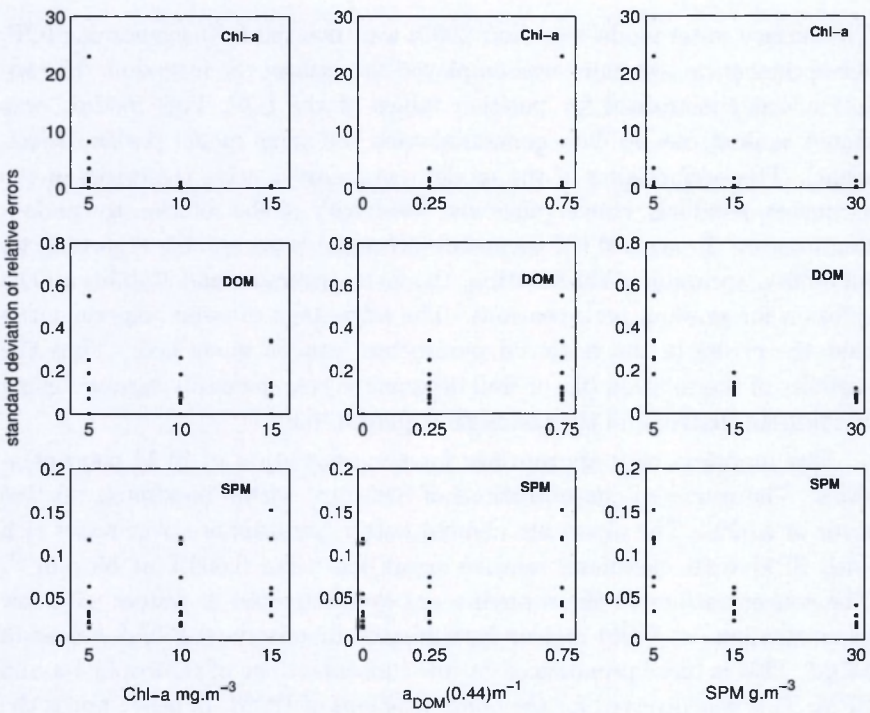

Fig. 6.6: The standard deviations of the relative errors in the IOP (retrieved form 1000 fluctuated spectra) as function of the actual concentrations of table (6.1) subjected to fluctuations.

For DOM free water, the relative errors in the estimated concentrations of Chl-a and SPM increased over clear waters. It appears from figure (6.6) that the absorption coefficient of chlorophyll-a is the most sensitive parameter to the random fluctuations in the water leaving reflectance. This is true if DOM is presented in the water. In this case, the retrieved concentrations of chlorophyll-a have 65% probability to be within $\pm$ 23% off the true values. For DOM-free water this uncertainty in the retrieved concentrations of chlorophyll-a is reduced to less than 0.2% for the same probability of occurrence. These conclusions are corrected with respect to the associated range of spectral fluctuations (figure 6.5(b)). The range of the fluctuation at the blue ($\pm$1%) is two folds larger than the allowed error (0.1-0.5%) in the water leaving reflectance at this band (Gordon 1997)[42].

6.4 Conclusion and remarks

The surface water model equation (2.39) was inverted to the governing IOP. An optimization technique was employed to perform the inversion. The solution was constrained for positive values of the IOP. This method was tested against pseudo data generated with the same model (twins experiment). The performance of the model was assessed using the errors in the estimates, residuals, convergence and sensitivity of the solution to random fluctuations. In general the inversion technique is acceptable regarding its reliability, accuracy of the solution, the fast conversion and stability of the solution for random perturbations. The advantage of twins experiment is that the errors in the retrieved parameters can be quantified. Thus the stability of the solution (ill- or well determined) can be easily assessed using the hessian matrix and the residuals (equation 6.6).

The model is very appropriate for the estimation of SPM concentrations. The retrieved concentrations of SPM are within maximum relative error of 0.02%. The algorithm showed better performance over water rich with SPM with maximum relative errors less than 0.005% at 30 g.m^{-3}. The concentrations of chlorophyll-a are overestimated in waters with low concentrations of DOM and underestimated in waters with high values of DOM. This is more pronounced at low concentrations of chlorophyll-a and SPM. This was inverted for the concentrations of DOM. In other words the relative errors in DOM increased with increasing DOM concentrations and decreasing the concentrations of SPM and chlorophyll-a. The algorithm succeeded in reproducing very good estimates of the IOP. The accuracy of

the IOP is improved when retrieved from water with high concentrations of chlorophyll-a and SPM and free of DOM. The relative errors in the concentrations were less than 2% in chlorophyll -a, 0.05% in DOM and 0.02% in SPM. The simulated water leaving spectra were then subjected to random fluctuations. These fluctuation were generated with normally distributed probability function having a zero mean and an adaptive-standard deviation. The residuals of a randomly generated spectra were used to adapt the value of the standard deviation to generate the very next fluctuated spectrum. This adaptive-value of the standard deviation enabled the algorithm to construct realistic fluctuations spectra.

Each one of the fluctuated water spectra was inverted to the governing IOP. The standard deviation of the relative errors in these IOP sets was used to assess the sensitivity of the IOP to fluctuations in the water spectrum. The absorption coefficient of chlorophyll-a was found to be the most sensitive parameter to the random fluctuations in the water leaving reflectance. In case of DOM laden water, the retrieved concentrations of chlorophyll-a have 65% probability of being within $\pm$ 23% off the true values. For DOM-free water this uncertainty was reduced to less than 0.2% for the same probability of occurrence. These conclusions are with respect to the associated range of spectral fluctuations $\pm 1\%$ at the blue to ± 0.5 at the NIR. Let us note that these results are superior to the required-accuracy which is 35% (Fargion and Muller 2000)[23].

Chapter 7

Stochastic technique to estimate the uncertainty bound on the IOP

Abstract

A stochastic approach was developed that used the residuals between model predictions and measured spectrum to construct a 95% confidence interval around the modelled reflectance. The width of the confidence interval was then used to quantify the sensitivity of the IOP to fluctuations in the recorded reflectance. In turn, these fluctuations were separated according to two perturbation sources, namely imperfect atmospheric correction and sensor noise. A sensitivity analysis on the IOP was then performed to evaluate relative contribution of each perturbation component to the total error-budget of the IOP. In general, the errors in the estimated concentrations of SPM are aerosol dominant while the uncertainty on the retrieved concentrations of chlorophyll-a and DOM is governed by sensor noise.

The algorithm was proposed for hyperspectral sensors with large number of spectral bands. However it was validated with both hyperspectral and multi-spectral data sets.

7.1 Introduction

Due to the stochastic nature of the measurement and the correction (i.e. atmospheric correction) errors, the retrieved water leaving reflectance is not the only possible spectrum. Instead, there are many other spectra (we call them hypothetical spectra) of the water leaving reflectance. Each one of these hypothetical spectra, has the same probability of being the measured water leaving spectrum. Therefore a different set of the IOP would have resulted if a hypothetical spectrum had been realized. In consequence, the hypothetical-IOPs (i.e. resulting from inverting the hypothetical spectra) will have a certain probability distribution from which the solution vector $\mathbf{iop}_0$ was drawn. Equivalently the difference between the solution vector $\mathbf{iop}_0$ (our first estimates) and the true IOP is one member drawn from the probability distribution of the differences between the hypothetical-IOP and the true IOP. This distribution (of the differences) provides all the necessary information about the quantitative uncertainties in the solution vector $\mathbf{iop}_0$.

The objective of this chapter is to compute this distribution and evaluate the relative contribution of each perturbation-component to the total error of IOPs. This is done by separating the influence of these fluctuations on the retrieved IOPs. This will provides us with the necessary tool to quantify the sensitivity and the uncertainties of the IOP to fluctuations in the recorded spectrum. The quality of the water leaving spectrum in retrieving the concentrations of the SPM, chlorophyll-a and DOM can therefore be assessed.

7.2 Method

7.2.1 Separating the perturbation components

Description of the algorithm

Fluctuations in the water leaving spectrum, at the sensor level, can be modelled as bing due to noise in the sensor itself and imperfect atmospheric correction. Each one of these perturbations has its own contribution to the total error-budget on the IOPs. The sensitivity of the IOPs to each sort of these fluctuations can therefore be quantified separately. This is by generating random spectra of water leaving reflectance within a specific interval. The basic idea is to synthesize (i.e. simulate) the hypothetical spectra in a random fashion. Each spectrum, of these random spectra, has

to be physically realistic and within a region of possible spectra. In other words the synthetic-spectra has to be generated within a region around the measured spectrum. The width of this region is adjusted such as to make the distinction between the fluctuations in a spectrum (say n) and the very next spectra (say n-1 and n+1). From each synthetic-spectrum a specific

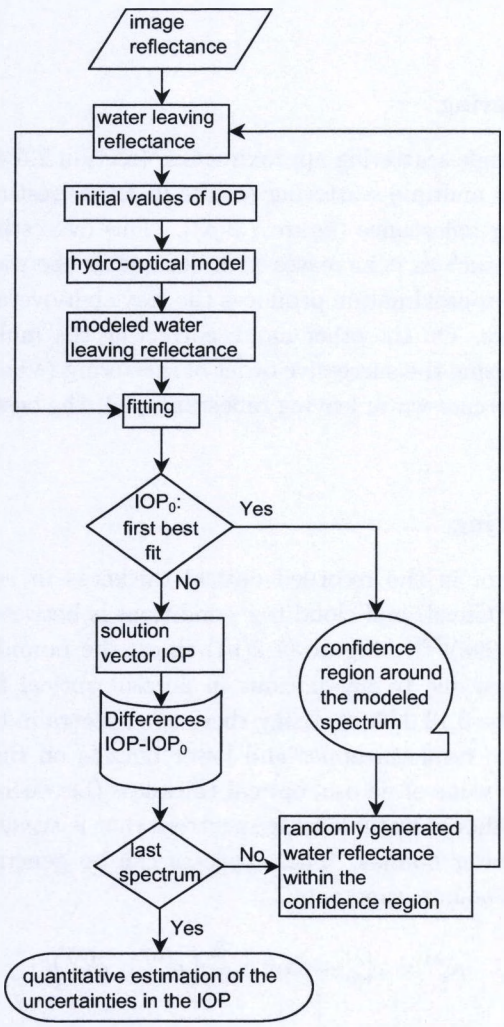

Fig. 7.1: Schematic description of the algorithm.

set of the synthetic-IOP ($\mathbf{iop}^n_{syn}$) can, then, be estimated. The shape of the probability distribution of the difference ($\mathbf{iop}^n_{syn}$ - $\mathbf{iop}_0$) is assumed to be the same as the shape of the probability distribution $\mathbf{iop}_0$ - $\mathbf{iop}_{true}$. This means that the solution vector $\mathbf{iop}_0$ serves as a surrogate to the real values $\mathbf{iop}_{true}$ in the shape of the probability distribution of the differences. Figure (7.1) schematically summarize the aforementioned steps to realize our objective which is the quantitative estimation of the uncertainties on the IOP.

Rayleigh scattering

The use of the single scattering approximation (section 2.5.4) to correct for the air molecules multiple-scattering results in an overestimated values of the water leaving reflectance (figure 7.2(a)). This overestimation is spectrally dependent such as it increases with decreasing the wavelengths. The single scattering approximation produces the Rayleigh-overestimated water leaving reflectance. On the other hand, correcting the multiple-scattering of air molecules using the successive order of scattering (Van Hulst 1981)[27] produces our *reference* water leaving reflectance; i.e. the best possible water leaving spectrum.

Aerosol scattering

The absolute error in the recorded optical thickness in newly calibrated sun-photometer (Cimel) and cloud free conditions is between 0.01 and 0.02 (Holben *et al.*, 1998)[125]. Figure (7.2(b)) shows the bounds on the atmospheric reflectance due to fluctuations in aerosol optical thickness which was assumed to be 0.13 ± 0.02. Using these two spectra in the atmospheric correction scheme result in upper and lower bounds on the water leaving reflectance. Any value of aerosol optical thickness (between 0.11 and 0.15) will result in a different water leaving spectrum that is situated between the upper and the lower bounds. These spectra can be generated within the upper and lower bounds randomly:

$$\rho_w^{(\lambda)} = \rho_{w0}^{(\lambda)} + Ran \times \frac{1}{2}\left(\rho_U^{(\lambda)} - \rho_L^{(\lambda)}\right) \tag{7.1}$$

Where: $\rho_{w0}^{(\lambda)}$ is our best fit estimate using the recorded value of the aerosol optical thickness; $\rho_L^{(\lambda)}$ and $\rho_U^{(\lambda)}$ are the lower and the upper bounds of the water leaving spectra respectively. These two bounds can be obtained using

the two values of aerosol optical thickness (i.e. 0.11 and 0.15) respectively. The random number *Ran* can be generated following the normal distribution such that 95% of the numbers falls between ± 1. Let us note that the choice of normal distribution is just to be in consistence with the least square approximation which assumes a normally distributed residuals (see appendix C).

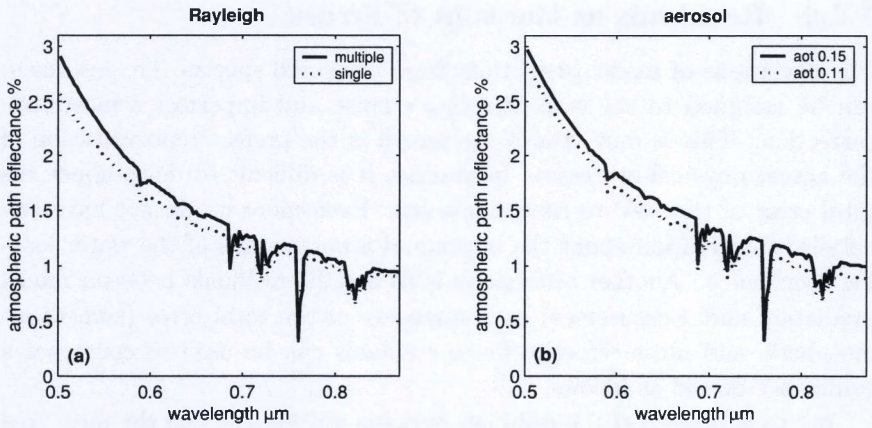

Fig. 7.2: Fluctuation in the atmospheric path reflectance due to (a): single/ multiple Rayleigh scattering and (b): different aerosol optical thickness 0.11 and 0.15. The sun zenith angle is 40°; the sensor is at nadir with zero azimuthal-difference and 4km altitude.

Random noise

The noise equivalent radiance (NER) of a sensor is less than a certain value say NER. Random numbers can be generated between $\pm$ NER at each wavelength independently (i.e. independent of wavelength) such as:

$$Ran\,(0, a \times NER) \tag{7.2}$$

The random noise is assumed to follow the normal distribution with zero mean and $a\times$ NER standard deviation. Let us note that the value of the constant a depends on sensor specifications.

The relative contribution

Normally we will have a total sum of all perturbations due to fluctuations in Rayleigh/aerosol correction and sensor noise. The relative contributions

of each fluctuation-source (rv_i of noise or atmosphere) to the total errors on the IOP can be calculated as being the ratio of the each variance component to the total sum of variances:

$$rv_i = \frac{\sigma_i^2}{\sum_i^N \sigma_i^2} \tag{7.3}$$

7.2.2 Residuals as the sum of errors

The deviations of model predictions from measured spectra (i.e. residuals) can be assigned to the sum of sensor's noise and imperfect atmospheric correction. This is only true if the model is the prefect representation of the actual physical-processes. In practice it is difficult to de-compose the total error of the IOP to its components. Even-more we do not have any detailed information about the upper and lower bounds of the water leaving reflectance. Another alternative is to use the residuals between model prediction and measurement as a surrogate of the total error (sum of atmospheric and noise errors). These residuals can be used to construct a confidence bound as follows.

Let us assume that the residuals between our best fit and the measured spectrum (using the technique of chapter 6) are normally distributed. The variance of the residuals can then be estimated as (Brad 1974)[123]:

$$\sigma^2 = \frac{1}{N-m} \sum_{i=1}^{N} e_i^2 \tag{7.4}$$

Where (N-m) is the degree of freedom which is given by the number of bands (N) minus the number of unknowns (m). The term e_i is the residual between measured and predicted water leaving reflectance at a band i. A (1-α) confidence interval $\rho_{w\pm 0}^{(\lambda)}$ for the model's best fit $\rho_{w0}^{(\lambda)}$ can then be approximated as (Bates and Watts 1988)[126]:

$$\rho_{w\pm 0}^{(\lambda)} = \pm\sigma \left\| \frac{\Delta\rho_{w,m0}^{(\lambda)}}{\Delta \mathbf{iop}_0} \mathbf{R}^{-1} \right\| t(N-m, \alpha/2) \tag{7.5}$$

Where $t(N-m, \alpha/2)$ is the upper quantile for a Student's t distribution with $N-m$ degrees of freedom. The matrix $\mathbf{R}$ is the upper triangle matrix resulting from the the QR decomposition of the the jacobian matrix of the cost function at the minimum (see chapter 6 and appendix C). The first term on the right hand side of in equation (7.5) is the derivative of the

model prediction that has the best fit to the measurement. The derivation of the confidence interval (equation 7.5) will take us out of the scope of this study. For more details consult (Bates and Watts 1988)[126]. We will use this approach relying on the fact that the recorded spectrum of a water type should, in principle, be close to model prediction. In other words, the fluctuations in the measured reflectance should occur within a region that is related to model prediction (i.e. residuals). These residuals can therefore be assigned to the different perturbation-sources on sensor readings. Let us note that to get good results from equations (7.4) and (7.5) the number of bands should be larger than the number of the sought IOP. This approach is therefore valid for large number of spectral bands, thus mainly narrowing the dependency of the confidence interval to the residuals between model predictions and measurements.

7.3 Results and discussion

7.3.1 The DAIS sensor

Introduction

On the 25th of June 2001 the Digital Airborne Imaging Spectrometer (DAIS, see specifications 7.5.1) acquired sets of images that covered part of the Belgian coast. The acquisition was concurrent with radiometric and biophysical in-situ measurements. The images were atmospherically corrected using measurements from the sun-photometer at Oostende. This water-region exhibits a permanent high load of suspended matter reaching 40 $g.m^{-3}$ off the coast and may increase (especially in the winter off Oostende) to more than 100 $g.m^{-3}$ (Eisma and Kalf 1979)[18]. This high load of suspended sediment arises from transport and re-suspension of sediment materials through hydrodynamic processes, from river discharge and from the nearly continuous dredging activities in the area.

Processing steps

The processing of a DAIS image was subdivided into three steps namely, preprocessing, processing and postprocessing. The objective of the first step was to retrieve high accuracy water leaving reflectance. This was realized through a good design of the flight lines (demonstrated in section 7.5.2), accurate in-situ measurements (section 7.5.3) and a reliable algorithm for

atmospheric correction. The total recorded reflectance at DAIS level was atmospherically corrected using data of the sun-photometer at Oostende site (see section 7.5.4). In the processing step, the inherent optical properties of the water were estimated from hyperspectral images. This encompassed two subtasks. The first subtask was to retrieve the IOP of the surface water using the approach of chapter (6). In the second subtask, a stochastic approach is developed to estimate the bounds of relative-uncertainty around the retrieved IOP which is equal to that around the associated concentrations. The post-processing step was to validate the results of the pre-processing and processing steps independently. Since the main objective of this chapter falls in the processing and postprocessing steps the pre-processing section was appended to the main body of the chapter.

7.3.2 Retrieving the IOP from DAIS reflectance

The technique developed in chapter (6) was applied to retrieve the IOP of the water column from the associated reflectance. The solution was bounded to allow zero or positive values of the estimated IOP only. The retrieved

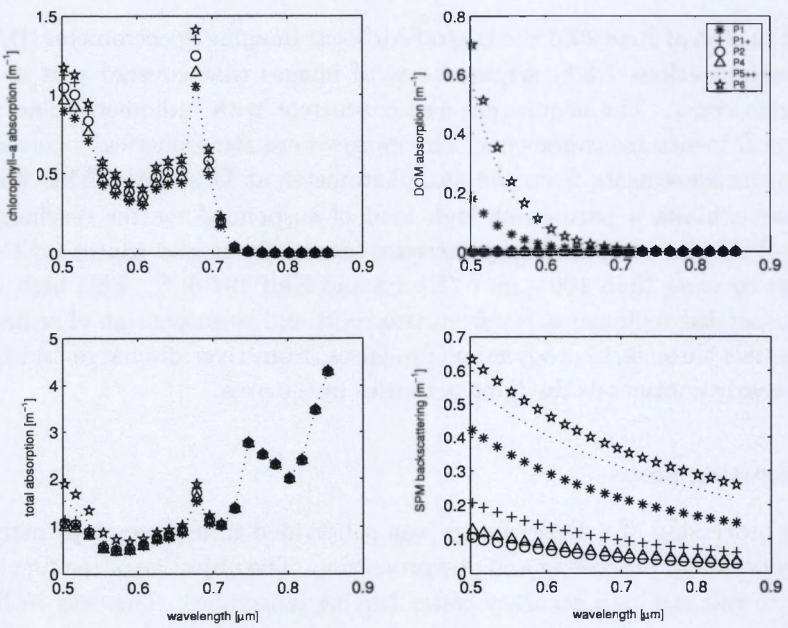

Fig. 7.3: The retrieved inherent optical properties of the water surface layer.

IOP are illustrated in figure (7.3). Figure (7.3) shows that the scattering coefficients of SPM and absorption coefficients of chlorophyll-a and DOM are relatively large (note that sites P1+,P2 and P4 are DOM-free). This is better illustrated in table (7.1). The concentrations in this table were calculated from the retrieved IOP (figure 7.3) and the measured SIOP (IVM data 2000[11]). The estimated concentration of SPM (table 7.1) are not even close to the measured values (table 7.7). This might be due to the large values of reflectance at the NIR (due to sensor's artifacts; Peter Gege 2003, personal communication) that were interpreted (by the model) as high concentrations of SPM. Then to compensate the resulting high signals at shorter wavelengths the model predicted high concentrations of chlorophyll-a and DOM. Let us note that the inversion will only be able to separate the absorption of chlorophyll-a from that of DOM at the blue and the red bands (centered at 0.44 μm and 0.675 μm respectively). However, the spectral range of DAIS (see specifications 7.5.1) do not cover the blue region ($<$ 0.502 μm). The governing parameter in determining the concentration of chlorophyll-a is therefore the red absorption band at 0.675 μm. Any fluctuation in this band will result in degenerated concentrations of chlorophyll-a and DOM (see section 6.3.5).

site	Chl-a mg.m^{-3}	$a_{dom}(0.44)$ m^{-1}	SPM g.m^{-3}
P1	56.72	0.67	173.56
P1+	71.61	0.00	97.29
P2	68.08	0.00	51.32
P4	59.94	0.00	60.54
P5++	64.16	2.80	242.28
P6	68.37	2.43	239.94

Table 7.1: The retrieved concentrations of SPM and chlorophyll-a and the absorption coefficient of DOM from DAIS spectra.

7.3.3 The sensitivity of the IOP to different fluctuations

Rayleigh

The relative errors between the retrieved IOP from the reference spectrum and that retrieved from the Rayleigh-overestimated spectrum are quantified in table (7.2). Table (7.2) shows that the overestimation of the water leaving reflectance due to the used Rayleigh single scattering approximation was interpreted by the model as low value of the chlorophyll-a and DOM absorption. However, the concentrations of chlorophyll-a were underestimated

at the DOM-free sites only (P1+, P2 and P4). When DOM was presented (as predicted by the model) the concentrations of chlorophyll-a were overestimated. This is because the resulting concentrations of chlorophyll-a and DOM are degenerated (see sections 6.3.3, 6.3.5 and 7.3.2).

site	The relative errors % on the IOP due to Rayleigh component		
	$a_{phy}(0.44)$	$a_{dom}(0.44)$	$b_{b(spm)}(0.4)$
P1	0.27	-40.84	2.81
P1+	-4.89	*	1.98
P2	-7.01	*	1.96
P4	-6.12	*	1.82
P5++	0.36	-16.98	2.36
P6	0.329	-19.62	2.32

Table 7.2: The relative errors between the retrieved IOP from the reference spectrum and that retrieved from the Rayleigh-overestimated spectrum. The stars indicate that the model predicted zero values.

Aerosol

1000 spectra were generated between the upper and the lower bounds (resulted from figure 7.2(b)) of the water leaving reflectance. The IOP's were then estimated form the randomly generated spectra. The relative deviation of these IOP's from our solution vector was quantified at 95% of confidence (two standard deviations of the relative difference) in table (7.3).

site	Relative errors due to aerosol with 95% of confidence		
	$a_{phy}(0.44)$	$a_{dom}(0.44)$	$b_{b(spm)}(0.4)$
P1	$\pm$ 1.06	$\pm$ 3.63	$\pm$ 2.51
P1+	$\pm$ 1.30	*	$\pm$ 3.30
P2	$\pm$ 3.37	*	$\pm$ 5.57
P4	$\pm$ 2.49	*	$\pm$ 4.31
P5++	$\pm$ 0.53	$\pm$ 0.86	$\pm$ 1.91
P6	$\pm$ 0.52	$\pm$ 0.98	$\pm$ 1.92

Table 7.3: Relative errors, due to fluctuations in aerosol optical thickness, at 95% of confidence after 1000 iterations.

Noise

Table (7.4) shows the 95% of confidence on the estimated IOP from noise-fluctuated water leaving reflectances. The noise equivalent radiance (NER) of DAIS sensor is less than $\pm 0.25\ Wsr^{-1}m^{-2}\mu m^{-1}$ in the visible and NIR part of the spectrum. This NER was converted to reflectance in figure (7.4). 1000 random numbers were generated with 95% probability to be

between -0.25 and 0.25. These numbers were generated at each wavelength independently (i.e. independent of wavelength), such as in (equation 7.2). The random noise was assumed to follow the normal distribution with zero mean and 0.5 × NER standard deviations (Peter Strobol 2003, personal communications).

site	Relative errors due to noise with 95% of confidence		
	$a_{phy}(0.44)$	$a_{dom}(0.44)$	$b_{b(spm)}(0.4)$
P1	± 2.56	± 13.03	± 1.28
P1+	± 1.84	*	± 1.59
P2	± 3.77	*	± 3.21
P4	± 2.99	*	± 2.46
P5++	± 2.26	± 4.04	± 1.06
P6	± 2.23	± 4.70	± 1.09

Table 7.4: The upper and the lower bound of the relative errors due to noise within 95% accuracy interval after 1000 iterations. The stars indicate that the model predicted zero values.

Tables (7.3) and (7.4) have a common feature that is the relative errors increase with decreasing turbidity of the water. This trend is also seen in table (7.2) for DOM and chlorophyll-a.

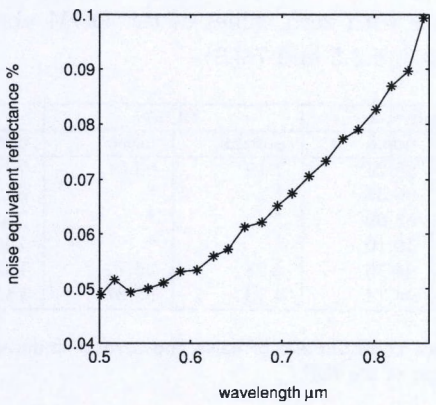

Fig. 7.4: The half width of the noise equivalent reflectance (%) of the DAIS sensor.

The relative contribution

The use of the single scattering theory to approximate the Rayleigh scattering reflectance is a major source of errors in the retrieved IOP (table 7.2).

In this exercise it was assumed that the Rayleigh reflectance is either corrected using single or multiple scattering computations. In other words, the errors due to the used Rayleigh correction scheme have a deterministic nature. Therefor, using a perfect correction scheme of the Rayleigh scattering, leaves the aerosol and noise induced errors to be the major stochastic contributors to the error budget of the IOP. Let us note that calibration errors was not considers due to the lake of information about their magnitude.

The contributions of each fluctuation-source (noise or aerosol) to the total errors on the IOP were calculated from (equation 7.3). Table (7.5) shows that the errors due to sensor's noise are the major contributor to the uncertainties on the estimated concentrations of chlorophyll-a ($> 55\%$) and DOM (>92 %). On the other hand, the aerosol-induced-errors constitute more than 75% of the SPM error-budget. In general, the average (over sites) contributions of the aerosol and noise induced-errors on the error-budget of Chl-a are 25% from aerosol and 75% from noise. This proportion is inverted for SPM to be around 75% from aerosol and the rest 25% are from noise. For DOM the proportion becomes 5% from aerosol while the other 95% are from noise-induced errors. These results are with respect to equal probabilities of having noise or atmospheric errors. Let us note that the contribution of aerosol induced-error to the total error-budget of Chl-a increases at the sites with zero values of the DOM absorption coefficient (consult sections 6.3.3, 6.3.5 and 7.3.2).

site	chlorophyll-a		DOM		SPM	
	aerosol	noise	aerosol	noise	aerosol	noise
P1	14.74	85.26	7.19	92.81	79.49	20.51
P1+	33.45	66.55	*	*	81.11	18.89
P2	44.31	55.69	*	*	75.00	25.00
P4	40.90	59.10	*	*	75.37	24.63
P5++	5.24	94.76	4.28	95.72	76.46	23.54
P6	5.26	94.74	4.13	95.87	75.72	24.28

Table 7.5: The relative contributions of noise and aerosol -induced errors to the total error-budget of the IOP.

7.3.4 Using the residuals between DAIS reflectances and model predictions

Constructing the confidence intervals on model predictions

Equations (7.4 and 7.5) were used to construct the 95% confidence interval around the predictions of the model (figure 7.5). The goodness of fit was

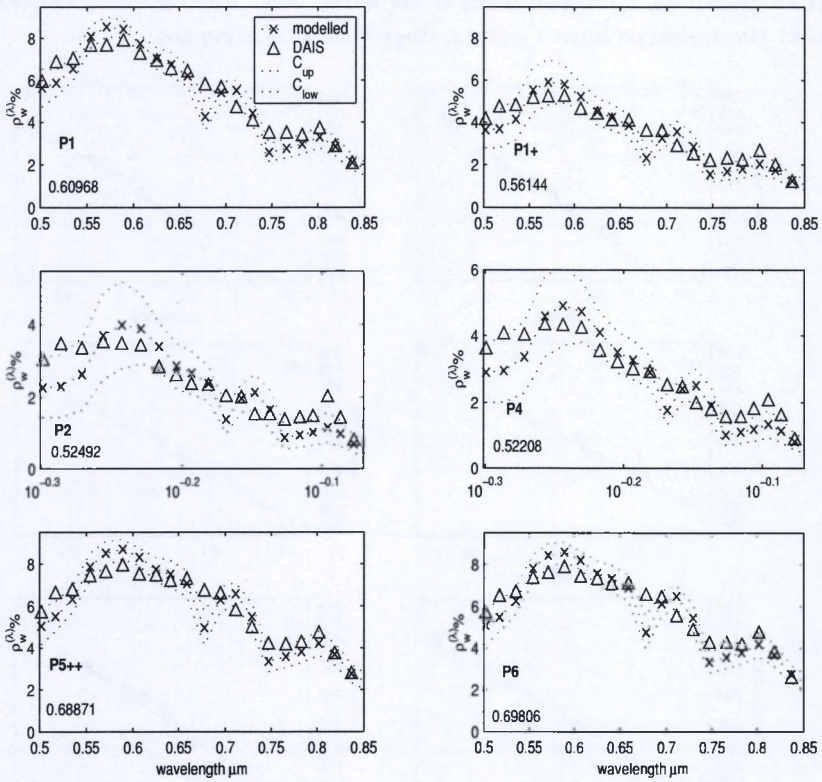

Fig. 7.5: Modelled versus DAIS water leaving reflectances with 95% of confidence with upper bound C_{up} and lower bound C_{low}. The numbers in each panel represent the root-mean-square of the residuals.

calculated as being the root-mean-square of the residuals. Figure (7.5) shows that the image spectra are within the 95% confidence of the modelled values except for the bands 0.67-0.8 μm (as it was explained in section 7.3.2). The confidence intervals of figure (7.5) are accepted if the residuals are small and normally distributed. Figure (7.6) shows the residuals displayed with the symbol '+'. Superimposed on each plot is a line joining the first and third quartiles. This line is extrapolated out to the ends of the sample to evaluate the linearity of the data. If the residuals does come from a normal distribution, the plot will appear linear. Other probability density functions will introduce curvature in the plot. The plots in figure (7.6) are linear,

indicating that the residuals can be modelled by a normal distribution. This conclusion was confirmed using a normality test. Therefore the hypothesis that the residuals have a normal distribution, is accepted.

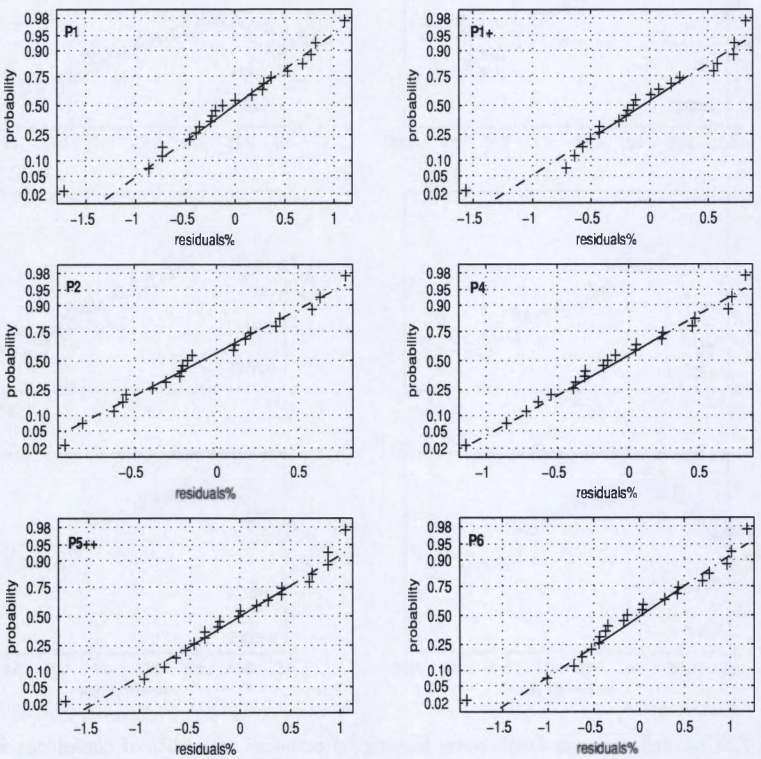

Fig. 7.6: The normal probability fit (line joining the first and third quartiles) of the residuals at each sampling site.

Generating random spectra

Although the upper and the lower bounds of the water leaving reflectance might give (through inversion) the upper and lower bounds on backscattering coefficient of SPM, it will certainly not give the upper and lower bounds on the absorption coefficients of chlorophyll-a and DOM. Randomly generated water spectra is the only way to construct the bounds on the whole IOP vector. The normal distribution is used to generate random spectra (i.e. synthetic water leaving spectra) around $\rho_{w0}^{(\lambda)}$ within the confidence intervals $\rho_{w\pm 0}^{(\lambda)}$ (equation 7.5). Two kinds of random spectra were generated.

The first is wavelength dependent:

$$\rho_w^{(\lambda)} = \rho_{w0}^{(\lambda)} + Ran \times \rho_{w\pm0}^{(\lambda)} \tag{7.6}$$

Where *Ran* is a random number with 95% probability to be between -1 and 1. The second type of random spectra are independent of wavelength:

$$\rho_w^{(\lambda)} = \rho_{w0}^{(\lambda)} + Ran\left(0, 0.5\rho_{w\pm0}^{(\lambda)}\right) \tag{7.7}$$

This time the random number *Ran* is generated with 95% probability to be in the range $\pm\rho_{w\pm0}^{(\lambda)}$. Equations (7.6) and (7.7) are used because fluctuations (in DAIS data) might occur from variations in the spectral-response of the sensor and imperfect atmospheric (aerosol) corrections (consult section 7.2). The random fluctuations resulting from imperfect aerosol correction should therefore be spectrally correlated whereas the noise-fluctuated data should be spectrally independent. The noise-fluctuated and aerosol-fluctuated water-leaving spectra are assumed to have equal chance of occurrence. In other words, the probabilities of having noise or aerosol errors is the same. Equal number of wavelength- dependent/ -independent random spectra were therefore generated. The IOPs were estimated from each randomly-generated spectrum using the optimization procedure of chapter (6). The populations of the differences were then used to calculate the confidence intervals on the vector $\mathbf{iop}_0$. The confidence interval on the IOP was estimated for the relative errors. This relative measure is used to eliminate the influence of the SIOP on the relative errors. Thus, the relative error of the IOP is equal to that of the associated constituent's concentration. Figure (7.7), shows the half width of relative errors (of the IOP) with 95% of confidence using the spectrally dependent random number, spectrally independent random number and both of them respectively. The 95% confidence was calculated as being two standard deviations from the mean-difference which is normalized to the solution vector $\mathbf{iop}_0$. Figure (7.7) shows the influence of the spectral correlation of the random fluctuations, on the relative bound on the IOP. The concentrations of DOM and Chl-a are less sensitive to the wavelength-dependent fluctuations (e.g. imperfect aerosol removal) than to the spectrally-uncorrelated fluctuations (e.g. sensor noise). This situation was converted for SPM concentrations (see table 7.5). However assuming an equal-probability of having fluctuation from sensor noise and atmospheric correction (both wavelength -dependent and -independent) will increase the uncertainty on the retrieved IOP. In the three cases (i.e. fluc-

tuation dependent and/or independent of wavelength) SPM has the best accuracy in the retrieved concentrations. Actually the uncertainties on the SPM and DOM have clear trend in decreasing with increasing the concentrations whereas chlorophyll-a does not show a similar trend. However the uncertainty in estimated concentrations of chlorophyll-a also increases with decreasing the concentration of SPM (relatively SPM-clear water). Similar observation was stated in sections (6.4.4) and (7.2) (i.e. large errors in the estimated IOP of relatively SPM-clear water). This type of water is observed at the sites P2 and P4. At these sites, the modelled and recorded water leaving reflectances did not exceed 4.5% at 0.555 μm with SPM concentrations of 22 g.m^{-3} and 18 g.m^{-3} respectively. Whereas this value (of the water leaving reflectance at 0.555 μ m) was bigger than 6% in all the other sites (SPM >50 g.m^{-3}). The proportional contributions of aerosol

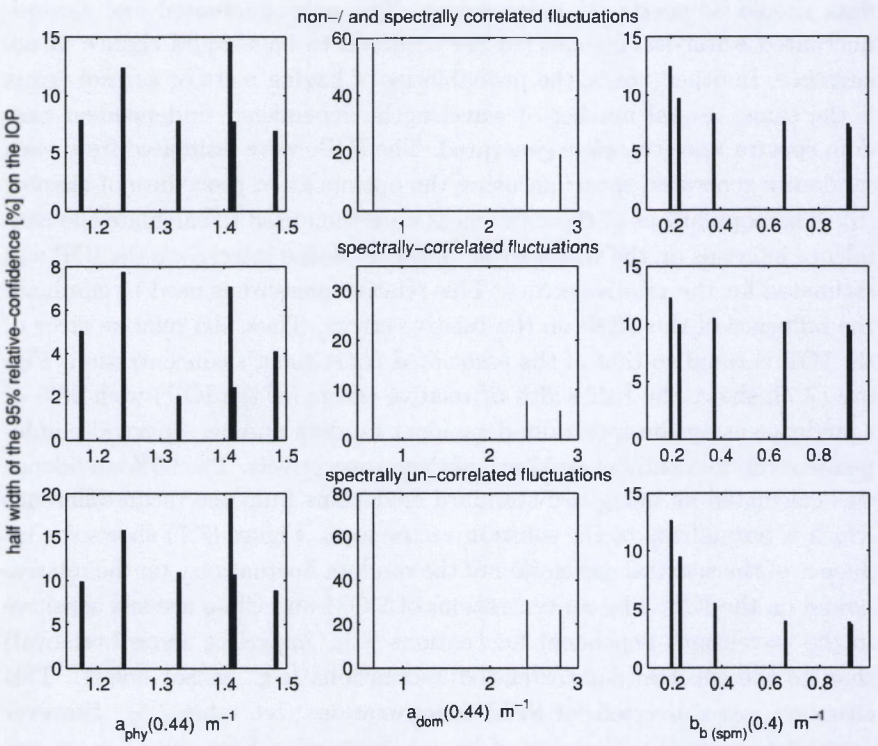

Fig. 7.7: Half width of the relative errors (with 95% of confidence) on the IOP using the spectrally dependent random number, spectrally independent random number and both of them respectively.

and noise fluctuation to the total error budget of SPM, DOM and Chl-a were isolated in section (7.2.1). Table (7.5) can therefore be used with the results of the upper panel of figure (7.7) to separate the errors on the IOP to their components, being caused by imperfect aerosol correction or sensor noise (figure 7.8).

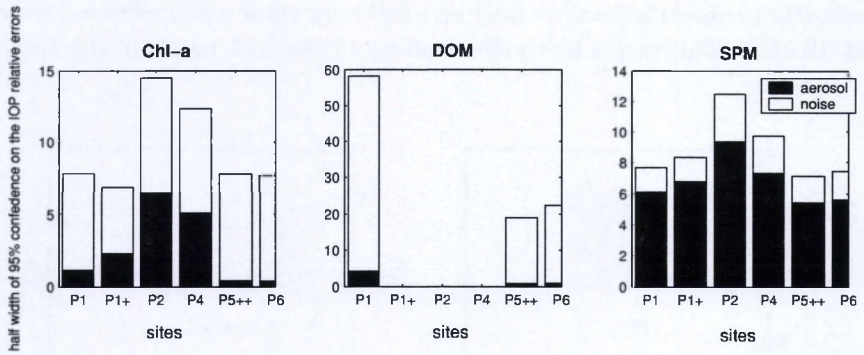

Fig. 7.8: Half width of the relative contributions (with 95% of confidence) of the aerosol and noise induced errors to the total error-budget on the IOP.

7.3.5 Validation with multi-spectral in situ sensor: SIMBADA

The proposed stochastic approach was applied on the spectra acquired by SIMBADA (see figure 7.12(a)). The IOP were first extracted from the recorded reflectances using the implicit inversion technique (chapter 6). Second the deviations between model predictions and SIMBADA readings were used to construct a 95% confidence interval (i.e. uncertainty bound) around model-generated spectra. Note that SIMBADA spectra are relatively (comparing to DAIS spectra) free of the atmospheric path reflectance. Therefore, only fluctuations due to sensor's noise were considered i.e. wavelength independent random spectra (equation 7.7). The spectra in figure (7.9) have wide uncertainty bounds (compare to figure 7.5). This is because the uncertainty bound will be wider if the number of bands N approaches the number of retrieved parameter m. In this case the spectra of SIMBADA have three degree-of-freedoms comparing to the 18 degree-of-freedoms for DAIS spectra. Estimating the IOP from the water leaving reflectances acquired by SIMBADA will therefor have large uncertainties (figure 7.10). These uncertainties (in figure 7.10) were quantified using equation (7.7)

with 1000 realizations. The concentrations of Chl-a and SPM were then estimated from the retrieved IOP (from SIMBADA spectra) and measured SIOP (figure 7.10). Let us note that while the inversion of DAIS spectra predicted a DOM-free water at three sites (P1+, P2 and P4), the inversion of SIMBADA spectra predicted DOM-free waters at all sites. Moreover, the estimated concentrations of Chl-a and SPM are lower when retrieved from SIMBADA. This might be to the artifacts in the NIR bands of the DAIS

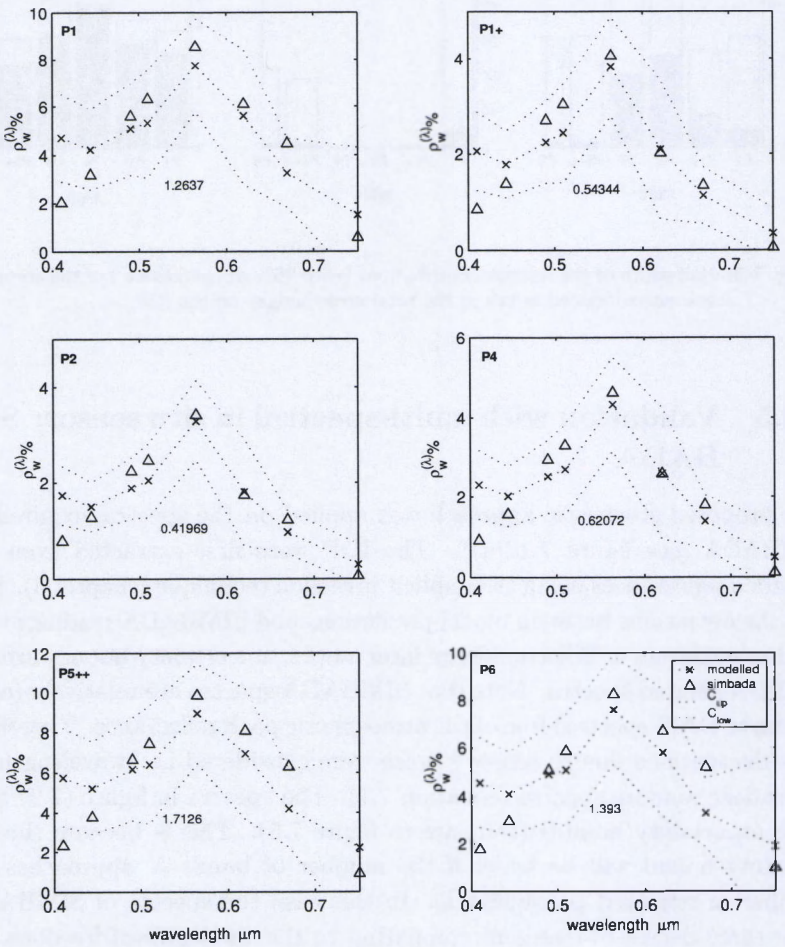

Fig. 7.9: Modelled versus measured (by SIMBADA) water leaving reflectances with 95% of confidence with upper bound C_{up} and lower bound C_{low}. The numbers in each panel represent the root-mean-square of the residuals.

sensor. The large relative-uncertainty bounds in figure (7.10) are mainly due to the approximation (equation 7.5) of the confidence intervals around the predicted spectra. This approximation is valid for observation with large degree-of-freedom and hence at large number of spectral bands (i.e. hyperspectral). The uncertainties on retrieved SPM and Chl-a increase in turbid waters. This is in contrary to the results obtained from DAIS (figure 7.8). This is due to some limitations in SIMBADA, namely the number of the spectral bands and their position.

Let us note that the techniques (developed in chapters 6 and 7) were applied and tested on hyperspectral data which covered the whole visible-NIR spectrum. The width of the confidence interval is inversely related to the number of spectral bands (equations 7.4 and 7.5 and figure 7.9). Therefore the retrieved IOPs, form SIMBADA readings, are subjected to high fluctuations-level which increases their uncertainties. Moreover the unique peak of SPM-rich water between 0.8-0.82 μ m is not covered by SIMBADA spectral-bands. This range is very important for turbid waters with SPM concentration > 30 g.m^{-3} (demonstrated in chapter 5) and observed in figure 7.10(b)). The SPM concentrations, estimated from SIMBADA-spectra, are therefor vulnerable to wider range of errors. Any error in the retrieved SPM will lead to increased uncertainty on Chl-a (figure 7.10(a)). In the sense that the fitting procedure will suppress any increase in SPM by over-estimation of Chl-a (see the discussion in section 7.3.2).

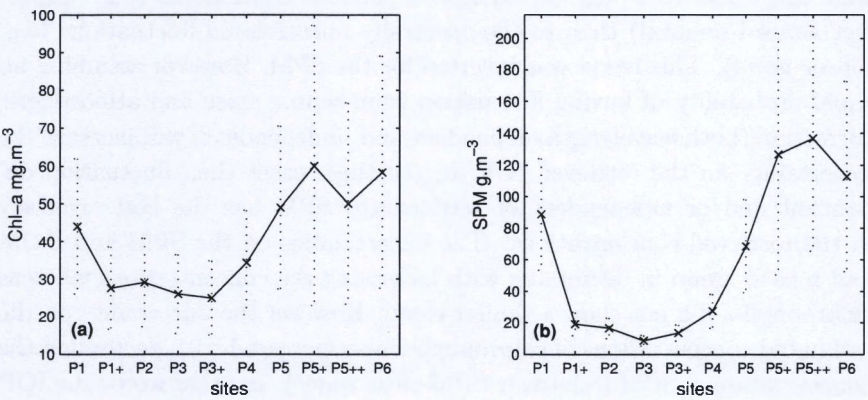

Fig. 7.10: The estimated concentrations of (a): Chl-a and (b): SPM with 65% of confidence (the dotted bars) after 1000 iterations.

7.4 Conclusion and remarks

A stochastic approach was proposed to estimate the bounds of relative-uncertainty around the retrieved IOP. In turn the errors were separated according to their sources due to imperfect atmospheric correction and sensor noise. A sensitivity analysis on the IOP was then performed to evaluate error budgeting and propagation for each perturbation component.

The proposed technique was applied on DAIS spectra using the residuals, resulting from the inversion, to construct a 95% confidence interval around the modelled reflectance. Random spectra of water leaving reflectance were generated within this confidence interval. The IOP vector was estimated for each of the random-generated spectrum. The differences between the solution vector $\mathbf{iop}_0$ and the stochastically simulated IOP were used to construct the 95% confidence intervals around the solution vector $\mathbf{iop}_0$. The width of the confidence interval gave an idea about the sensitivity of the retrieved IOP to small fluctuations in the recorded reflectance. In general, when the Rayleigh reflectance is accounted correctly the average (over sites) contributions of the aerosol and noise induced-error to the error-budget of SPM are 75% from aerosol and 25% from noise. This proportion is inverted for chlorophyll-a to be around 25% from aerosol and 75% from noise. For DOM the proportion becomes 5% from aerosol while 95% are from noise induced errors. This outcome is correct for equal probabilities of occurrence for noise or aerosol errors. The retrieved Chl-a and DOM concentrations were less sensitive to the wavelength-dependent fluctuations (e.g. imperfect aerosol removal) than to the spectrally-uncorrelated fluctuations (e.g. sensor noise). This trend was inverted for the SPM. However assuming an equal-probability of having fluctuation from sensor noise and atmospheric correction (both wavelength -dependent and -independent) will increase the uncertainty on the retrieved IOP. In the three cases (i.e. fluctuation dependent and/or independent of wavelength) SPM has the best accuracy in the retrieved concentrations. The uncertainties on the SPM and DOM had a clear trend in decreasing with increasing the concentrations whereas chlorophyll-a did not show a similar trend. However the uncertainty on the estimated concentrations of chlorophyll-a also increased with decreasing the concentration of SPM (relatively SPM-clear water). In other words the IOP of SPM-clear waters are more sensitive to fluctuations in the recorded reflectance.

The estimated uncertainty bounds on the IOP were relative and, therefore, independent of the SIOP. Thus, provided the water leaving reflectance,

the algorithm will give the confidence intervals on the concentrations of SPM, chlorophyll-a and DOM yet to be retrieved.

7.5 Appendix

7.5.1 Characteristics of the sensor

DAIS is a 79-channel Digital Airborne Imaging Spectrometer (DAIS 7915). This sensor covers the spectral range from 0.502 to 12.3 μm. Table 7.6 summarizes the spectral and geometrical characteristics of the sensor.

Parameter	DAIS sensor
Dynamic range [bit]	15
FOV [o]	$\pm$ 26
IFOV [mrad]	3.3
spectral range [μm]	0.5-12.3
Number of bands (0.5-0.85 μm)	21
Spectral interval [nm]	varies
Spatial resolution [m]	$\approx$ 6
flight altitude [m]	$\approx$ 4000
NER [$w/sr.m^2.\mu$m]	0.25

Table 7.6: The operational mode of DAIS sensor.

7.5.2 Planning the flight lines

The DAIS sensor scanned a sub-region of the Belgian coastal waters, off shore Oostende, with one DAIS. The constraints in preparing a flight line were:

- Avoid sun glint and specular reflection from the sea surface.
- Maintain an acceptable signal-to-noise-ratio.
- Minimize the variations in illumination-intensity across the flight line.
- Maintain the accessability to the sampling sites which is subjected to the tidal cycle (i.e water level).

To achieve a reasonable flexibility, several time dependent-scenarios were realized in figure (7.11). The flight lines scenarios were for a point near Oostende (Lat: 51.233, Long: 2.933) and for the 25th of June 2001 (the DAIS over-flight). The above conditions can be fulfilled at sun zenith between 30-50 degrees and the sun is at the back or front of the aircraft. To achieve the last requirement the beginning point of the flight line (the square in the middle of figure 7.11(b)) was fixed. Then the flight line rotated following the sun azimuth. The best flight line was depending on the alignment of the shore line and water level. The shoreline (in figure 7.11(b)) was

modelled as a line with an angle of 57° w.r.t. the north line in the clockwise direction.

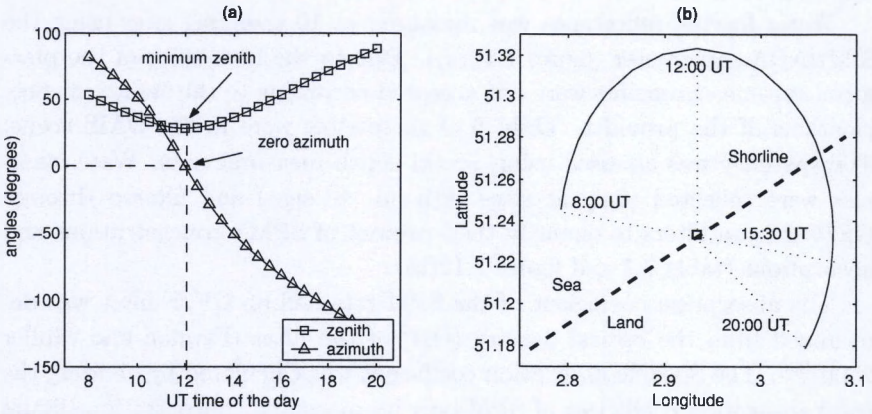

Fig. 7.11: The variation of the flight line as function of solar angles, position and date. (a): solar angles as function of time. (b): variations of the solar azimuth.

7.5.3 In-situ measurements

Complete details about the in-situ measurements performed during this research can be found in Salama and Monbaliu (2003) [100] and Salama and Monbaliu (2003)[99]. During the DAIS overflight, water reflectance, transparency, absorption and SPM content were measured at four sites (with

site ID	local time	coordinates		turbidity	
		lat	long	transparency [m]	SPM [g.m^{-3}]
P1	10:53	51.266	2.914	0.55	55
P1+	11:10	51.28	2.868	***	***
P2	11:21	51.3	2.826	2.3	22
P3	11:36	51.314	2.783	3.7	7
P3+	11:58	51.316	2.818	***	***
P4	12.:09	51.305	2.853	1.7	18.6
P5	12:27	51.316	2.897	0.65	33.6
P5+	12:40	51.303	2.915	***	***
P5++	12:50	51.288	2.932	***	***
P6	13:02	51.277	2.95	0.4	153.5

Table 7.7: The sites of in-situ measurements during the DAIS flight campaign 25th of June 2001. The '+' sign (and hence the stars) indicate that water samples were not collected.

no '+' sign, see table 7.7). These sites will be used to assess the performance of the atmospheric correction and hydro-optical model and the accuracy of the measurements.

Water leaving reflectance was measured at 10 sampling sites using the SIMBADA radiometer (figure 7.12(a)). Due to the instability of the platform, sun-measurements were not accepted according to the standard specifications of the provider. Only 6 of these sites were in the DAIS scene. Transparency was assessed using Secchi depth measurements. Water samples were collected (only at sites with no '+' sign) and filtered through GF/F 0.7 μm filters to quantify their content of SPM's concentrations and absorptions (table 7.7 and figure 7.12(b)).

The absorption coefficient of the SPM retained on GF/F filter was determined from the optical density (OD) of the filter (Fargion and Muller 2000)[23]. The Specific absorption coefficient was calculated by dividing the total absorption coefficient of SPM over its measured concentration (figure 7.12(b)). Let us note that the site P6 (figure 7.12(b)) has the highest value of the absorption coefficient (at 0.443 μm). This might be due to the high concentration of SPM at this site (table 7.1). This high concentration might prolong the optical path of the filter. Thus the spectrometer might register an erroneous high-value of the absorption coefficient for this site (see figure 7.12(b)). The effect of light backscattering by particles could be eliminated if the spectrophotometer was equipped with an integrating sphere (Tassan and Ferrari 1995)[127].

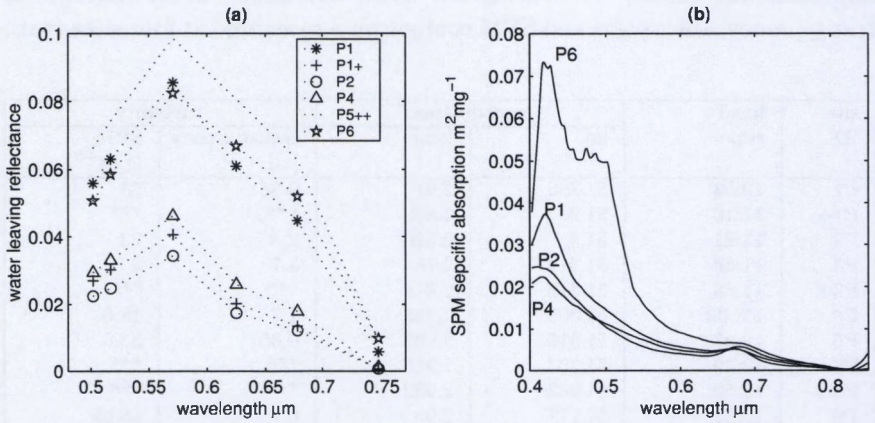

Fig. 7.12: In-situ measurements of some AOP and IOP during the DAIS campaign, the 25th of June 2001.(a): SIMBADA water leaving reflectance. (b): specific absorption spectra of SPM.

7.5.4 Atmospheric correction

The total recorded reflectances of DAIS were corrected for gaseous absorption, Rayleigh and surface reflectance. The data (aerosol optical thickness, water content and solar irradiance) recorded by the sun-photometer situated at Oostende were then used to generate the aerosol scattering at the sensor level (Vermote *et al.*, 1997)[45]. The resulting water leaving reflectances are illustrated in figure (7.13). The water leaving reflectances estimated from DAIS agreed with the readings of SIMBADA for all sites at the band 0.555 μm. This agreement at 0.555 μm gives more confidence on the atmospheric correction. This is because a good atmospheric correction will produce close estimates between the reflectance recorded by SIMBADA and DAIS. The aerosol reflectances were estimated by substracting the modelled and measured water leaving reflectances from the total corrected reflectances of DAIS (figure 7.14). The resulting aerosol reflectances

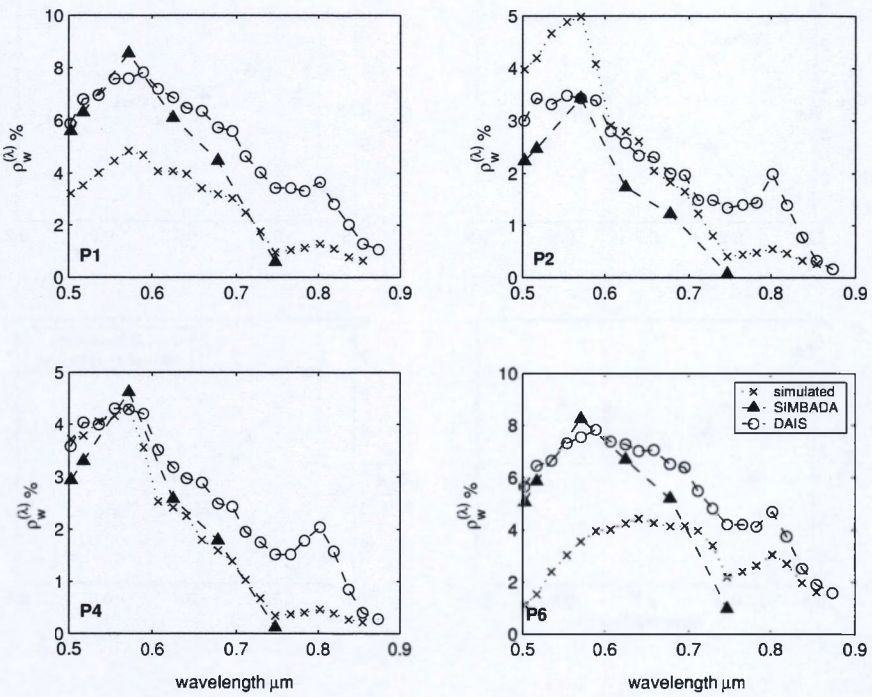

Fig. 7.13: The water leaving reflectance measured by DAIS and SIMBADA and predicted from equation (2.39).

(figure 7.14) from DAIS-SIMBADA and DAIS-model show that except for the site P4 model predictions deviate from measurement predictions. Let us note the the dip at 0.555μm band (figure 7.14) should not wrongly be interpreted as an absorption band of aerosol. It only means that the estimations of aerosol scattering at bands other than the 0.555μm are poor. Actually, we cannot expect a good fit between the readings of different devices. This is because DAIS reflectances are for one location. Each pixel of DAIS is associated with a water volume of 1 to hundreds cubic meters (depending on the penetration-depth). On the other hand the water leaving reflectances measured by SIMBADA (single measurement) are associated with a point measurement that is an order-of-magnitude smaller. Upon on that the measured inherent optical properties are associated with sample volumes ranging from order of cubic millimeter to cubic centimeters. These

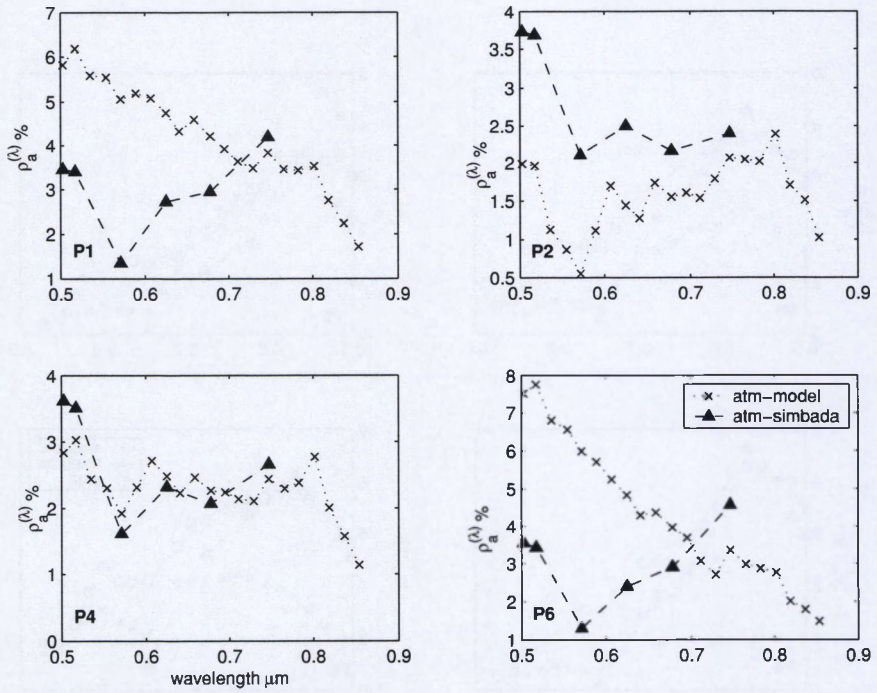

Fig. 7.14: Aerosol reflectance at the sensor level calculated from the corrected reflectances and the modelled (atm-model) and measured (atm-simbada) water leaving reflectances.

variations in the sampling volumes will create a scale closure that is difficult to be satisfied.

The most important observation, however, is that the predictions of the model (equation 2.39 feeded with elementary measurements of the IOP) largely deviate from SIMBADA readings. This can be explained that the model is not appropriate for water with high concentrations of Chl-a or DOM (see section 2.4.2). Let us note that the water leaving spectra acquired by DAIS and SIMBADA, both, predicted (via inversion) waters with high concentrations of Chl-a (see tables 7.1 and 7.10).

Chapter 8

Conclusion and remarks

8.1 Summary

The inherent optical properties (IOP) of a water body (namely: absorption coefficients and the volume scattering function) completely characterize the water leaving radiance and other related quantities (i.e. AOP) that can be measured by remote sensing techniques. The IOP of the surface water are estimated using implicit-inversion which solves a sequence of forward problems. The forward model defines exactly the apparent optical properties of the water column providing its inherent optical properties. The water leaving reflectance (or any AOP) can be computed following one of the two approaches. The first solves the radiative transfer equation providing the bulk IOP. The second approach employs Mie theory to compute the water leaving reflectance using the IOP of a single, perfectly shaped, particle. This implies that the bulk IOP are the sum of the IOP of individual particles. In other words, there is a closure between the scales of the bulk IOP and the single-particle IOP. Extensive research and measurements are needed before narrowing the gap of scale closure.

The light through its path back to the sensor experiences several attenuations events. This is due to the scattering and absorption by air molecules and aerosol. The calculation of Rayleigh scattering of air molecules is well described in terms of geometry and pressure. Gaseous absorption can be calculated knowing the altitude and the season. Aerosol scattering is the most significant contributor to the total received reflectance. The signals arising from aerosol scattering have large spatial and temporal variabilities. Thus, the aerosol scattering has to be quantified directly from measured

reflectance.

8.2 Contributions

In chapter (3) we developed a technique that retrieved the aerosol ratio at two bands from the AVHRR corrected reflectance. The approach was successfully extended and applied (in chapter 4) on SeaWiFS images. This was to replace the visual inspection by an automated process that is based on a statistical technique.

In chapter (5) a coupled atmosphere-ocean approach is proposed for turbid waters. This algorithms considers, and retrieves, the spatial variability of the aerosol and water reflectance ratios at the NIR. Two assumptions were imposed on three bands at the NIR (>0.8 μm). First, the water leaving reflectance is optically governed by the SPM and water molecules. Second, the aerosol in the multiple scattering regime follows the same spectral dependency of the single scattering regime. With respect to these assumptions a rigorous solution to the atmospheric-correction problem was established. For each triplet of corrected reflectance exact values of the aerosol and water reflectance ratios are found.

In chapter (6) we developed an implicit method to retrieve the bulk IOP from the water leaving reflectance. Sets of the IOP were feeded to the semi-empirical model to generate water leaving spectra. The measured reflectance was fitted to these pre-generated spectra of water leaving reflectance. The sought IOP were assumed to be of the modelled-spectrum with the best-fit to the measurement.

In chapter (7) a stochastic approach was developed that used the residuals between model predictions and measured spectrum to construct a 95% confidence interval around the modelled reflectance. The width of the confidence interval was then used to quantify the sensitivity of the IOP to fluctuations in the recorded reflectance. In turn, these fluctuations were separated according to two perturbation sources, namely imperfect atmospheric correction and sensor noise. A sensitivity analysis on the IOP was then performed to evaluate relative contribution of each perturbation component to the total error-budget of the IOP. In general, the errors in the estimated concentrations of SPM are aerosol dominant while the uncertainty on the retrieved concentrations of chlorophyll-a and DOM is governed by sensor noise.

A step for future research was proposed (in section 8.2.4).

8.3 Recommendation

8.3.1 In-situ measurements

In-situ measurements are the basis for calibrating and validating any proposed algorithm. The measurement procedure should consist of collecting samples for laboratory analysis, radiometric measurements and ancillary data. These measurements should be concurrent with image acquisition. It is advisable to divide the ground-reference sites into calibration and algorithm-validation sites. The calibration sites fall into two classes namely algorithm-calibration and vicarious-calibration sites. In the first step, algorithm-calibration sites are used to force the closure between measurements and the model predictions. The sites for vicarious-calibrations are only used to calibrate the sensor and correct for any spectral (or thermal) shift. In the second step the models (atmospheric correction and inversion technique) are validated against the measurements from the algorithm-validation sites. An important constraint in determining sampling locations is the accessibility to these sites. The depth profile of the SIOP, IOP and AOP of the water column should be measured at these sites. This should be associated with quantitative estimation of the water constituents. The ideal sampling campaign would measure independently each SIOP, IOP, AOP and constituents's concentrations in the water column. In this approach the measurement closure can be assessed.

8.3.2 Coastal areas

Normally coastal areas (shallow waters, shorelines, salt marches and mud flats) have received minor attention in remote sensing due to their optical complexity. These coastal environments are at risk from development and climate change. Remote sensing offers the only realistic means of acquiring the required measurements to study these large and often inaccessible areas (e.g. mud flats). In particular, hyperspectral technology provides data that can be used to derive the desired characteristics of any coastal environment. The objective of remote sensing over coastal areas is to assess the quality of coastal waters and the morphological changes of coastal areas. This should include mapping and measuring the changes of the coastal areas over time. Second, assessing their physical and biological characteristics. These measurements, along with information on hydrodynamics and climate processes, can then be used to determine the quality of coastal waters and the morphological change of coastal environments.

8.3.3 Exact forward modelling

The inversion of remote sensing signals (i.e. atmospheric corrections and estimating the IOP) is quite problematic in coastal zones. This is due to the high turbidity of the water, bottom reflectance, organic content and the adjacency effects from land (e.g. mud-flats) to the water column and vice versa. Therefore a careful modelling of the interactions of light with matter is required. To obtain reasonable results from inverse modelling (hence remote sensing), the forward modelling should be realized within a high degree of confidence. Normally the IOP of the water are retrieved using implicit-inversion which solves a sequence of forward problems. Therefore a reliable forward solution is the necessary reference to the inverse modelling and in-situ measurements. The right approach would be an exact solution of the RTE (e.g. Thomas and Stamnes 1999[5], Mobley 1994[2]) or Mie calculations (e.g. Van de Hulst 1981[27], Bohren and Huffman 1983[28]) with an accurate treatment of the boundary conditions.

8.3.4 Coupling Mie and radiative transfer calculations

It seems possible to link the inversion technique developed in chapter (6) to Mie calculation of single particles. This is due to the fact that the optics of a single particle can be linked to the bulk optical properties of sea waters (Morel 1994)[40]. However the single-particle-to-bulk-IOP scale closure is difficult to be made (Mobley 1994[2], Zaneveld 1994[38]). Nevertheless, similar approach was successfully applied on seawater (Gordon and Du 2001[121], Twardowski *et al.*, 2001[120] and Balch *et al.*, 1999[128]). Therefore the proposed method in this section might provide essential information on the backscattering fraction, index of refraction and possibly the particle-size distribution.

Volume scattering function

Any wrongly assumed scattering phase function would not describe the fraction of backscattering and neither the shape of the angular distribution of up-welling radiance within the water. This will lead to considerable errors in computed AOP (forward modelling) and retrieved IOP (i.e. inverse modelling). Most studies (as well as this thesis) used a fixed backscattering fraction that can only occur in very clear waters (Gordon 1993)[129]. To our understanding the shape and the magnitude of the volume scattering function (hence backscattering fraction) are determined by the index of

refraction, particles-size distribution and concentration of the SPM in the water column. Therefore it is crucial to accurately estimate and measure the fraction of backscattering and the associated scattering phase function.

Constant SIOP

The concentrations of SPM were estimated from the retrieved IOP and measured SIOP. The measured SIOP were assumed to have constant values. This assumption is acceptable for a region at which the SIOP's have been locally-measured (i.e. in-situ) during a specific season (Mikkelsen 2002)[116]. The SIOP of a constituent is a measure of the absorption/scattering efficiency of the particle cross section. The SIOP will vary with particle-size distribution, chemical, biological and mineral composition of the particle. This can be described by a particle-size distribution function and the index of refraction of the particles being suspended in the water. The cross section s of a particle plays an essential role in defining its optical efficiency as scatterer or absorber. The particle can thus be characterized by scattering, absorption and attenuation efficiency factors. The efficiency factor of absorption Q_a or scattering Q_b is the ratio of scattered energy to the total incident energy crossing the geometrical section of a particle. These efficiency factors can be linked to the corresponding bulk IOP (absorption or scattering coefficient) knowing the particle-size distribution function (PSD) of the constituents (Morel 1994)[40].

Proposed method

We propose an algorithm to estimate the IOP, index of refraction and fraction of backscattering from image reflectance alon. The method couples the implicit inversion of the radiative transfer equation (RTE) with simulations from Mie theory (Bohren and Huffman 1983)[28] in an iterative scheme. The inputs to start Mie computations are index of refraction, particle-size distribution PSD and the wavelength. The output are the intensities and directions of scattered beams and efficiency factors. The backscattering and absorbtion efficiency factors can be up scaled to the bulk IOP. The computations are repeated by changing the values of index of refraction. This is continued until the values of the backscattering and absorbtion coefficients agrees with those resulted from the inversion of the RTE. In other words, the absorption and backscattering coefficients are used as the key-parameters to measure the fit between the radiative transfer and Mie computations of

the light field. The expected outputs are IOP, fraction of backscattering and the index of refraction.

This approach might provide the necessary information that links the bulk IOP to the particle-level IOP. This information is essential for quantifying the concentrations of SPM and other marine quantities. This might open the way for a new approach to estimate the fraction of backscattering and the specific inherent optical properties (SIOP) from image reflectance. However, extensive measurements on the AOP, IOP, SIOP, refractive index of the particles and their size distribution are needed to validate such an approach. Moreover these in situ measurements are necessary to investigate the scale closure from the single particle IOP to bulk IOP.

Bibliography

[1] Preisendorfer R. *Hydrologic optics*, volume I: introduction. 1976.

[2] Mobley C. *Light and water radiative transfer in natural waters.* Academic Press, 1994.

[3] Spinrad W., Carder K., and Perry M. *Ocean Optics.* Oxford University Press, 1994.

[4] Bukata R., Jerome J., Kondratyev K., and Pozdnyakov D. *Optical properties and remote sensing of inland and coastal waters.* CRC Press, 1995.

[5] Thomas G. and Stamnes K. *Radiative transfer in the atmospher and ocean.* Cambridge; University Press, 2002 edition, 1999.

[6] Lee Z., Carder K., Mobley C., Steward R., and Patch J. Hyperspectral remote sensing for shallow waters. 1. a semianalytical model. *Applied Optics*, 37(27):6329–6338, 1998.

[7] Morel A. and Gentili B. Diffuse reflectance of oceanic waters II. bidirectional aspects. *Applied Optics*, 32(33):6864–6879, 1993.

[8] Morel A. and Gentili B. Diffuse reflectance of oceanic waters .3. implication of bidirectionality for the remote-sensing problem. *Applied Optics*, 35(24):4850–4862, 1996.

[9] Gordon H., Brown O., Evans R., Brown J., Smith R., Baker K., and Clark D. A semianalytical radiance model of ocean color. *Journal of Geophysical Research*, (93):10909–10924, 1988.

[10] Lee Z., Carder K., Mobley C., Steward R., and Patch J. Hyperspectral remote sensing for shallow waters: 2. deriving bottom depths and water properties by optimization. *Applied Optics*, 38(18):3831–3843, 1999.

[11] IVM. Measurements of the SIOP in the North Sea. personal communication, 1999-2000.

[12] Morel A. Optical properties of pure water and pure seawater. In Jerlov N.G. and Nielson E.S., editors, *Optical aspects of oceanography*, pages 1746–1754. 1974.

[13] Pop R. and Fry E. Absorption spectrum (380-700nm) of pure water: II, integrating cavity measurements. *Applied Optics*, 36(33):8710–8723, 1997.

[14] Smith R. and Baker K. Optical properties of the clearest natural waters (200-800 nm). *Applied Optics*, 20:177–184, 1981.

[15] Hale G. and Querry M. Optical constants of water in the 200 nm to 200 μm wavelength region. *Applied Optics*, (12):555–563, 1973.

[16] Palmer K.F. and Williams D. Optical properties of water in the near infrared. *Journal of Optical Society of America*, (64):1107–1110, 1974.

[17] Bricaud A., Morel A., and Prieur L. Absorption by dissolved organic-matter of the sea (yellow substance) in the UV and visible domains. *Limnology and Oceanography*, 26(1):43–53, 1981.

[18] Eisma D. and Kalf J. Distribution and particles size of suspended matter in the southern bight of the North Sea and the eastern channel. *Netherlands Journal of Sea Research*, 13(2):289–324, 1979.

[19] Petzold T.J. *Volum scattering functions for selected ocean waters*, chapter 12 in Light in the sea, pages 150–174. Hutchinson&Ross, 1977.

[20] Gordon H. *Modeling and simulating radiative transfer in the ocean*, chapter 1 in Ocean Optics, page 283. Number 25 in Oxford Monographs on Geology and Geophysics. Oxford University Press, 1994.

[21] Kopelevich O. V. *Small-parameter model of optical properties of sea waters*, volume 1 Physical Ocean Optics, chapter 8 in Ocean Optics. Nauka, 1983.

[22] Haltrin V.I. and Kattawar G. Light fields with raman scattering and fluorescence in sea waters. Technical, Department of Physics,Texas University, 1991.

[23] Fargion S. and Muller J. Ocean optics protocol for satellite ocean color sensor validation, revision 2. Protocol Tm-2000-209966.87-97, NASA, 2000.

[24] Terrill E., Melville W., and Stramski D. Bubble entrainment by breaking waves and their influence on optical scattering in the upper ocean. *Journal of Geophysical Reseach*, 106(C8):16815–16823, 2001.

[25] Yan B., Chen B., and Stamnes K. Role of oceanic air bubbles in atmospheric correction of ocean color imagery. *Applied Optics*, 41(12):2202–2212, 2002.

[26] Zhang XD., Lewis M., Lee M., Johnson B., and Korotaev G. The volume scattering function of natural bubble populations. *Limnology and Oceanography*, 47(5):1273–1282, 2002.

[27] van de Hulst H. *Light scattering by small particles.* Dover, Mineola, N.Y. edition, 1981.

[28] Bohren C. and Huffman D. *Absorption and scattering of light by small particles.* John Wiley, N.Y. edition, 1983.

[29] Kirk J. *The relationship between the inherent and apparent optical properties of surface waters and its dependence on the shape of the volume scattering function*, chapter 2 in Ocean Optics, page 283. Number 25 in Oxford Monographs on Geology and Geophysics. Oxford University Press, 1994.

[30] Lee Z., Carder K., Marra J., Steward R., and Perry M. Estimating primary production at depth from remote sensing. *Applied Optics*, 35(3):463–474, 1996.

[31] Gordon H., Brown O., and Jacobs M. Computed relationships between inherent and apparent optical-properties of a flat homogeneous ocean. *Applied Optics*, 14(2):417–427, 1975.

[32] Gordon H. Radiative-transfer in ocean - method for determination of absorption and scattering properties. *Applied Optics*, 15(11):2611–2613, 1976.

[33] Morel A. and Prieur L. Analysis of variation in ocean color. *Limnology and Oceanography*, 22(4):709–722, 1977.

[34] Kiefer D. *Light absorption, fluorescence, and photosynthesis: Skeletonema costatum and field measurements*, chapter 9 in Ocean Optics, page 283. Number 25 in Oxford Monographs on Geology and Geophysics. Oxford University Press, 1994.

[35] Smith R. and Marshall B. *Raman scattering and optical properties of pure water*, chapter 12 in Ocean Optics, page 283. Number 25 in Oxford Monographs on Geology and Geophysics. Oxford University Press, 1994.

[36] Zhang X., Lewis M., and Johnson B. Influence of bubbles on scattering of light in the ocean. *Applied Optics*, 37(27):6525–6536, 1998.

[37] Baker R. and Smith R. Irradiance transmittance through the air/water interface. In R.w. Spinrad, editor, *Ocean Optics*, volume 1 of *X*, pages 556–565. SPIE, 1990.

[38] Zaneveld J. *Optical closure: from theory to measurement*, chapter 3 in Ocean Optics, page 283. Number 25 in Oxford Monographs on Geology and Geophysics. Oxford University Press, 1994.

[39] Carder K. and Castello D. *Optical effects of large particles*, chapter 13 in Ocean Optics, page 283. Number 25 in Oxford Monographs on Geology and Geophysics. Oxford University Press, 1994.

[40] Morel A. *Optics from the single cell to the mesoscale*, chapter 5 in Ocean Optics, page 283. Number 25 in Oxford Monographs on Geology and Geophysics. Oxford University Press, 1994.

[41] Kattawar G. *Polarization of light in the ocean*, chapter 11 in Ocean Optics, page 283. Number 25 in Oxford Monographs on Geology and Geophysics. Oxford University Press, 1994.

[42] Gordon H. Atmospheric correction of ocean color imagery in the earth observing system era. *Journal of Geophysical Research*, 102(D14):17081–17106, 1997.

[43] Jacobson M. *Fundamentals of atmospheric modelling*. Cambridge University Press, 1999.

[44] Gao B., Montes M., Ahmed Z., and Davis C. Atmospheric correction algorithm for hyperspectral remote sensing of ocean color from space. *Applied Optics*, 39(6):887–896, 2000.

[45] Vermote E., Tanre D., Deuze J., Herman M., and Morcrette J. Second simulation of the satellite signal in the solar spectrum, 6s: An overview. *IEEE Transactions on Geoscience and Remote Sensing*, 35(3):675–686, 1997.

[46] Goody R. *Atmospheric radiation 1, theoretical basis*. Oxford University Press, 1964.

[47] Malkmus W. Random Lorentz band model with exponential-tailed s^{-1} line intensity distribution function. *Journal of Optical Society of America*, 57(3):323–329, 1967.

[48] Gordon H., Clark D., Brown J., Brown O., Evans R., and Broenkow W. Phytoplankton pigment concentrations in the middle atlantic bight-comparison of ship determinations and CZCS estimates. *Applied Optics*, 22(1):20–36, 1983.

[49] Gordon H. and Castano D. Coastal color scanner atmospheric correction algorithm: multiple scattering effects. *Applied Optics*, 26(11):2111–2122, 1987.

[50] Yang H. and Gordon H. Remote sensing of ocean color: assessment of water-leaving radiance bidirectional effects on atmospheric diffuse transmittance. *Applied Optics*, 36(30):7887–7897, 1997.

[51] Wang M. Atmospheric correction of ocean color sensors: computing atmospheric diffuse transmittance. *Applied Optics*, 38(20):451–455, 1999.

[52] Koepke E. Effective reflectance of oceanic whitecaps. *Applied Optics*, 23(11):1816–1824, 1984.

[53] Burt W. Albedo over wind-roughened water. *Journal of Meteology*, 11:283–289, 1954.

[54] Cox C. and Munk W. Measurements of the roughness of the sea surface from photographs of the sun glitter. *Journal of Optical Society of America*, 44:838–850, 1954.

[55] Cox C. and Munk W. Statistics of the sea surface derived from sun glitter. *Journal of Marine Research*, 13:198–227, 1954.

[56] Deschamp P.Y., Herman M., and Tanre D. Modelling of the atmospheric effects and its application to remote sensing of ocean color. *Applied Optics*, (22):3751, 1983.

[57] Hansen J. and Travis L. Light-scattering in planetary atmospheres. *Space Science Reviews*, 16(4):527–610, 1974.

[58] Sturm B. *The atmospheric correction of remotely sensed data and the quantitative determination of suspended matter in marine surface layer*, chapter 11 in Oceanography and Hydrology, pages 163–197. Ellis Horwood, 1980.

[59] Gordon H., Brown J., and Evans R. Exact Rayleigh scattering calculation for the use with the nimbus-7 coastal zone color scanner. *Applied Optics*, 27(5):862–871, 1988.

[60] Gordon H. and Wang M. Surface-roughness consideration for atmospheric correction of ocean color sensors I: The Rayleigh-scattering component. *Applied Optics*, 31(21):4247–4267, 1992.

[61] Gordon H. and Wang M. Retrieval of water-leaving radiance and aerosol optical thickness over the ocean with SeaWiFS: a preliminary algorithm. *Applied Optics*, 33(3):443–452, 1994.

[62] Zhao F. and Nakajima T. Simultaneous determination of water-leaving reflectance and aerosol optical thickness from coastal zone color scanner measurements. *Applied Optics*, 36(27):6949–6956, 1997.

[63] Gordon H., Du T., and Zhang T. Remote sensing of ocean color and aerosol properties: resolving the issue of aerosol absorption. *Applied Optics*, 36(33):8670–8684, 1997.

[64] Chomko R. and Gordon H. Atmospheric correction of ocean color imagery: use of the Junge power-law aerosol size distribution with variable refractive index to handle aerosol absorption. *Applied Optics*, 37(24):5560–5572, 1998.

[65] Gordon H. Removal of atmospheric effects from satellite imagery of oceans. *Applied Optics*, 10:1631–1636, 1978.

[66] Crader K.L., Chen F.R., Lee Z.P., Hawes S. K., and Kamykowski D. Semianalytical moderate-resolution imaging spectrometer algorithms for chlorophyll a and absorption with bio-optical domains based on nitrate-depletion temperature. *Journal of Geophysical Research*, 104(C3):5403–5421, 1999.

[67] Carder K., Cattrall C., and Chen F.R. Modis clear water epsilon. Algorithm Theoretical Basis Document ATBD 21, 1999.

[68] Ruddick K., Ovidio F., and Rijkeboer M. Atmospheric correction of SeaWiFS imagery for turbid coastal and inland waters. *Applied Optics*, 39(6):897–912, 2000.

[69] Hu C., Carder K., and Muller F. Atmospheric correction of SeaWiFS imagery over turbid coastal waters: a practical method. *Remote Sensing of Environment*, (74):195–206, 2000.

[70] Kirk J. Volume scattering function, average cosine, and the underwater light field. *Limnology and Oceanography.*, 36:455–467, 1991.

[71] Gould R., Arnone R., and Martinolic P. Spectral dependence of scattering coefficients in case I and case II waters. *Applied Optics*, 38:2377–2383, 1999.

[72] Li Y. Atmospheric correction of SeaWiFS imagery for turbid coastal and inland waters: comment. *Applied Optics*, 42(6):893–895, 2003.

[73] Gordon H. and Clark D. Clear water radiances for atmospheric correction of coastal color scanner imager. *Applied Optics*, (20):4175–4180, 1981.

[74] Andre J. and Morel A. Atmospheric corrections and interpretation of marine radiance in CZCS imager, revisited. *Oceanlogica Acta*, 14:3–22, 1991.

[75] Salama S., Monbaliu J., and Coppin P. The atmospheric correction of AVHRR images. *International Journal of Remote Sensing*, 2003. accepted for publication.

[76] Bricaud A. and Morel A. Atmospheric correction and interpretation of marine radiances in CZCS imager: use of reflectance model. *Oceanolgica Acta*, 7:33–50, 1987.

[77] Vos R. and Gerritsen H. Use of NOAA/AVHRR satellite remote sensing data for modelling of suspend sediments transport in the North Sea. Technical Report Appendix B to the promise project report, Delft hydraulics, 1997.

[78] Vos R., Villars M., Roozekrans J., Peters S., and Van Raaphorst W. Integrated monitoring of total suspended sediment in the Dutch coastal zone. Technical Report BCRS 5.2/TE-53, 1998. Part II.

[79] Althuis I. and Shimwell S. Modelling of remote sensing reflectance spectra for suspended matter concentration detection in coastal waters. In *EARSeL Advances in Remote Sensing*, volume 4, pages 53–59, 1995.

[80] Emery W. and Thomson R. *Data analysis methods in physical oceanography.* Elsevier, second and revised edition, 2001.

[81] Richards J. *Remote sensing digital image analysis: An introduction.* Springer-Verlag, berlin edition, 1994.

[82] Aage C., Allan T., Carter D., Lindgren G., and Olagnon M. *Oceans from space.* Ifremer, Brest, 1998.

[83] Sospedra E., Caselles V., Coll C., Valor E., and Rubio E. Validation of cloud detection algorithms. In J. L. Casanova, editor, *Remote Sensing in the 21st Century: Economic and Environmental Applications*, Proc. of the 19th (EARSel) Symposium on Remote Sensing in the 21st Century, pages 119–123. EARSel, A.A. Balkema, 2000.

[84] Tolk B., Han L., and Rundquist D. The impact of bottom brightness on spectral reflectance of suspended sediments. *International Journal of Remote Sensing*, 21(11):2259–2268, 2000.

[85] Han L. and Rundquist D. Spectral characterization of suspended sediments generated from two texture classes of clay soil. *International Journal of Remote Sensing*, 17(3):643–649, 1996.

[86] Ding K. and Gordon H. Analysis of the influence of O_2 a-band absorption on atmospheric correction of ocean-color imagery. *Applied Optics*, 35(12):2068–2080, 1995.

[87] Smith R. and Wilson W. Ship and satellite bio-optical research in the california bight. In Gower J.R.F., editor, *Oceanography from Space*, page 256. New York, 1981.

[88] Muller J. Effects of water reflectance at 670nm on coastal zone color scanner (CZCS) aerosol radiance estimates off the coast of central California. In *Ocean Optics*, volume VII of *SPIE*, pages 179–186, 1984.

[89] Viollier M. and Sturm B. CZCS data analysis in turbid coastal water. *Journal of Geophysical Research*, 89(D4):4977–4985, 1984.

[90] Austin R. and Petzold T. The determination of the diffuse attenuation coefficient of seawater using the coastal zone color scanner. In Gower J.R.F., editor, *Oceanography from Space*, pages 281–294. Plenum, New York, 1981.

[91] Gould R. and Arnone R. Extending coastal zone color scanner estimates of the diffuse attenuation coefficient into case II waters. In *SPIE*, volume 2258 of *Ocean Optics XII*, pages 342–357, 1994.

[92] Lavender S., Moore G., and Aiken J. Remote sensing and atmospheric correction of UK coastal waters using MOS imagery. In *SPIE proceeding*, pages 527–532, 1997.

[93] Moore G., Aiken J., and Lavender S. The atmospheric correction of watercolour and the quantitative retrieval of suspended particulate matter in case II waters: application to MERIS. *International Journal of Remote Sensing*, 20(9):1713–1733, 1999.

[94] Antoine D. and Morel A. Relative importance of multiple scattering by air molecules and aerosol in forming the atmospheric path radiance in the visible and near-infrared parts of the spectrum. *Applied Optics*, 37(12):2245–2259, 1998.

[95] Salama S. and Monbaliu J. Atmospheric correction algorithm for CHRIS images: Application to CASI. In Shen S., editor, *Imaging Spectrometry*, volume VIII of *SPIE*, pages 120–131, 2002.

[96] Chomko R., Gordon H., Maritorena S., and Siegel D. Simultaneous retrieval of oceanic and atmospheric parameters for ocean color imagery by optimization: a validation. *Remote Sensing of Environment*, 84:208–220, 2003.

[97] Stamnes K., Li W., Yan B., Eide H., Barnard A., Pegau W., and Stamnes J. Accurate and self-consistent ocean color algorithm: simultaneous retrieval of aerosol optical properties and chlorophyll concentrations. *Applied Optics*, 42(6):939–951, 2003.

[98] Land P. and Haigh J. Atmospheric correction over case 2 waters with an iterative fitting algorithm. *Applied Optics*, 35(27):5443–5451, 1996.

[99] Salama S. and Monbaliu J. CASI in-situ campaign. Technical report, Hydraulics Laboratory KULeuven, 2003.

[100] Salama S. and Monbaliu J. DAIS/ROSIS in-situ campaign. Technical report, Hydraulics Laboratory KULeuven, 2003.

[101] Press W., Flannery B., Teukolsky S., and Vetterling W. *Numerical recipes in C++, The art of scientific computing.* Cambridge University Press, second edition, 2002.

[102] Nanu L. and Robertson C. Estimating suspended sediment concentrations from spectral reflectance data. *International Journal of Remote Sensing*, 11(5):913–920, 1990.

[103] Holyer R. Towards universal multispectral suspended sediment algorithm. *Remote Sensing of Environment*, 7:323–338, 1978.

[104] Stumpf R. Sediment transport in Chesapeake bay during floods: analysis using satellite and surface observations. *Journal of Coastal Research*, 4(1):1–15, 1988.

[105] Lathrop R. and Lillesand T. Monitoring water quality and river plume transport in green bay, lake Michigan with SPOT-1 imagery. *Photogrammetric Engineering And Remote Sensing*, 55(3):349–354, 1989.

[106] Novo E., Hansom J., and Curran P. The effect of viewing geometry and wavelength on the relationship between reflectance and suspended sediment concentration. *International Journal of Remote Sensing*, 10(8):1357–1372, 1989.

[107] Lathrop R., Lillesand T., and Yandell B. Testing the utility of simple multi date thematic mapper calibration algorithms for monitoring turbid inland waters. *International Journal of Remote Sensing*, 12(10):2045–2063, 1991.

[108] Ferrier G. A field study of the variability in the suspended sediment concentration-reflectance relationship. *International Journal of Remote Sensing*, 16(14):2713–2720, 1995.

[109] Han L. Spectral reflectance with varying suspended sediment concentration in clear and algae-laden waters. *Photogrammetric Engineering and Remote Sensing*, 63(6):701–705, 1997.

[110] Gao J. and OLeary S. Estimation of suspended solids from aerial photographs in a GIS. *International Journal of Remote Sensing*, 18(10):2073–2086, 1997.

[111] Pozdnyakov D., Kondratyev K., Bukata R., and Jerome J. Numerical modelling of natural water colour: implications for remote sensing and limnological studies. *International Journal of Remote Sensing*, 19(10):1913–1932, 1998.

[112] Ouillon S. Forget P. Surface suspended matter off the Rhone river mouth from visible satellite imagery. *Oceanologica Acta*, 21(6):739–749, 1998.

[113] Kallio K., Kutser T., Hannonen T., Koponen S., Pulliainen J., Vepsalainen J., and Pyhalahti T. Retrieval of water quality from airborne imaging spectrometry of various lake types in different seasons. *Science of the Total Environment*, 208(1-3):59–77, 2001.

[114] Doxaran D., Froidefond J., Lavender S., and Castainga S. Spectral signature of highly turbid waters application with SPOT data to quantify suspended particulate matter concentrations. *Remote Sensing of Environment*, 81(1):149–161, 2002.

[115] Durand D. and Cauneau F. Towards a new method for shallow water monitoring using remote sensing. In Gumandsen P., editor, *Future Trends in Remote Sensing*, 1998.

[116] Mikkelsen O. Variation in the projected surface area of suspended particles: Implication for remote sensing assessment of TSM. *Remote Sensing of Environment*, 79:23–29, 2002.

[117] Forget P., Broche P., and Naudin J. Reflectance sensitivity to solid suspended sediment stratification in coastal water and inversion: a case study. *Remote Sensing of Environment*, 77:92–103, 2001.

[118] Doerffer R. and Fischer J. Concentration of chlorophyll, suspended matter, and gelbstoff in case II waters derived from satellite coastal zone color scanner with inverse methods. *Journal Of Geophysical Research*, 99(C4):7457–7466, 1994.

[119] Forget P., Ouillon S., Lahet F., and Broche P. Inversion of reflectance spectra of nonchlorophyllous turbid coastal waters. *Remote Sensing of Environment*, 68(3):264–272, 1999.

[120] Twardowski M., Boss E., Macdonald J., Pegau W., Barnard A., and Zaneveld J. A model for estimating bulk refractive index from the optical backscattering ratio and the implications for understanding particle composition in case I and case II waters. *Journal Of Geophysical Research-Oceans*, 106(C7):14129–14142, 2001.

[121] Gordon H. and Du T. Light scattering by nonspherical particles: Application to coccoliths detached from emiliania huxleyi. *Limnology And Oceanography*, 46(6):1438–1454, 2001.

[122] Risovic D. Effect of suspended particulate-size distribution on the backscattering ratio in the remote sensing of seawater. *Applied Optics*, 41(33):7092–7101, 2002.

[123] Bard Y. *Nonlinear parameter estimation.* Academic Press, 1974.

[124] Tassan S. The effect of dissolved "yellow substance" on the quantitative retrieval of chlorophyll and total suspended sediment concentrations from remote measurements of water colour. *International Journal of Remote Sensing*, 9(4):787–797, 1988.

[125] Holben B., Eckdagger T., Slutsker I., Tanr D., Buis J., Setzer A., Vermote E., Reagan J., Kaufman Y., Nakajima T., Lavenu F., Jankowiak I., and Smirnov A. AERONETA Federated instrument network and data archive for aerosol characterization. *Remote Sensing of Environment*, 66(1):1–16, 1998.

[126] Bates D. and Watts D. *Nonlinear Regression Analysis and Its Applications.* John Wiley and Sons, NY, 1988.

[127] Tassan S. and Ferrari G. An alternative approach to absorption measurements of aquatic particles retained on filters. *Limnology and Oceanography*, 40(8):1358–1368, 1995.

[128] Balch W., Drapeau D., Cucci T., Vaillancourt R., Kilpatrick K., and Fritz J. Optical backscattering by calcifying algae: Separating the contribution of particulate inorganic and organic carbon fractions. *Journal Of Geophysical Research-Oceans*, 104(C1):1541–1558, 1999.

[129] Gordon H. Sensitivity of radiative transfer to small angle scattering in the ocean: quantitative assessment. *Applied Optics*, 32(36):7505–7511, 1993.

[130] Neckel H. and Labs D. Improved data of solar spectral irradiance from 0.33 to 1.25 μm. *Solar Physics*, 74:231–249, 1981.

[131] Gregg W. and Carder K. A simple spectral solar irradiance model for cloudless maritime atmospheres. *Limnology and Oceanography*, 35(8):1657–1675, 1990.

[132] Murray W. *Numerical methods for unconstrained optimization.* Academic Press, 1972.

[133] Gill Ph.E., Murray W., and Wright M.H. *Practical optimization.* Academic Press. 1981.

Appendix A

The solar energy

A.1 The solar spectrum

The extraterrestrial solar irradiance corrected for the earth-sun distance can be estimated as (Gordon et al.1983[48]):

$$E_o(\lambda) = H_o(\lambda)\left(1 + e\cos\left(\frac{2\pi(D-3)}{365}\right)\right]^2 \qquad \text{(A-1)}$$

Where $H_o(\lambda)$ is the mean extraterrestrial irradiance obtained from Neckel and Labs (1981)[130], e=0.0167 is the orbital eccentricity and D is the Julian day (figure A.1). This solar radiation travels, within the earth atmosphere, along a path that is proportional to the solar zenith angle i.e. $1/\cos(\theta)$. The path-length of the light (from sun to target) can be calculated taking into account the sphericity of the earth-atmospheric system as (Gregg and Carder 1990[131]):

$$M(\theta) = 1\Big/\left(\cos\theta + 0.15\,(93.885-\theta)^{-1.253}\right) \qquad \text{(A-2)}$$

Note that the longer this path is, the greater the chance that a photon will hit a scattering or absorbing center (i.e. molecules or particles). Thus some energy will be lost (absorbed or scattered out) or gained due to the scattering into the beam of incident light. Similar processes occur in the second path of the light from target to the sensor. The solar zenith and azimuth for a location (latitude and longitude) on the earth surface can be calculated knowing the day of the year and time of the day. Figure

(A.1) depicts the solar irradiance and at top of atmosphere (TOA). As we can see that the maximum solar energy is at 0.555 μm wavelength. It is not a coincidence that this wavelength (0.555 μm) induces the maximum sensation of brightness in the human eye (retina).

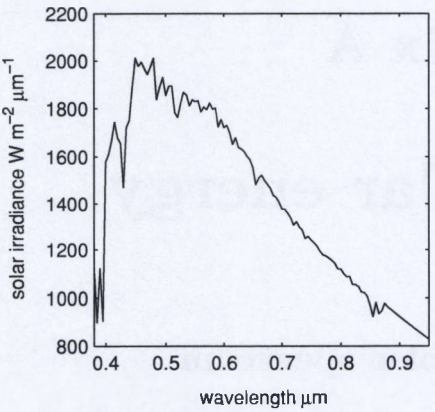

Fig. A.1: The solar irradiance at the TOA corrected for earth sun distance.This was for 23 August 2000 and sun zenith of 40°.

A.2 The nature of solar radiative-energy

The solar radiant-energy is envisioned as consisting of numerous localized packets of time-varying self sustaining electric and magnetic field called photons. The photon is a quantum of electromagnetic energy that has no mass, no electric charge and a speed in the vacuum of $c = 2.99792458 \times 10^8 [ms^{-1}]$. Note that the dual aspects of light as an electromagnetic wave or quanta are both important for proper treatment of light interaction with matter. The energy q [J] of a photon is related to its frequency ν [s] and corresponding wavelength λ [μm] by :

$$q = h\nu = \frac{hc}{\lambda} \tag{A-3}$$

Where $h = 6.6260755 \times 10^{-34}$[J s] is plank's constant. Equation(A-3) shows that the radiant energy is greater at shorter wavelengths. This radiation is emitted by all bodies in the universe that have temperature above absolute zero (0 K). A blackbody is a substance, in thermodynamic equilibrium, that emits all radiation that it absorbs. The radiance L_B that is emitted by a

blackbody with temperature T [K] at wavelength λ μm (spectral radiance) can be expressed by Planck's law:

$$L_B = \frac{2hc^2}{\lambda^5[\exp(\frac{hc}{\lambda K_B T})] - 1} \tag{A-4}$$

Where k_B is the Boltzmann's constant $1.3806568 \times 10^{-23}$[J.K^{-1}]. In reality all natural bodies emit a fraction of a perfect blackbody radiance. This fraction is the emissivity of that substance $\epsilon_\lambda \leq 1$, and therefore the radiance emitted by any substance can be approximated as:

$$L_\lambda = \epsilon_\lambda L_B \tag{A-5}$$

Equations (A-4 and A-5) are the means to estimate the sea-surface temperature from radiance measurements.

Appendix B

Geometry

B.1 The coordinates system

A unit sphere is a sphere with radius normalized to unity. The unit sphere Ξ specify a set of directions $\xi \in \Xi$. Therefor Ξ represents all zenith θ and azimuthal ϕ angles such that: $0 \leq \theta \leq \pi$ and $0 \leq \phi \leq 2\pi$. Considering the two-way path of the solar radiant energy from sun to target to sensor, the set Ξ can be divided into two subsets. These are the upward and the downward hemisphere of directions, Ξ_u and Ξ_d (see figure B.1):

$$\Xi_u : \pi/2 \leq \theta \leq \pi \qquad 0 \leq \phi \leq 2\pi \tag{B-1}$$

$$\Xi_d : 0 \leq \theta \leq \pi/2 \qquad 0 \leq \phi \leq 2\pi \tag{B-2}$$

The solid angle is an extension of two dimensional space angle and has a unit of steradian $[sr]$. An incremental solid angle $d\Omega$ is an incremental surface area dA on a unit sphere according to (B-3).

$$d\Omega = \frac{dA}{r^2} \tag{B-3}$$

The incremental surface can be derived as:

$$dA = (rd\theta)\,(r\sin\theta d\phi) = r^2 \sin\theta d\theta d\phi \tag{B-4}$$

where $d\theta$ and $d\phi$ are the increment zenith and azimuth angles respectively. Substituting (B-4) in (B-3) gives the incremental solid angle:

$$d\Omega = \sin\theta d\theta d\phi \tag{B-5}$$

Any point $\overrightarrow{X} = (x, y, z)$ on the unit sphere can be linked to the viewing geometry (zenith θ and azimuth ϕ) as :

$$\begin{aligned} x &= \sin\theta\cos\phi \\ y &= \sin\theta\sin\phi \\ z &= \cos\theta \end{aligned}$$

The direction vector ξ is:

$$\xi = \sin\theta\cos\phi i_1 + \sin\theta\sin\phi i_2 + \cos\theta i_3 \tag{B-6}$$

Where i, j, and k are the three perpendicular unit vector that define a right handed cartesian coordinate system. The used coordinate system is illustrated in figure(B.1).

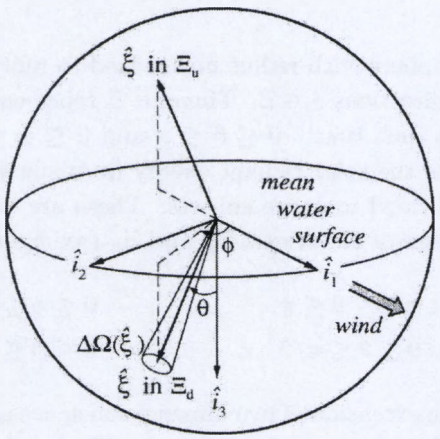

Fig. B.1: The used coordinate system for defining upward and downward directions.

Appendix C

Least-square minimization

C.1 The cost function

An approach to retrieve the IOP from recoded reflectance is to maximize the likelihood of the IOP that give the observed water leaving reflectance. Suppose that the water leaving reflectance is modelled as a set of data; a point for each band. The measurement error of the water leaving reflectance at each band can be assumed normally distributed around the model output (the mean). The probability distribution function of the data-set is proportional to the product of each probability at each band:

$$P \propto \prod_{i=1}^{N} \left\{ \exp\left(-\frac{1}{2} \left[\frac{\rho_{w,r}^{(\lambda_i)} - \rho_{w,m}^{(\lambda_i)}(\mathbf{iop})}{\sigma_i} \right]^2 \right) \Delta\rho_w \right\} \qquad \text{(C-1)}$$

Where $\rho_{w,r}^{(\lambda_i)}$ is the recorded water leaving reflectance and $\rho_{w,m}^{(\lambda_i)}(\mathbf{iop})$ is the modelled reflectance as a function of the IOP's vector **iop**; σ_i is the standard deviation of the measurements at the band i. Maximizing (C-1) is equivalent to maximizing its logarithm, or minimizing the negative of its logarithm:

$$\frac{1}{2} \sum_{i=1}^{N} \left[\frac{\rho_{w,r}^{(\lambda_i)} - \rho_{w,m}^{(\lambda_i)}(\mathbf{iop})}{\sigma_i} \right]^2 - N \log \Delta\rho_w \qquad \text{(C-2)}$$

The number of bands N and the derivative $\Delta\rho_w$ can be assumed constant, minimizing (C-2) is equivalent to minimizing the following:

$$\chi^2 = \sum_{i=1}^{N} \left[\frac{\rho_{w,r}^{(\lambda_i)} - \rho_{w,m}^{(\lambda_i)}(\mathbf{iop})}{\sigma_i} \right]^2 \tag{C-3}$$

The quantity in (C-3) is called the chi-square (χ^2). This corresponds to the sum of N squares of normally distributed quantities, each normalized to a unit variance. If the variance can be assumed constant for all channels then the minimization in (C-3) is simplified to:

$$\phi = \sum_{i=1}^{N} \left[\rho_{w,r}^{(\lambda_i)} - \rho_{w,m}^{(\lambda_i)}(\mathbf{iop}) \right]^2 \tag{C-4}$$

From the above discussion we can conclude that least-square minimization is a special case of chi-square minimization (maximum likelihood estimation) of the fitted parameters. This is true taking into account our first assumption of normally distributed errors with a constant standard deviation.

C.2 Gauss Newton method

Equation (C-4) can be started with initial values of the IOP. In each iteration (j) the values of the IOP are adjusted to decrease the cost function ($\phi_{j+1} < \phi_j$). This is proceeded until the cost function has converged to the minimum. Brief outlines of the Gauss Newton method are given in the following paragraph. The function (ϕ) can be approximated by its Taylor series (up to the second order):

$$\phi_{j+1} = \phi_j + \mathbf{g}_j^T(\mathbf{iop}_{j+1} - \mathbf{iop}_j) + \frac{1}{2}(\mathbf{iop}_{j+1} - \mathbf{iop}_j)^T \mathbf{H}_j (\mathbf{iop}_{j+1} - \mathbf{iop}_j) \tag{C-5}$$

Where $\mathbf{g}_j$ and $\mathbf{H}_j$ are, respectively, the gradient vector and the hessian matrix at iteration j. If the the function (ϕ) is minimum at $\mathbf{iop}_{j+1}$ then:

$$\frac{\Delta\phi_{j+1}}{\Delta\mathbf{iop}_{j+1}} = \mathbf{g}_j + \mathbf{H}_j(\mathbf{iop}_{j+1} - \mathbf{iop}_j) = 0 \tag{C-6}$$

If $\mathbf{H}_j$ is nonsingular then:

$$\mathbf{iop}_{j+1} = \mathbf{iop}_j - \mathbf{H}_j^{-1}\mathbf{g}_j \tag{C-7}$$

The function ϕ_j can be written as:

$$\phi_j = \sum_{i=1}^{N} e_i^2 \tag{C-8}$$

Where the right hand side of equation (C-8) is the sum of residuals between modelled and measured reflectances at iteration j. The gradient vector can be calculated such as:

$$\mathbf{g}_j = \frac{\Delta\phi_j}{\Delta\mathbf{iop}_j} = 2\sum_{i=1}^{N} e_i \frac{\Delta e_i}{\Delta\mathbf{iop}_j} \tag{C-9}$$

Where the second term on the right hand side of equation (C-9) is the jacobian matrix. The hessian matrix can then be approximated from the jacobian matrix $\mathbf{J}_{(i,j)}$ as:

$$\mathbf{H}_j = 2\sum_{i=1}^{N} \mathbf{J}_{(i,j)}^T \mathbf{J}_{(i,j)} \tag{C-10}$$

Defining the searching direction of the algorithm will take us out of the scope of this study. For detailed discussion about the searching direction see Murray 1972[132], Bard 1974[123] and Gill et al., 1981[133] and Press et al., 2002[101].

Resumé

Suhyb Salama graduated in the year 1993 from the faculty of civil engineering of Damascus University. The subject of his thesis was "*Project management and constructions*". He joined military service as a supervisor engineer till 1995. Then he continued in the same position till 1997 in the Syrian Ministry of Higher Education. In the year 1997 he joined a private company as a system analyst. His work in Syria, during the last three years, provided him with the necessary budget to fund his Master study and the first year of his PhD. In the year 1999 he enrolled in a pre-doctorate master programm at the hydraulics laboratory KUL. The subject of his thesis was "*Monitoring suspended sediment in coastal water by optical earth observation technique*". Since the year 2000 he involved in the research activities as a research assistant in the hydraulics lab at KUL. His research focused on optical oceanography and lead to this PhD dissertation.

List of publications

Peer-reviewed journal

1. Salama S. Monbaliu J. and Coppin P.,2003 The atmospheric correction of AVHRR images. *Int. J. Remote Sensing*, Vol.24. No. pp.

International conference proceedings

1. Salama S. and Monbaliu J., 2002. Atmospheric correction algorithm for CHRIS images: Application to CASI. Imaging Spectrometry VIII, *Proc. of SPIE*, Vol. 4816, pp 120-131.

2. Salama S. and Monbaliu J., Quantification of suspended particulate matters from DAIS/ROSIS images: case-II waters". *Third EARSeL workshop on Imaging Spectroscopy*, 2003, Oberpfaffenhofen, Germany (accepted).

3. Salama S. and Monbaliu J., The estimation of marine bio-geo-physical quantities from CHRIS images. *23rd EARSeL symposium on Very High Resolution Data*, 2003, Gent, Belgium (accepted).

Internal reports

1. Salama S. and Monbaliu J., CASI in-situ campaign (in voorbereiding).

2. Salama S. and Monbaliu J., DAIS/ROSIS in-situ campaigns (in voorbereiding).

Published abstracts in inter-/national conferences and workshops

1. Salama S., 2003. The estimation of marine bio-geo-physical quantities from hyperspectral images. Poster presentatie, *VLIZ young scientists' day*, Brugge, Belgium.

2. Salama S. and Monbaliu J.,2003. Hyperspectral Remote Sensing of Suspended Sediment in Coastal Waters" with subtitle : CHRIS/PROBA, data exploitation: simulations, *CHRIS data exploitation* ESTC, Noordwijk, The Netherlands.

3. Salama S. and Monbaliu J., The estimation of marine bio-geo-physical quantities from hyperspectral images. *23rd EARSeL symposium on Very High Resolution Data*, 2003, Gent, Belgium.

4. Salama S. and Monbaliu J., Quantification of suspended particulate matters from DAIS/ROSIS images: case-II waters". *Third EARSeL workshop on Imaging Spectroscopy*, 2003, Oberpfaffenhofen, Germany.

5. Salama S. and Monbaliu J., 2002, Hyperspectral remote sensing of suspended sediments in coastal waters, *results-reporting meeting*, DLR, Oberpfaffenhofen, Germany.

6. Salama S. and Monbaliu J., 2002. Atmospheric correction algorithm for CHRIS images: Application to CASI. *Imaging Spectrometry VIII*, SPIE, Seattle, USA.

7. Salama S., 2002. Atmospheric correction of CHRIS data: A first step towards suspended sediment quantification. *VLIZ young scientists' day,* Brugge, Belgium.

8. Salama S. and Monbaliu J., 2001, Hyperspectral remote sensing of suspended sediments in coastal waters, *planning-meeting*, DLR, Oberpfaffenhofen, Germany.

9. Salama S. and Monbaliu J., 2000, Hyperspectral imaging of water quality, *planning-meeting*, ESTC, Noordwijk, The Netherlands.

10. Salama S., Ruddick K., Monbaliu J. and Coppin P., 2000. Aerosol scattering removal. *Ocean from Space symposium*, Venice, Italy.

In preparation

1. Salama S. and Monbaliu J., Coupled approach for simultaneous atmospheric-correction and SPM quantification: Case II waters. Journal of Geophysical Research.

2. Salama S. and Monbaliu J., Principle component transformation to classify clear water pixels and atmospherically correct SeaWiFS images. Remote sensing of Environment.

3. Salama S. and Monbaliu J., Semi-analytical approach to estimate the concentrations of small and large particles of SPM: Investigation. IEEE Transaction on Geosciences and Remote Sensing.

4. Salama S. and Monbaliu J., Stochastic technique to estimate the uncertainty bounds on the IOP. Journal of Geophysical Research.